Forschungsbericht 2022-30

Aerodynamics of Forward and Backward Swept Wings with an Over-Wing-Nacelle

Fabian Lange-Schmuckall

Deutsches Zentrum für Luft- und Raumfahrt
Institut für Aerodynamik und Strömungstechnik
Braunschweig

Deutsches Zentrum
für Luft- und Raumfahrt

Forschungsbericht 2022-30

Aerodynamics of Forward and Backward Swept Wings with an Over-Wing-Nacelle

Fabian Lange-Schmuckall

Deutsches Zentrum für Luft- und Raumfahrt
Institut für Aerodynamik und Strömungstechnik
Braunschweig

111 Seiten
108 Bilder
3 Tabellen
66 Literaturstellen

Deutsches Zentrum für Luft- und Raumfahrt
DLR

Herausgeber:

Deutsches Zentrum
für Luft- und Raumfahrt e. V.
Wissenschaftliche Information
Linder Höhe
D-51147 Köln

ISSN 1434-8454
ISRN DLR-FB-2022-30
Erscheinungsjahr 2022

DOI: https://doi.org/10.57676/qde0-ak32

Triebwerksintegration, Überflügelanordnung, Installationseffekte, UHBR, Reiseflug, SFB880

Fabian Lange-Schmuckall
DLR, Institut für Aerodynamik und Strömungstechnik, Braunschweig

Aerodynamik von Vorwärts und Rückwärts gepfeilten Flügeln mit einem Triebwerk in Überflügelanordnung

Dissertation, Technische Universität Braunschweig

In dieser Dissertation wird der Einfluss von Strahltriebwerken mit sehr großem Bypassverhältnis in Überflügelanordnung auf die aerodynamischen Charakteristika des Flügels anhand von zwei Flugzeugkonfigurationen untersucht. Das Triebwerk ist dabei oberhalb der Flügelhinterkante positioniert. In Reiseflugbedingungen, bei einer Machzahl von 0.78, werden verschiedene Aspekte untersucht, um ein grundsätzliches und allgemeingültiges Verständnis für die damit einhergehenden Installationseffekte aufzubauen.

Zu Beginn ermöglicht ein Vergleich zwischen Flügel-Rumpf und Flügel-Rumpf-Pylon-Triebwerk Konfiguration mit rückwärts gepfeiltem Flügel die Identifikation der Installationseffekte. Eine Variation des Triebwerksschubs bietet die Möglichkeit einer weiterführenden Detaillierung der aerodynamischen Interaktion zwischen Flügel und Triebwerk in Überflügelanordnung.

Die Untersuchungen zeigen einen deutlichen Einfluss auf die Druckverteilung der Flügeloberseite durch die Installation der Gondel oberhalb der Flügelhinterkante, wohingegen die Flügelunterseite nahezu unbeeinflusst ist. Der Druck entlang der Flügeloberseite ist dabei abhängig einerseits von der Präsenz der Triebwerksgondel und andererseits von dem Schubzustand des Triebwerks, wobei der räumliche Einflussbereich in stromauf und spannweitiger Richtung in der Größenordnung des Gondeldurchmessers liegt. Dies führt unter anderem zu einer stromauf Verschiebung der Stoßlage auf dem Flügel. Darüber hinaus sind weitere Strömungsbeeinflussungen ausgehend von der OWN in Querströmungsrichtung zu beobachten, welche zu weiteren Überschallgebieten und stoßinduzierten Ablösungen führen.

Des Weiteren ermöglicht die Variation der vertikalen und horizontalen Triebwerksposition einen weiteren Einblick und Bewertung bezüglich der Auslöser, die beispielsweise zur Änderung der Stoßposition oder Strömungsablösungen führen, und die damit einhergehende Änderung der aerodynamischen Koeffizienten. In diesem Zusammenhang werden die aerodynamischen Koeffizienten mit Hilfe von Oberflächen- und Volumen-basierten Auswerteverfahren untersucht, um damit den räumlichen Ursprung als auch die Art des generierten Widerstands zu identifizieren. Die vertikale Triebwerksposition wirkt sich dabei hauptsächlich auf die Unterschallströmung entlang des hinteren Flügelsegments aus, wodurch primär der Auftriebsbeiwert beeinflusst wird, wohingegen die horizontale Triebwerksposition einen Einfluss auf den Gesamtwiderstand und die Stoßposition aufweist.

Die Untersuchung der OWN an einem sowohl rückwärts als auch vorwärts gepfeilten Tragflächengrundriss bietet die Möglichkeit die Installationseffekte und damit einhergehenden aerodynamischen Eigenschaften an einer weiteren Konfiguration zu analysieren, um damit auf der einen Seite den Einfluss der Vorwärtspfeilung zu untersuchen und auf der anderen Seite eine erweiterte, sowie allgemeingültige Bewertung der OWN-Installation abzuleiten. Die Analyse der OWN an der vorwärts gepfeilten Konfiguration zeigt vergleichbare Installationseffekte, wie sie auch für den rückwärts gepfeilten Flügel zu beobachten sind. Jedoch hat sich durch den negativen Pfeilungswinkel der dominante Störbereich vom äußeren zum inneren Flügelsegment verschoben.

Engine integration, Over-wing-nacelle, Installation effects UHBR, Cruise flight, SFB880

Fabian Lange-Schmuckall
German Aerospace Center (DLR), Institute of Aerodynamics and Flow Technology, Braunschweig

Aerodynamics of Forward and Backward Swept Wings with an Over-Wing-Nacelle

Doctoral Thesis, Technical University Braunschweig

In this thesis the impact of ultra-high bypass ratio over-wing-nacelle installation on aerodynamic wing characteristics is investigated on the basis of two aircraft configurations. The engine was placed above the wing trailing edge. For cruise flight conditions, at a Mach number of 0.78, different aspects are evaluated to build up a fundamental and generalized understanding of the associated installation effects. The investigation is accomplished with the aid of numerical simulations.

At first, a comparison of wing-body and wing-body-engine-pylon configuration for a swept-back wing enables the identification of basic installation effects. The variation of the engine power setting provides a further detailing of the aerodynamic interaction between wing and OWN.

The investigations reveal a significant effect on the upper wing pressure distribution due to the installation of an OWN-UHBR engine, while the lower wing is almost unaffected. The upper wing surface pressure is influenced on the one hand by the presence of the engine and on the other hand the engine power setting, whereby the sphere of influence in upstream and sideways direction is within the order of the engine diameter, leading to an upstream shift of the wing shock position in front of the engine. Moreover, flow disturbances originating from the OWN, are induced along the wing span, especially in the direction of the wing sweep, resulting in additional regions of supersonic flow and shock induced flow separations.

The impact of an engine position variation in vertical and horizontal direction enables insight and assessment of the causes resulting in e.g. shock position variation or flow separations and their associated impact on aerodynamic coefficients. In this regard, the aerodynamic coefficients are evaluated with the aid of surface- and volume-based approaches to identify the type of generated drag component as well as the place of origin. The vertical engine position affects mainly the subsonic rear wing pressure level and thus has solely an impact on the wing lift coefficient, while the horizontal engine position is dominant with respect to the overall drag and affects the wing shock position.

The investigation of OWN installation on a backward and forward swept wing planform offers an examination of the installation effects and accompanied aerodynamic characteristics on an additional configuration to derive on the one hand the impact of forward sweep and on the other hand achieve an extended and more general evaluation. The OWN installation on the forward swept wing configuration reveals similar interactions, as observed for the backward swept wing, whereby the main area of interference switches for the negative sweep angle from outer to inner wing segment.

TU Braunschweig – Niedersächsisches
Forschungszentrum für Luftfahrt

Berichte aus der Luft- und Raumfahrttechnik

Forschungsbericht 2022-25

Aerodynamics of Forward and Backward Swept Wings with an Over-Wing-Nacelle

Fabian Lange-Schmuckall

Deutsches Zentrum für Luft- und Raumfahrt
Institut für Aerodynamik und Strömungstechnik
Braunschweig

Diese Veröffentlichung wird gleichzeitig in der Berichtsreihe "NFL -Forschungsberichte" geführt.

Diese Arbeit erscheint gleichzeitig als von der Fakultät für Maschinenbau der Technischen Universität Carolo-Wilhelmina zu Braunschweig zur Erlangung des akademischen Grades eines Doktor-Ingenieurs genehmigte Dissertation.

Aerodynamics of Forward and Backward Swept Wings with an Over-Wing-Nacelle

Von der Fakultät für Maschinenbau
der Technischen Universität Carolo-Wilhelmina zu Braunschweig

zur Erlangung der Würde

eines Doktor-Ingenieurs (Dr.-Ing.)

genehmigte Dissertation

von:	Fabian Lange-Schmuckall
geboren in:	Flensburg

eingereicht am:	07.06.2022
mündliche Prüfung am:	24.11.2022
Vorsitz:	Prof. Dr.-Ing. S. Heimbs
Gutachter:	Prof. Dr.-Ing. R. Rudnik Prof. Dr.-Ing. R. Radespiel

2022

Aerodynamics of Forward and Backward Swept Wings with an Over-Wing-Nacelle

Abstract

In this thesis the impact of ultra-high bypass ratio over-wing-nacelle installation on aerodynamic wing characteristics is investigated on the basis of two aircraft configurations. The engine was placed above the wing trailing edge. For cruise flight conditions, at a Mach number of 0.78, different aspects are evaluated to build up a fundamental and generalized understanding of the associated installation effects. The investigation is accomplished with the aid of numerical simulations.

At first, a comparison of wing-body and wing-body-engine-pylon configuration for a swept-back wing enables the identification of basic installation effects. The variation of the engine power setting provides a further detailing of the aerodynamic interaction between wing and OWN. The investigations reveal a significant effect on the upper wing pressure distribution due to the installation of an OWN-UHBR engine, while the lower wing is almost unaffected. The upper wing surface pressure is influenced on the one hand by the presence of the engine and on the other hand the engine power setting, whereby the sphere of influence in upstream and sideways direction is within the order of the engine diameter, leading to an upstream shift of the wing shock position in front of the engine. Moreover, flow disturbances originating from the OWN, are induced along the wing span, especially in the direction of the wing sweep, resulting in additional regions of supersonic flow and shock induced flow separations.

The impact of an engine position variation in vertical and horizontal direction enables insight and assessment of the causes resulting in e.g. shock position variation or flow separations and their associated impact on aerodynamic coefficients. In this regard, the aerodynamic coefficients are evaluated with the aid of surface- and volume-based approaches to identify the type of generated drag component as well as the place of origin. The vertical engine position affects mainly the subsonic rear wing pressure level and thus has solely an impact on the wing lift coefficient, while the horizontal engine position is dominant with respect to the overall drag and affects the wing shock position.

The investigation of OWN installation on a backward and forward swept wing planform offers an examination of the installation effects and accompanied aerodynamic characteristics on an additional configuration to derive on the one hand the impact of forward sweep and on the other hand achieve an extended and more general evaluation. The OWN installation on the forward swept wing configuration reveals similar interactions, as observed for the backward swept wing, whereby the main area of interference switches for the negative sweep angle from outer to inner wing segment.

Übersicht

In dieser Dissertation wird der Einfluss von Strahltriebwerken mit sehr großem Bypassverhältnis in Überflügelanordnung auf die aerodynamischen Charakteristika des Flügels anhand von zwei Flugzeugkonfigurationen untersucht. Das Triebwerk ist dabei oberhalb der Flügelhinterkante positioniert. In Reiseflugbedingungen, bei einer Machzahl von 0.78, werden verschiedene Aspekte untersucht, um ein grundsätzliches und allgemeingültiges Verständnis für die damit einhergehenden Installationseffekte aufzubauen.

Zu Beginn ermöglicht ein Vergleich zwischen Flügel-Rumpf und Flügel-Rumpf-Pylon-Triebwerk Konfiguration mit rückwärts gepfeiltem Flügel die Identifikation der Installationseffekte. Eine Variation des Triebwerksschubs bietet die Möglichkeit einer weiterführenden Detaillierung der aerodynamischen Interaktion zwischen Flügel und Triebwerk in Überflügelanordnung. Die Untersuchungen zeigen einen deutlichen Einfluss auf die Druckverteilung der Flügeloberseite durch die Installation der Gondel oberhalb der Flügelhinterkante, wohingegen die Flügelunterseite nahezu unbeeinflusst ist. Der Druck entlang der Flügeloberseite ist dabei abhängig einerseits von der Präsenz der Triebwerksgondel und andererseits von dem Schubzustand des Triebwerks, wobei der räumliche Einflussbereich in stromauf und spannweitiger Richtung in der Größenordnung des Gondeldurchmessers liegt. Dies führt unter anderem zu einer stromauf Verschiebung der Stoßlage auf dem Flügel. Darüber hinaus sind weitere Strömungsbeeinflussungen ausgehend von der OWN in Querströmungsrichtung zu beobachten, welche zu weiteren Überschallgebieten und stoßinduzierten Ablösungen führen.

Des Weiteren ermöglicht die Variation der vertikalen und horizontalen Triebwerksposition einen weiteren Einblick und Bewertung bezüglich der Auslöser, die beispielsweise zur Änderung der Stoßposition oder Strömungsablösungen führen, und die damit einhergehende Änderung der aerodynamischen Koeffizienten. In diesem Zusammenhang werden die aerodynamischen Koeffizienten mit Hilfe von Oberflächen- und Volumenbasierten Auswerteverfahren untersucht, um damit den räumlichen Ursprung als auch die Art des generierten Widerstands zu identifizieren. Die vertikale Triebwerksposition wirkt sich dabei hauptsächlich auf die Unterschallströmung entlang des hinteren Flügelsegments aus, wodurch primär der Auftriebsbeiwert beeinflusst wird, wohingegen die horizontale Triebwerksposition einen Einfluss auf den Gesamtwiderstand und die Stoßposition aufweist.

Die Untersuchung der OWN an einem sowohl rückwärts als auch vorwärts gepfeilten Tragflächengrundriss bietet die Möglichkeit die Installationseffekte und damit einhergehenden aerodynamischen Eigenschaften an einer weiteren Konfiguration zu analysieren, um damit auf der einen Seite den Einfluss der Vorwärtspfeilung zu untersuchen und auf der anderen Seite eine erweiterte, sowie allgemeingültige Bewertung der OWN-Installation abzuleiten. Die Analyse der OWN an der vorwärts gepfeilten Konfiguration zeigt vergleichbare Installationseffekte, wie sie auch für den rückwärts gepfeilten Flügel zu beobachten sind. Jedoch hat sich durch den negativen Pfeilungswinkel der dominante Störbereich vom äußeren zum inneren Flügelsegment verschoben.

Declaration

I hereby declare that I have conducted this work independently. All used auxiliary materials are indicated. No portion of the work referred to in this thesis has been submitted in support of an application for another degree or qualification at this or any other institution of education. For actuality reasons, extracts of the present study have been published in specific scientific papers.

Eidesstatliche Erklärung

Hiermit versichere ich an Eides statt, dass ich die vorliegende Arbeit selbständig angefertigt habe. Alle benutzten Hilfsmittel sind angegeben. Diese Arbeit ist bisher weder veröffentlicht noch an einer anderen Hochschule eingereicht worden. Aus Gründen der Aktualität wurden Auszüge der vorliegenden Arbeit in bestimmten wissenschaftlichen Artikeln vorveröffentlicht.

Bremen, im Juni 2022

Fabian Lange-Schmuckall

Acknowledgment

This work was carried out during my employment as a research engineer at the Institute of Aerodynamics and Flow Technology at the German Aerospace Center.

I would like to thank Prof. Dr.-Ing. R. Rudnik very much for performing all the functions of a doctoral supervisor, for his support and guidance, which contributed to the success of this work, and the opportunity to conduct this PhD thesis in the framework of my daily business at the institute. Special thanks go to Prof. Dr.-Ing. Rolf Radespiel, head of Institute of Fluid Mechanics from the Technische Universität Braunschweig, for the encouragement regarding this research topic and for taking on the function of the second doctoral supervisor.

Many other people contributed to his work in ways both direct and indirect. Foremost of all I would like to mention PD Dr.-Ing. habil. Jochen Wild and to thank him for the many technical discussions, exchange of thoughts and corrections of my work. Moreover, I would like to thank Dr. Vlad Ciobaca for his everlasting support and for being a role model and friend in the course of our joint work at DLR and beyond. To all my colleagues at the institute and especially to those from the Transport Aircraft department, to be highlighted Jochen Kirz, Arno Ronzheimer, Sebastian Spinner, Dr.-Ing. Olaf Brodersen, Ruben Seidler, I owe thanks to the cooperative atmosphere and for all the great memories we share.

Apart from the DLR, my private life has also contributed to the success of this work. In this regard I would like to thank my parents for the relentless support that has made me who I am today and my wife Franziska, who supported me throughout the many evenings and weekends to achieve this goal.

Bremen, Juni 2022

Contents

List of Figures

List of Tables

Abbreviations

BPR	**B**y**P**ass **R**atio
BSW	**B**ackward **S**wept **W**ing
CAD	**C**omputer **A**ided **D**esign
CFD	**C**omputational **F**luid **D**ynamics
CRC	**C**ollaborative **R**esearch **C**enter
DFG	**D**eutsche **F**orschungs**g**emeinschaft
DLR	**D**eutsches Zentrum für **L**uft- und **R**aumfahrt
DoE	**D**esgin **o**f **E**xperiments
FOD	**F**oreign **O**bject **D**amage
FSW	**F**orward **S**wept **W**ing
GE	**G**eneral **E**lectric
MAC	**M**ean **A**erodynamic **C**hord
MTOW	**M**aximum **T**ake-**o**ff **W**eight
NASA	**N**ational **A**eronautics and **S**pace **A**dministration
OAD	**O**verall **A**ircraft **D**esign
OEI	**O**ne **E**ngine **I**noperative
ONERA	**O**ffice **n**ational d'**é**tudes et de **r**echerches **a**érospatiales
OWN	**O**ver **W**ing **N**acelle
OWME	**O**ver-the-**W**ing **M**ounted **E**ngine
QCR	**Q**uadratic **C**onstitutive **R**elation
RANS	**R**eynolds-**a**veraged **N**avier-**S**tokes
RR	**R**olls **R**oyce
RSM	**R**eynolds **S**tress **M**odel
sfc	**s**pecific **f**uel **c**onsumption

TFN	**T**hrough **F**low **N**acelle
TLAR	**T**op **L**evel **A**ircraft **R**equirements
TPS	**T**urbo **P**owered **S**imulator
UHBR	**U**ltra **H**igh **B**ypass **R**atio
UWN	**U**nder **W**ing **N**acelle
WB	**W**ing **B**ody
WBEP	**W**ing **B**ody **E**ngine **P**ylon
ZNT	**Z**ero **N**et **T**hrust

List of Symbols

Latin symbols

Symbol	Description	Dimension
C_D	Drag coefficient	–
C_L	Lift coefficient	–
D	Drag	N
E	Total specific energy	$\mathrm{J\,kg^{-1}}$
$\overline{\overline{F}}$	Flux density tensor	–
H	Total specific enthalpy	$\mathrm{J\,kg^{-1}}$
$\overline{\overline{I}}$	Unit tensor	–
L	Lift	N
La	Laval number	–
M	Mach number	–
Pr	Prandtl number	–
Pr_t	Turbulent Prandtl number	–
R	Specific gas constant	$\mathrm{J\,kg^{-1}\,K^{-1}}$
Re	Reynolds number	–
S	Control surface	$\mathrm{m^2}$
T	Temperature	K
T_t	Total temperature	K
V	Control volume	$\mathrm{m^3}$
$\vec{W}$	Vector of conservative flow variable	–
a	Speed of sound	$\mathrm{m\,s^{-1}}$

Continued on next page

Symbol	**Description**	**Dimension**
c	Chord length	m
c_{D}	Sectional drag coefficient	–
c_f	Skin friction coefficient	–
c_{L}	Sectional lift coefficient	–
c_p	Pressure coefficient	–
	Specific heat capacity at constant pressure	$\mathrm{J\,kg^{-1}\,K^{-1}}$
$c_{\mathrm{p,crit}}$	Critical pressure coefficient	–
c_v	Specific heat capacity at constant volume	$\mathrm{J\,kg^{-1}\,K^{-1}}$
e	Specific internal energy	$\mathrm{J\,kg^{-1}}$
g	Acceleration of gravity	$\mathrm{kg\,m\,s^{-2}}$
h	Vertical distance between wing and nacelle	m
h	Specific enthalpy	$\mathrm{J\,kg^{-1}}$
$\tilde{k}$	Mass-weighted turbulent kinetic energy	–
$\vec{n}$	Normal vector	–
p	Static pressure	Pa
p_{t}	Total pressure	Pa
q	Dynamic pressure	Pa
s	Half-span	m
t	Time	s
$\vec{u}$	Flow velocity vector	–
u	x-component of flow velocity	$\mathrm{m\,s^{-1}}$
u_τ	Shear stress velocity	$\mathrm{m\,s^{-1}}$
v	y-component of flow velocity	$\mathrm{m\,s^{-1}}$
w	z-component of flow velocity	$\mathrm{m\,s^{-1}}$
x	x-coordinate	m
x	Horizontal distance between wing and nacelle	m
y	y-coordinate	m
y^+	Dimensionless wall distance	–

Continued on next page

Symbol	Description	Dimension
y_n	Distance normal to the wall	m
z	z-coordinate	m

Greek symbols

Symbol	Description	Dimension
α	Angle of attack	$^\circ$
δ_{max}	Maximum layer thickness	m
ϵ	Area relation	–
κ	Adiabatic index	–
λ	Conductivity coefficient	$\mathrm{W\,m^{-1}\,K^{-1}}$
λ_t	Turbulent thermal conductive coefficient	$\mathrm{W\,m^{-1}\,K^{-1}}$
μ	Dynamic viscosity	$\mathrm{kg\,m^{-1}\,s^{-1}}$
μ_t	Artificial eddy viscosity	$\mathrm{kg\,m^{-1}\,s^{-1}}$
ν	Kinematic viscosity	$\mathrm{m\,s^{-2}}$
$\widetilde{\nu}$	Spalart–Allmaras variable	$\mathrm{kg\,m^{-1}\,s^{-1}}$
ρ	Density	$\mathrm{kg\,m^{-3}}$
σ_k	Closure variable related to the turbulent kinetic energy	–
τ	Shear stress	$\mathrm{kg\,m^{-1}\,s^{-2}}$
τ_t	Turbulent shear stress	$\mathrm{kg\,m^{-1}\,s^{-2}}$
τ_w	Wall shear stress	$\mathrm{kg\,m^{-1}\,s^{-2}}$
Φ	Arbitrary flow quantity	–
ω	Vorticity	$\mathrm{s^{-1}}$

Indices

Symbol	Description
$\overline{()}$	Time-averaged
$\widetilde{()}$	Favre-weighted average
$()'$	Fluctuation
$\vec{()}$	Vector
$\overline{\overline{()}}$	Tensor
c	Convective term
p	Pressure term
t	Turbulent flow
v	Viscous term
x	in x-direction
S	Sutherlands constant temperature
0	Local conditions
∞	Freestrean conditions

Operators

Symbol	Description	Dimension
$\otimes$	Cross product	
∇	Nabla operator	

1 Introduction

The current progress in the design of fuel-efficient passenger aircraft is largely based on developments by engine manufactures, since the wing and tube layout was not changed within the past decades. The latest single-aisle aircraft, operating on short and mid-range missions, are equipped with very-high-bypass ratio engines to achieve a significant specific fuel reduction due to the increasing bypass ratio, the ratio between bypass and core massflow. In the recent past, the impact of under-the-wing mounted engines is considered by an integrated wing design. This is possible due to years of experience and profound understanding of the interaction between under-wing nacelles (UWN) and wing. Thus, unexpected effects due to the engine installation can be eliminated. Nevertheless, the increasing bypass-ratio is accompanied by an increasing engine diameter because the core size cannot be reduced significantly and instead the bypass diameter needs to be adapted. Due to the constrained ground clearance, the option to install future, more efficient engines below the wing is challenging or even limited.

Therefore, different locations for the mounting of ultra-high bypass-ratio (UHBR) engines need to be investigated. Besides the installation at the rear fuselage, a familiar mounting position of business-jets, the engine installation above the wing at the wing trailing edge should be considered. The application of over-wing nacelles (OWN) was taken into account so far only rarely, nevertheless some commercial aircraft were and are equipped with OWN. The first successful implementation of OWN engines on a certified passenger aircraft was achieved in the 1970's by VFW-Fokker [4]. The latest example for an OWN configuration is the business jet configuration by Honda [5]. However, both configurations are equipped with engines featuring small bypass ratios and thus small engine diameters. For the application of OWN installation on large passenger aircraft, the impact of future UHBR engines needs to be evaluated to achieve a comparable aerodynamic knowledge of the associated installation effects, as for the UWN, especially in consideration of high-bypass ratio engines and transonic speed.

Previous investigations of OWN configurations have revealed complex aerodynamic interference phenomena between nacelle and upper-wing surface, but the cause and coherence were not described yet. The observations range from two sequential shocks on the wing upper surface over drag benefits on the nacelle up to improvements regarding the drag divergence Mach number, the maximum Mach number featuring a defined drag increment with increasing Mach number. Consequently, the interference between the transonic flow around the wing and an OWN causes multiple aerodynamic effects. These effects need to be understood to achieve an efficient UHBR engine integration with minimum risk during the design of future aircraft. In this regard, the present study will focus on the fundamental effects occurring from the close coupling of tube and wing aircraft and UHBR over-wing-nacelles.

A central role within the recent years of research can be assigned to Lockheed Martin, performing extensive investigations both numerically [6] [7] and experimentally [8] to demonstrate the aerodynamic potential of ultra-high bypass ratio (UHBR) OWN configurations. They stated a beneficial interference effect, which increases with increasing engine diameters [8]. However, a generalized description of the interference effects between OWN and wing at transonic flight conditions is not described yet. For this reason, the present work serves to investigate the interference effects between engine, streamtube and wing upper surface to build up a profound knowledge of the aerodynamic interactions. Thus, a deep understanding of the synergy and detrimental interference between over-the-wing mounted nacelles and transonic wings can be established for cruise flight conditions. Thereby, identification and comprehension of cause and effect are essential. Based on this knowledge, primal challenges in the aerodynamic design of an OWN configuration during cruise flight operation can be taken into account and avoided, which in turn enables the consideration of OWN configurations and accompanied benefits during the design of future aircraft. The impact of the OWN installation on the high lift capabilities requires his own and separate consideration.

1.1 State of the art

Today's large transonic operating commercial aircraft are characterized by a wing and tube layout with engines mounted below a backward swept wing. The general arrangement has not significantly changed within the past 60 years, but was continuously optimized. Improvements in manufacturing, materials, and multidisciplinary design processes implicated a continuous improvement. Moreover, accompanying processes of the airlines are tailored to this layout to achieve most economic operation. Examples for this are the easy access to maintain engines or efficient procedures at airports. However, this well understood layout offers hardly any possibilities for aerodynamic improvements. In the past decades, the development and utilization of methods, like computational fluid dynamics (CFD), enabled a detailed prediction of aerodynamic characteristics within the design process. Consequently, the aerodynamic performance could be further optimized for given constraints, e.g. spar height, closed coupled engine integration and design speeds. However, the latest developments of the two largest civil aircraft manufactures Airbus and Boeing, like the Airbus A320neo, Boeing 737MAX or A330neo, depend mainly on the improvements by engine manufactures, providing more efficient engines, while other promising technology developments, like (hybrid-)laminar flow, were not industrialized yet on current aircraft concepts to obtain significant aerodynamic improvements accordingly drag reductions. The aerodynamically efficient installation of new engines with larger diameters was achieved based on the existing generalized model, which describes the fundamental interference effects of UWN. Exemplary, a detailed description of engine/airframe interference for varying engine sizes can be found in [9]. In general, installing an engine below the wing leading edge affects both wing upper and lower surface. Comparing a wing-body (WB) and wing-body-engine-pylon (WBEP) configuration at identical angle of attack, an upstream shift of the shock position on the wing upper surface can be detected caused by a reduction of the local flow incidence induced by the engine. On the wing lower surface, the flow is disturbed by the pylon and a channel between nacelle, pylon and wing leads to a flow acceleration. Inboard of the nacelle, flow accelerations on the wing lower surface lead to an increased pressure level along the chord, which is associated with a local lift loss. Simultaneously, the pressure distribution on the upper surface features a small increase of the pressure level, but a distinct upstream shift of the shock location, resulting in an additional lift loss. The airfoil section outboard of the nacelle indicates only minimal variations along the wing lower surface. This can be addressed to the reduced overlap of nacelle and backward swept wing. But the wing upper surface indicates a distinct drop of the low pressure level in the supersonic segment in addition to an upstream shift of the shock location. The variation in the chordwise pressure distributions involves a decreasing local incidence, thus the UWN installation is accompanied by a reduced effective angle of attack α_{eff}. However, the decline of α_{eff} is not limited to the region around the UWN, but affects the full wing span. Consequently, the entire spanwise lift distribution is affected resulting in a distinct lift loss from wing root to tip. Consequently, the WBEP configuration has to operate at higher angles of attack to obtain the identical lift coefficient as the WB configuration. These interference effects of an UWN installation become more intense with increasing engine diameter.

The current progress towards a reduction of the specific fuel consumption (sfc) is largely based on an increasing bypass ratio (BPR) associated with a significant increasing engine diameter. For example the CFM International LEAP-1A engine features a BPR of about 11 and diameter of about 2.5m [10] [11]. Compared with the CFM56-5B4 [12], which is applied on the A320ceo, the bypass ratio was almost doubled and the engine diameter increased by 25%. The installation of more efficient but larger engines is challenging due to limited space between wing lower surface and ground. This constraint might lead to unusual nacelle designs, e.g. observable on the Boeing 737-300 [13] and the latest Boeing 737MAX, which features a non-symmetrical nacelle with flattened lower side, while the upper side extends above the wing leading edge. This indicates that the space limits below the wing are already reached. Consequently, engines with further increasing BPR>15, offering an improved efficiency, could probably not be mounted below the wing without a detrimental impact on the overall aircraft design and thus, the future development of more efficient aircraft necessitates extensive modifications of the current layout.

The limitation for the under-wing mounted engines necessitates the investigation of alternative engine mounting options. In the past, the consideration of OWN was occasionally investigated. With the aid of wind tunnel tests and numerical studies of OWN configurations, an aerodynamic proof of concept was confirmed. Some investigations actually resulted in a final aircraft design. A current example is the HondaJet [5], a small business jet for up to 6 passengers, which features GE Honda HF-120 engines with a BPR of 2.9 mounted on top of the wing to maximize the internal space of the fuselage. During the design of the aircraft, a beneficial impact of the OWN on the drag divergence Mach number was proven to increase the flight speed above the design point of about M=0.72 without a significant wave drag rise compared with the clean wing configuration [14].

Already in 1975 the VFW-Fokker VFW614 (see Fig. 1.1) celebrated its entry into service, taking the advantage of an OWN installation into account. The VFW614 [4] [15] was designed to transport up to 44 passengers over a range of 1200km. The OWN layout was driven exemplary by a minimum loading height, reduced risk of foreign object damage to operate on unpaved runways and an acoustic shielding of engine noise by the wing. However, the flight Mach number was limited to M=0.65 to exclude supersonic areas on the wing. The associated engine RR/SNECMA M45H is characterized by a maximum diameter of about 1m and BPR<3. The installation of the small OWN on the VFW614 affected the aerodynamics on the upper wing, but neither distinct beneficial nor detrimental aerodynamic performance variations could be detected. However, wind tunnel and flight tests during the design of the VFW614 exhibited a favorable effect of OWN engines on the high-lift performance and an increasing zero incidence lift in comparison with under-wing mounted engines. Nevertheless, the flow acceleration between rear wing upper surface and over-wing nacelle resulted in an increasing nose down pitching moment especially for engine idle. This aerodynamic feature was additionally reinforced by an increasing flight Mach number and might result in speed instabilities for M≥0.6 [16].

Fig. 1.1 *Experimental Aircraft ATTAS based on VFW 614 [1]*

Ensuing from the insights of the OWN installation on the VFW614, further investigations were initiated. Reubusch [17] performed wind tunnel tests for M=0.5...0.8 with a generic wing-body configuration and powered nacelles in the NASA Langley 16-ft transonic wind tunnel. The nacelles were located above the wing without a physical linkage to the aircraft model. The nacelle exit position was varied between wing leading and trailing edge. The force measurements revealed a beneficial interference on the wing-body drag due to the presence of the nacelle. However, the test setup was not able to capture detrimental effects on the nacelle.

Further investigations with an turbopowered simulator (TPS) were performed by *Szodruch* and *Kotschote* [18] on the basis of the VFW614 design. They stated, that intake and outlet flow of the engine affect the interference between airframe and nacelle. In addition, they claimed, that the longitudinal engine position is more relevant than the vertical engine position. A comparison between under- and over-wing mounted TPS revealed an improvement of maximum lift-to-drag ratio of 6.5% at take-off. However, these wind tunnel experiments focused on the engine installation above the wing leading edge resulting in a beneficial jet/wing interaction for high velocity ratios V_j/V_∞.

In the course of the development of the HondaJet, Honda designed the experimental aircraft MH02 [19]. This configuration is characterized by a high-wing and closed coupled over-the-wing mounted nacelles. Additionally, the wing features a forward sweep (12° at 25% chord). The engines are located on top of the junction between wing and fuselage and extend over the entire root chord length. This engine position was driven with respect to the center of gravity and a minimal lever arm in case of one-engine inoperative (OEI). Besides a minimization of foreign object damage (FOD), the over-wing position enabled the mounting of inconclusive engine diameters. However, significant interference drag of 0.002 was obtained in wind tunnels tests caused by the deviation of the spanwise lift distribution due to this particular, closed coupled OWN installation. Nevertheless, the basic idea to mount the engines on the wing instead of the fuselage of a business jet was maintained and later applied to the HondaJet [5].

Following, the installation of an OWN on the DLR-F6 configuration was investigated by Sasaki and Nakahashi [20]. Therefore, the through flow nacelle (TFN) of the DLR-F6 was positioned above the wing. By optimizing nacelle position, nacelle shape and wing shape, the overall aircraft performance with respect to L/D in cruise flight (M=0.7) was comparable to the UWN DLR-F6. Thereby, the drag evaluation of the OWN exhibited increasing pressure drag on fuselage and inboard wing. However, this was compensated by significant negative pressure drag values on the nacelle, leading to a comparable overall drag at constant lift for the OWN configuration.

In the past ten years, detailed investigations regarding the potential of OWN positoned at the wing trailing edge, especially with high bypass ratios (BPR>9), at transonic cruise conditions were carried out under the control of Lockheed Martin [6] [7] [8] [21]. Numerical investigations revealed a beneficial interference between large nacelles and wing for an OWN installed at a typical transport aircraft configuration with backward swept wings operating in the range of M=0.8. . . 0.85 [6]. Due to the location of the nacelle leading edge in the high velocity flow field above the wing, a negative drag component can be induced, resulting in a beneficial installation effect. However, the reaction of the nacelle on the wing results in strong variations of the flow characteristic above the wing associated with a significant interference drag of up to 60 drag counts (1 dct. $\widehat{=}$ 0.0001 C_D), which equals about one quarter of the overall drag for the WB configuration. Thus, a redesign of the wing is required to take the disturbance by the OWN into account and achieve finally an optimized configuration including a low drag wing design [6].

Based on these investigation by Hooker et al., over-wing mounted nacelles were applied on a hybrid wing body configuration, also known as blended wing body, which can be described as fixed wing aircraft without a clear separation line between wings and main body. Numerical investigations were performed to determine an optimized engine position along the wing trailing edge to achieve favorable interference drag of 1.2 dcts. compared with the isolated aircraft and isolated engine performance [7]. Subsequent, a wind tunnel test in the National Transonic Facility was performed by Lockheed Martin, NASA and the Air Force Research Laboratory [8] [21]. Two different through flow nacelle designs, representing the high bypass ratio turbofans Rolls-Royce Ultra Fan and the GEnX engine designed by GE, were manufactured and tested at three different positions. The wind tunnel results confirmed the beneficial interference drag due to the OWN installation at the wing trailing edge. Furthermore, the beneficial interference increases with the larger Ultra Fan nacelle. A comparison between the different engine positions revealed an increasing drag for under-wing and a decreasing drag for over-wing installations with increasing nacelle diameter. In addition, the impact of a varying engine massflow on the interference effects was investigated by using different plugs. The massflow variation of +/-15% resulted in minimal changes in total drag. Thereby, a decreasing drag with increasing massflow could be observed. In summary, this extensive investigation by Lockheed Martin in cooperation with various research partners was able to prove a beneficial interference drag between wing and over-the-wing mounted nacelles, for high-bypass ratio engines located at the wing trailing edge with the aid of simulations and cryogenic testing at high Mach numbers $M \approx 0.8$.

Motivated by the promising results of Lockheed Martin, the reference configuration 3 (REF3) was designed within the Collaborative Research Center (CRC) 880 funded by the German Research Foundation (DFG). This configuration, illustrated in Fig. 1.2, is the basis for investigations and explorations of various topics ranging from engine integration, circulation control for high lift to noise mitigation. In particular, the present research work is based on this aircraft configuration to investigate the aerodynamic interference between over-the-wing mounted engines and airframe. The overall aircraft design of REF3 was provided by Heinze [2] with the aid of the PrADO (Preliminary Aircraft Design and Optimization) tool [22]. The design is characterized by an UHBR OWN positioned at the trailing edge of a backward swept wing. This configuration features an attachment of the landing gear below the engines in an extended pylon fairing to prevent a tailstrike due to the resulting center of gravity. To address the unfavorable aerodynamic effects of the landing gear mounting, the reference configuration 4 (REF4) was designed. The defining difference between REF3 and REF4 is an alteration of the wing planfrom from a double-trapezoidal backward swept wing (REF3) towards a single-trapezoidal forward swept wing (REF4) as shown in Fig. 1.3. This modification allowed a landing gear attachment in the wing-belly junction due to the backward shift of the wing root, which resulted in a significantly shrinkage of the engine pylon in comparison with REF3. In addition, the modification allows laminar flow at transonic speed, which is not disturbed by an engine mounted in front of the wing. A combination of OWN and laminar flow is reasonable. A flight test of the VFW614 with a laminar glove indicated no impact of the OWN on the natural laminar flow along the wing upper surface [23].

Basic knowledge about the design of a forward swept configuration with the OAD tool PrADO was established in an extensive conceptual design study at the German Aerospace Center (DLR) leading to the LamAiR (Laminar Aircraft Research) configuration [24] [25]. During the evaluation of the aerodynamic characteristics with the aid of high-fidelity CFD, a strong inboard shock unsweep and high pre-shock Mach numbers were observed in cruise condition at $M=0.78$. By adaptation of the root airfoil, the shock was moved downstream and the pre-shock Mach number was reduced. This was achieved by an aft shift of the maximum thickness of the wing. Nevertheless, this region causes unsatisfying wave drag components especially for an increased Mach number of 0.8 resulting in significant reduction of lift-to-drag ratio in off-design conditions. In spite of this drawback, the forward swept wing offers several advantages. McGeer [26] predicted a potential improvement of induced drag by 10% by optimizing the wing planform.

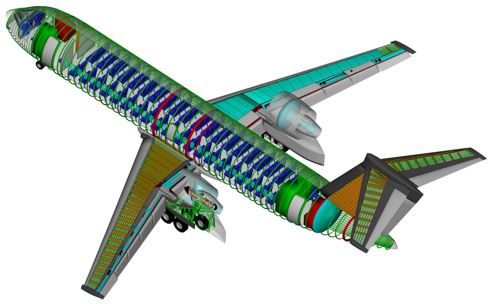

Fig. 1.2 *Sketch of REF3 based on OAD data [2]*

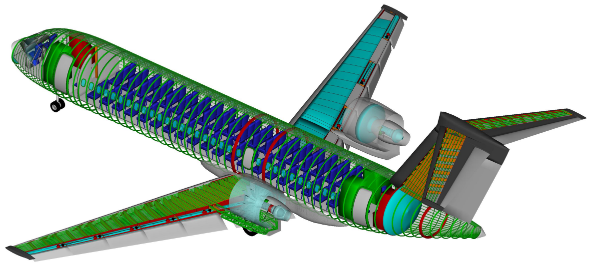

Fig. 1.3 *Sketch of REF4 based on OAD data [3]*

1.2 Objectives and outline

Beneficial effects due to OWN installations in transonic conditions were revealed by Lockheed Martin and Honda. Numerical and experimental investigations point out an overall drag benefit in cruise flight for ultra-high-bypass engines installed above the wing trailing edge in comparison with the under-wing mounting. In addition, the OWN position could increase the drag divergence Mach number and thereby improve the off-design performance. Besides these aerodynamic effects, other disciplines could take advantage of the over-wing mounted nacelle. For example, the wing could be used for acoustic shielding to reduce the fan noise propagation to the ground. Simultaneously, previous studies exhibit also detrimental effects on the aerodynamic characteristic of the wing due to an OWN. The alterations include shock position displacements, flow separations and influences on flight stability. These aerodynamic flow phenomena are accompanied by lift losses and drag increases. Nevertheless, aircraft with OWN, like the HondaJet or VFW614, demonstrate a successful realization of the general concept. But the latest studies from Lockheed Martin also expose the necessity to address the aerodynamic challenges, which correlates with the over-wing-nacelle installation.

The state of the art of research for OWN engine installations indicates that a fundamental and generalized characterization of the complex interference of wing upper surface and over-the-wing mounted engines is missing. Therefore, this thesis aims for an explanation of the mutual interference of an UHBR engine located above the trailing edge of a wing in transonic flow conditions. The study will be performed considering short-range transport aircraft configurations, designed carrying up to 100 passengers, in combination with UHBR engines. Thereby, not a through-flow nacelle is considered, but an entire powered engine including core engine and jet effects. A variation of the wing planform towards a forward swept configuration is carried out to reveal the impact of the OWN on the upstream located wing segment. The aim is to understand the interaction between engine and shock positions and the correlation between engine power setting and wing surface pressure

Fig. 1.4 provides a conceptual sketch of a model illustrating the interference between wing and OWN. The transonic wing is characterized by an area of supersonic flow ($M > 1$) covering more than half of the upper wing and concluding with a shock. The straight shock is characterized by a sudden increase of static pressure, density and temperature as well as a drop from supersonic to subsonic velocities. Moreover, shocks are in principal accompanied by energetic losses, thus a drag increment, which depends on the shock strength accordingly the pressure difference between left and right state of the shock. The flow along the upper wing interacts with a streamtube entering the engine, located above the wing trailing edge. The flow deceleration upstream the fan, operating in standard cruise conditions, is achieved through the engine inlet [13]. As a consequence, a positive pressure gradient dp/dx in upstream direction is induced. Since information are propagating in subsonic flow in both, upstream and downstream direction, the wing would be affected by the presence of the OWN and associated power setting. This pressure gradient might also affect the propagation of the supersonic flow ($M > 1$) by a displacement of the wing shock position in upstream direction. The interference effects between engine, streamtube and wing upper surface will be investigated to build up a profound understanding of this aerodynamic interaction outlined in Fig. 1.4.

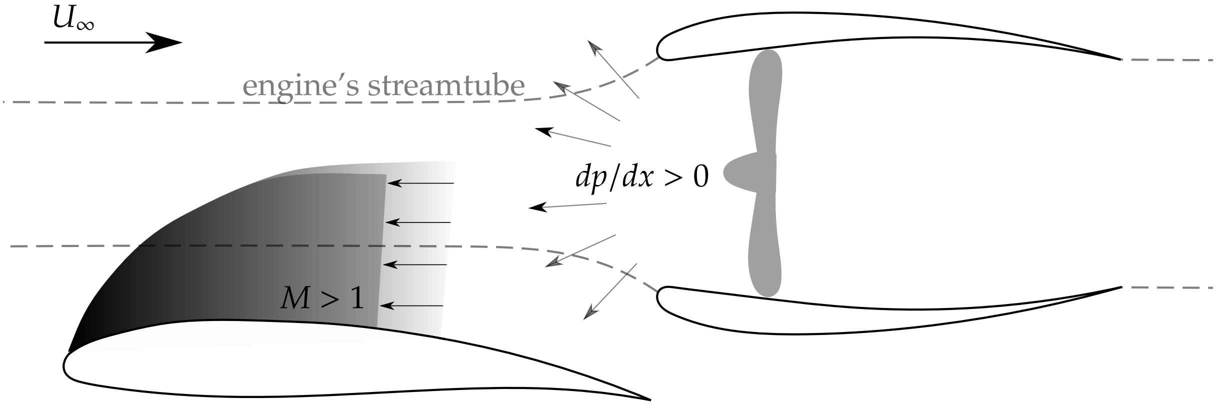

Fig. 1.4 *Sketch of OWN/wing interference*

Moreover, the spanwise propagation of the disturbance induced by the OWN needs to be evaluated. At the same time, the flow redirection around the wing with respect to the engine streamtube will be of interest. Conclusively, the investigation of a backward and forward swept wing planform enables a differentiation of the observed effects to build up general-purpose correlations. The evaluation of the backward swept wing affiliates the existing investigations and aims for a profound understanding regarding the impact of an OWN on the aerodynamic features on the wing, like shock position, pre-shock Mach number and local flow incidence by varying the engine's position and operating points. The additional investigations of an OWN in combination with a forward swept wing allows a verification of the previous obtained insights.

This work is divided in six chapters. At first, results of previous research activities are summarized and essential insights highlighted. Chapter 2 provides all necessary information about the numerical methods utilized for flow simulation, grid generation, optimization, and evaluation. Thereby, the validity of the selected settings is demonstrated. Chapter 3 describes the overall aircraft design of REF3 and REF4. Besides general aircraft specifications, the aerodynamic characteristics of isolated backward and forward swept wings are shown exemplary on the basis of the wing-body configurations of REF3 and REF4. Chapter 4 focuses on aircraft configuration REF3. Initially, basic features of the OWN installation are described. Subsequently, a variation of the thrust setting provides evidence to clarify whether the actual presence of a displacement body or the variable adverse pressure gradient depending on the engine setting dominates the wing pressure distribution. Additionally, the impact of the engine position on the wing aerodynamics is investigated with the aid of a surrogate-based model approach. For this purpose, the variation of the aerodynamic coefficients and their physical cause is taken into account. The results for REF4 are presented in chapter 5, analog to chapter 4. However, it should be noted that the redesign of REF4 enabled a larger parameter space for the engine position variation and thus an extended significance to describe the impact of the OWN position on the aerodynamic wing characteristic. The additional benefit of utilizing laminar flow to reduce drag will not be taken into account in the course of this work. The 6th chapter summarizes and discusses the findings and evaluates the aerodynamic potential of OWN configurations while highlighting key findings.

Concluding, this investigation contributes to the fundamental understanding of OWN installation effects. Based on the resulting knowledge concerning the aerodynamic characteristics occurring through the interference between OWN and wing, the full potential of an OWN configuration can be exploited in future aircraft designs.

2 Numerical methods

The following section deals with the numerical tools and associated methods utilized within this work. Basic principles of the CFD solver DLR *TAU*-code [27] will be presented. The characteristics of the commercial grid generator *Centaur* will be highlighted. In addition, the drag prediction tools *AeroForce* [28] and *ffd00* [29] will be outlined. Finally, a tool verification to specify a valid setup for the subsequent investigations and the optimization framework *POT* [30] will be presented.

2.1 High-fidelity RANS simulation with DLR TAU-code

The present study utilizes the DLR *TAU*-code [27], which solves the three-dimensional, compressible Reynolds-averaged Navier-Stokes (RANS) equations with the aid of a finite-volume approach. The solver is based on an edge-based dual-cell approach. Thus, the RANS-equations are solved within control volumes, which are constructed around the vertices of the grid by connections between the surrounding grid cell centers and cell face centers. In the following, fundamental equations building the basis for the RANS equations will be outlined based on the comprehensive overview by Blazek [31].

2.1.1 Governing equations

The numerical investigation of aeronautical applications are typically based on the conservative laws of fluid mechanics, considering the atmosphere as a continuum. Moreover, air can be characterized as Newtonian fluid. Thus, the Navier-Stokes equations can be utilized for this type of application. Those include a general description of mass, momentum and energy conservation over an an arbitrary control volume V. Assuming a fixed volume V in time and space and neglecting body forces and heat transfer, the integral equation can be written as

$$\iiint_V \frac{\delta}{\delta t}\vec{W}dV + \iint_S \overline{\overline{F}} \cdot \vec{n}dS = 0, \qquad \vec{W} = \begin{bmatrix} \rho \\ \rho\vec{u} \\ \rho E \end{bmatrix} \tag{2.1}$$

The first addend contains the temporary change of the vector of conservative flow variables $\vec{W}$ within the control volume V. The second addend describes the fluxes over the control volume's surface S by the product of the flux density tensor $\overline{\overline{F}}$ and the local normal vector $\vec{n}$ of the surface element dS. Thereby, the temporal change of the flow state within the control volume equates to the fluxes over the control surface. The vector $\vec{W}$ assembles five properties composed of the mass flow, expressed by the density ρ, the momentum, which results from the product of density and flow velocity $\vec{u} = [u, v, w]^T$, and the energy, defined by density times total specific energy E. The flux density tensor $\bar{\bar{F}}$ consist of two parts, a convective part $\bar{\bar{F}}_c$ and a viscous part $\bar{\bar{F}}_v$:

$$\bar{\bar{F}} = \bar{\bar{F}}_c - \bar{\bar{F}}_v \tag{2.2}$$

$$\bar{\bar{F}}_c = \begin{bmatrix} \rho\vec{u} \\ \rho\vec{u} \otimes \vec{u} + \bar{\bar{I}}p \\ \rho H\vec{u} \end{bmatrix} \quad \text{and} \quad \bar{\bar{F}}_v = \begin{bmatrix} 0 \\ \bar{\bar{\tau}} \\ \vec{u}\bar{\bar{\tau}} + \lambda\nabla T \end{bmatrix} \tag{2.3}$$

In addition, some further relations will be introduced to solve the above equations. In case of a civil transport aircraft, a calorically perfect gas can be assumed as working fluid. This results in the following correlation between pressure p, density ρ, specific gas constant R and temperature T

$$p = \rho R.T \tag{2.4}$$

The total specific enthalpy H is expressed by

$$H = E + \frac{p}{\rho}. \tag{2.5}$$

Furthermore, The total energy E can be split into internal energy $e = c_v T$ and kinetic energy $u^2 + v^2 + w^2/2$. Thus, the total specific enthalpy is then derived by

$$H = c_v T + \frac{1}{2}\vec{u}^2 + \frac{p}{\rho}. \tag{2.6}$$

Combining (2.5) and (2.6) including the definition of the specific gas constant R

$$R = c_p - c_v = \left(\frac{\kappa - 1}{\kappa}\right) c_p \tag{2.7}$$

and the adiabatic index $\kappa = c_p/c_v$ results in the following expression of the total specific energy E through the flow quantities pressure p, density ρ and velocity $\vec{u}$

$$E = \frac{1}{\kappa - 1}\frac{p}{\rho} + \frac{\vec{u}^2}{2}. \tag{2.8}$$

Because of the assumption of a Newtonian fluid, implying a linear correlation between shear stress and shear strain rate, the shear stress tensor $\bar{\bar{\tau}}$ can be expressed by the dynamic viscosity μ and the spatial velocity derivative $\nabla \otimes \vec{u}$.

$$\bar{\bar{\tau}} = \mu\left(\nabla \otimes \ \vec{u} + (\nabla \otimes \vec{u})^T - \frac{2}{3}(\nabla \cdot \vec{u})\bar{\bar{I}}\right) \tag{2.9}$$

The dynamic viscosity μ depends on the temperature T. The correlation is given by Sutherland's law

$$\frac{\mu}{\mu_\infty} = \left(\frac{T}{T_\infty}\right)^{3/2} \frac{T_\infty + T_S}{T + T_S} \tag{2.10}$$

with $T_S = 110.4K$ for $T_\infty = 273.15K$.

Finally, the heat flux can be determined based on the constant specific heat capacity at constant volume c_v in combination with the thermal conductivity coefficient λ and the Prandtl number being set to $Pr = 0.72$ for air

$$Pr = \frac{\mu \kappa c_v}{\lambda} \tag{2.11}$$

describing the relation between viscous and thermal diffusion rate.

2.1.2 Reynolds-averaged Navier-Stokes equations

The previous section summarized the basic equations providing a system of nonlinear, partial differential equations on the assumption of a calorically prefect gas. However, an analytic solution for the Navier-Stokes equations only exists for specific flow phenomena [32]. Therefore, a numerical approach is applied for complex aerodynamic problems, which requires a time and space dependent discretization of the flow field. In the past decades, several methods with varying accuracy and turbulence modeling efforts were developed. For example, the highest level of effort is required for the direct numerical simulation (DNS). However, the application of this method for complex flows is too costly. The required performance of current supercomputers limits the use to simple flow features at low Reynolds numbers Re, because the computational expense of the turbulent term scales with Re^3. In most cases, a resolution of all scales of turbulence is not necessary to evaluate an aerodynamic problem on aircraft level and thus can be approximated by modeling. Dependent on the extent of modeling, a partly approximation of small scale turbulence in combination with resolved large eddies up to a full turbulence modeling over the entire bandwidth of turbulent scales can be utilized to reduce the computational costs. For the turbulence approximation, Reynolds suggested in 1895 a decomposition of the time and space dependent flow quantity Φ into a time-averaged mean flow $\overline{\Phi}$ and a turbulent fluctuation Φ'.

$$\Phi = \overline{\Phi} + \Phi' \tag{2.12}$$

The time average of the fluctuating part is zero $\left(\overline{\Phi'} = 0\right)$, while the time-average of a product of two fluctuating quantities can differ from zero

$$\overline{\Phi_i' \Phi_j'} = \overline{\Phi_i \Phi_j} - \overline{\Phi_i \Phi_j} \neq 0. \tag{2.13}$$

Besides the Reynolds-averaging approach, the so called Favre-averaging must be applied for certain flow quantities in case of compressible flows ($\rho \neq const.$). This approach is based on a mass-weighted averaging method taking the fluctuation in density and the associated non-linear terms into account.

$$\Phi = \widetilde{\Phi} + \Phi'', \qquad \text{with} \qquad \overline{\rho}\widetilde{\Phi} = \overline{\rho\phi} \tag{2.14}$$

Note, the Favre-weighted average of the fluctuations is zero ($\widetilde{\Phi''} = 0$), and the time-averaged is unequal zero ($\overline{\Phi''} \neq 0$). Following, the Favre- and Reynolds-averaged Navier-Stokes equations are defined by:

$$\iiint_V \frac{\delta}{\delta t} \overline{\vec{W}} dV + \iint_S \overline{\overline{\overline{F}}} \cdot \vec{n} dS = 0 \tag{2.15}$$

also known as Reynolds-averaged Navier-Stokes equations (RANS). The resulting flow variable $\overline{\vec{W}}$ and flux density tensor $\overline{\overline{\overline{F}}}$ due to the Reynolds- and Favre-averaging is given by:

$$\overline{\vec{W}} = \begin{bmatrix} \overline{\rho} \\ \overline{\rho}\widetilde{\vec{u}} \\ \overline{\rho}\widetilde{E} \end{bmatrix}, \qquad \text{and} \qquad \overline{\overline{\overline{F}}} = \overline{\overline{\overline{F_c}}} - \overline{\overline{\overline{F_v}}} \tag{2.16}$$

with the convective $\overline{\overline{\overline{F_c}}}$ and viscous $\overline{\overline{\overline{F_v}}}$ part of the flux density tensor

$$\overline{\overline{\overline{F_c}}} = \begin{bmatrix} \overline{\rho}\widetilde{\vec{u}} \\ \overline{\rho}\widetilde{\vec{u}} \otimes \widetilde{\vec{u}} + \overline{\rho\vec{u}'' \otimes \vec{u}''} + \overline{\overline{I}}\overline{p} \\ \overline{\rho}\widetilde{H}\widetilde{\vec{u}} + \overline{\rho\vec{u}''h''} + \overline{\rho\vec{u}'' \otimes \vec{u}''}\widetilde{\vec{u}} + 1/2\overline{\rho\vec{u}''\left(\vec{u}'' \otimes \vec{u}''\right)} \end{bmatrix} \qquad \text{and} \qquad \overline{\overline{\overline{F_v}}} = \begin{bmatrix} 0 \\ \overline{\overline{\overline{\tau}}} \\ \widetilde{\vec{u}}\overline{\overline{\overline{\tau}}} + \overline{\overline{\overline{\tau}}\vec{u}''} + \lambda\nabla\widetilde{T} \end{bmatrix}. \tag{2.17}$$

By introducing the mass-weighted averaged turbulent kinetic energy $\widetilde{k} = 1/2\widetilde{\vec{u}''\vec{u}''}$, the Favre-averaged total energy $\widetilde{E}$ and total enthalphy $\widetilde{H}$ is defined by:

$$\widetilde{E} = \widetilde{e} + \frac{\widetilde{U}^2}{2} + \widetilde{k} \qquad \text{and} \qquad \widetilde{H} = \widetilde{h} + \frac{\widetilde{U}^2}{2} + \widetilde{k}. \tag{2.18}$$

The derived equations are formally comparable with the Navier-Stokes equations, including three additional terms representing the fluctuating quantities.

- $\overline{\rho\vec{u}'' \otimes \vec{u}''}$ comprises the Reynolds stress tensor and describes the transfer of momentum induced by the turbulent fluctuations. The tensor is symmetric and features six independent components, whereas the elements on the diagonal represents turbulent normal stresses;
- $\overline{\rho\vec{u}''h''}$ represents the turbulent transport of heat;
- $\overline{\overline{\overline{\tau}}\vec{u}''} - 1/2\overline{\rho\vec{u}''\left(\vec{u}'' \otimes \vec{u}''\right)}$ describes the turbulent diffusion, thus the transformation of turbulent kinetic energy into heat. The molecular diffusion is represented by the first term, while the second term describes the turbulent transport of turbulent kinetic energy.

However, the Favre- and Reynolds- averaged equations are not a closed system of equations since the terms $\overline{\Phi_i''\Phi_j''}$ do not vanish. As a consequence, additional relations must be supplied. The necessary conservative formulation of the Reynolds stresses introduces higher order correlations, which makes the direct closure of the RANS-equations impossible.

In order to close this fundamental closure problem two approaches are available. On the one hand, the six components of the symmetric Reynolds stress tensor can be computed at the cost of seven additional equations. This approach provides a second-order closure model and is called Reynolds stress model (RSM). The RSM represents the currently most complex strategy of the classical RANS turbulence models. One the other hand, first-order closure models can be applied, called eddy viscosity models. These models require a significantly reduced computational effort to approximate the flow turbulence. The most common eddy viscosity models rely on a linear relation between turbulent shear stress and the mean strain rate, which is based on Boussinesq's hypothesis.

$$\overline{\overline{\tau_t}} = -\overline{\rho \vec{u}'' \otimes \vec{u}''} = \mu_t \left(\nabla \otimes \widetilde{\vec{u}} + \left(\nabla \otimes \widetilde{\vec{u}} \right)^T - \frac{2}{3} \overline{\overline{I}} \left(\nabla \cdot \widetilde{\vec{u}} \right) \right) - \frac{2}{3} \overline{\overline{I}} \left(\overline{\rho} \widetilde{k} \right) \tag{2.19}$$

The proportionality between the turbulent shear stress tensor $\overline{\overline{\tau_t}}$ and the mean strain rate tensor is given by the artificial eddy viscosity μ_t. This parameter needs to be evaluated by additional equations based on local flow properties and geometrical characteristics.

In similarity to the Reynolds analogy, the turbulent transport of heat within the energy equation is defined by:

$$\overline{\rho \vec{u}'' h''} = -\lambda_t \nabla \widetilde{T} \tag{2.20}$$

with the turbulent thermal conductivity coefficient λ_t

$$\lambda_t = c_p \frac{\mu_t}{Pr_t}. \tag{2.21}$$

The turbulent Prandtl number Pr_t is assumed constant over the flow field at $Pr_t = 0.9$ for air.

The turbulent diffusion within the energy equation is sometimes neglected for the turbulence modeling. In case the molecular diffusion and the turbulent transport of turbulent kinetic energy is considered, the term is for example described by:

$$\overline{\overline{\overline{\tau}} \vec{u}''} - \frac{1}{2} \overline{\rho \vec{u}'' \left(\vec{u}'' \otimes \vec{u}'' \right)} = \left(\mu_t + \frac{\mu_t}{\sigma_k} \nabla \widetilde{k} \right) \tag{2.22}$$

whereas σ_k represents a quantity associated with the turbulent kinetic energy, which depends on the chosen turbulence model.

Finally, after the application of the Boussinesq hypothesis in combination with the RANS equations two unknown are remaining, the eddy viscosity μ_t and the turbulent kinetic energy $\widetilde{k}$. The determination of these unknowns is dependent on the turbulence model. Using one-equation turbulence models, one additional transport equation is solved for either the turbulent kinetic energy or the eddy viscosity. In case of two-equation turbulence models, usually the turbulent kinetic energy plus a variable describing the scale of turbulence are evaluated. In the following, the utilized turbulence models are described.

Spalart-Allmaras turbulence model

The turbulence model by Spalart and Allmaras is the basis for today's state of the art turbulence modeling and widely used [33] [34]. It considers one additional transport equation to solve the quantity $\widetilde{\nu}$, which is related to the eddy viscosity μ_t. The model builds up a relation between the vorticity of the flow and the production of turbulence. Thus, the new transport quantity $\widetilde{\nu}$ is derived from the eddy viscosity:

$$\widetilde{\nu} \sim \frac{\mu_t}{\rho} \tag{2.23}$$

In addition, a differentiation between viscous regions and the free flow is introduced with the aid of the function f_{v1}:

$$\mu_t = \rho\widetilde{\nu} f_{v1} \text{ with } f_{v1} = \frac{X^3}{X^3 + c_{v1}^3} \text{ and } X = \frac{\rho\widetilde{\nu}}{\mu} \tag{2.24}$$

The transport equation for the viscosity variable $\widetilde{\nu}$ in integral notation is expressed by:

$$\begin{aligned} &\iiint_V \frac{\delta\rho\widetilde{\nu}}{\delta t} + \iint_S \left(\rho\widetilde{\nu}\left(\vec{\widetilde{u}} - \vec{\lambda}_b\right) - \left(\frac{\mu_l + \rho\widetilde{\nu}}{\sigma}\right)\nabla\widetilde{\nu}\right) \cdot \vec{n} dS \\ = &\iiint_V \left(c_{b1}\left(1 - f_{t2}\right)\widetilde{S}\rho\widetilde{\nu} + \frac{c_{b2}}{\sigma}\nabla\left(\rho\widetilde{\nu}\right) \cdot \nabla\widetilde{\nu} - \left(c_{w1} f_w - \frac{c_{b1}}{k^2} f_{t2}\right)\rho\frac{\widetilde{\nu^2}}{y_n^2}\right) dV \end{aligned} \tag{2.25}$$

The left hand side of the transport equation is composed of a temporal change within the control volume V and the convective and diffusion fluxes over the control surface S for the variable $\widetilde{\nu}$. The right hand side introduces a source term, which includes a proportional relation between the production term $c_{b1}\left(1 - f_{t2}\right)\widetilde{S}\rho\widetilde{\nu}$ and the vorticity ω plus a correction term for viscous near-surface flows dependent on the nearest wall distance d:

$$\widetilde{S} = \left|\overline{\overline{\omega}}\right| + \frac{\rho\widetilde{\nu}}{k^2 d^2} f_{v2} \text{ with } \overline{\overline{\omega}} = \nabla \otimes \vec{\overline{u}} - \left(\nabla \otimes \vec{\overline{u}}\right)^T \tag{2.26}$$

Furthermore, the model introduces three damping functions:

$$f_{v1} = \frac{X^3}{X^3 + c_{v1}^3}; f_{v2} = 1 - \frac{X}{1 + X f_{v1}}; f_w = g\left(\frac{1 + c_{w3}^6}{g^6 + c_{w3}^6}\right)^{1/6} \tag{2.27}$$

with

$$X = \frac{\widetilde{\nu}}{\nu_t}; g = r + c_{w2}\left(r^6 - r\right); r = \frac{\widetilde{\nu}}{\widetilde{S} k_s^2 y_n^2}. \tag{2.28}$$

Finally, the constants used the turbulence modeling are defined as:

$$\begin{aligned} c_{b1} = 0.1355, c_{b2} = 0.622, \sigma = \frac{2}{3}, \\ k = 0.41, c_{v1} = 7.1, c_{w1} = \frac{c_{b1}}{k^2} + \frac{1 + c_{b2}}{\sigma}, \\ c_{w2} = 0.3, c_{w3} = 2 \end{aligned} \tag{2.29}$$

There are several extension of the standard SA turbulence model available. In the following, two widely used versions will be highlighted, first the Negative Spalart-Allmaras One-equation model (SA-neg). This formulation is identical with the original SA turbulence equations for $\widetilde{\nu} \geq 0$, but fixes μ_t to zero and solves a slightly adapted set of equations in case of $\widetilde{\nu} < 0$ [34]. Second, the Spalart-Allmaras One-equation model with quadratic constitutive relation (QCR) describes a nonlinear model version. This is obtained by adding to the linear Boussinesq relation an antisymmetric normalized rotation tensor to improve the eddy-viscosity approximation [35].

Reynolds stress model

The second-order closer model is not relying on the Boussinesq hypothesis to approximate the Reynolds stresses, instead the Reynolds stress turbulence models solve the differential transport equation. Thus, complex flows can be predicted more accurate by computing each component of the Reynolds stress tensor individually. Consequently, the anisotropic characteristic of turbulent flows is considered. In particular the SSG/LRR-$\ln\omega$ turbulence model was utilized in this work. This model is a combination of the Speziale-Sarkar-Gatski (SSG) pressure strain model and the Launder-Reece-Rodi (LRR) model for near-surface flows. The turbulent length scale is provided by Menter's BSL-ω-equation. The transport equation of the SSG/LRR-ω model is composed of six terms. The production term $\overline{\rho}P_{ij}$ is exact, because the mean flow velocities and Reynolds stresses are given by the equation system. Moreover, the system rotation term $\overline{\rho}F_{ij}$ can be computed exactly. Instead, the pressure strain correlation $\overline{\rho}\Phi_{ij}$, dissipation term $\overline{\rho}\epsilon_{ij}$, and viscous diffusion term $\overline{\rho}D_{ij}$ require modeling. The last term, the mass flux term $\overline{\rho}M_{ij}$, representing compressible effects, is neglected. As a result, the transport equation for the six independent Reynolds stresses is given by:

$$\begin{aligned} &\frac{d}{dt}\iiint_V \overline{\rho}\widetilde{u_i''u_j''}dV + \iint_S \overline{\rho}\widetilde{u_i''u_j''}\left(\widetilde{\vec{u}-\vec{\lambda}_b}\right)\cdot\vec{n}dS \\ &= \iiint_V \left(\overline{\rho}P_{ij} + \overline{\rho}\Phi_{ij} + \overline{\rho}\epsilon_{ij} + \overline{\rho}D_{ij} + \overline{\rho}F_{ij}\right)\cdot dV. \end{aligned} \tag{2.30}$$

For the closure of the equation system, an additional transport equation is necessary. In case of the SSG/LRR-$\ln\omega$ model, a blending between the ϵ-equation outside the boundary layer and Wilcox' ω-equation near the wall was chosen following the approach of Menter, where the isotropic dissipation rate is defined by

$$\epsilon = C_\mu\widetilde{k}\omega \qquad \text{with} \qquad C_\mu = 0.09 \tag{2.31}$$

whereas the specific kinetic energy $\widetilde{k}$ depends on the specific Reynolds stress component $\widetilde{R_{ij}}$

$$\widetilde{k} = \frac{1}{2}\widetilde{R_{ij}} \tag{2.32}$$

Finally, the length scale is provided by $\ln\omega$, thus the dependency of the solution on the $y^+(1)$ resolution is reduced. More details concerning the RSM turbulence modeling can be found in [36].

Boundary conditions

In order to solve the system of equations suitable boundary conditions have to be defined, since the numerical simulation considers only selected parts of the physical domain. Along these artificial boundaries of the computational domain, physical quantities, like pressure, temperature or velocity, need to be specified. These include exemplary the farfield boundary, symmetry plane as well as engine inlet and outlet faces. [31]

Following, the selected engine boundary condition is described in more detail [37]. Within the present work, the pressure ratio p_t/p_0 and temperature ratio $T_t/T_{t,0}$ are specified for the engine outlet face. Thereby, p_0 and $T_{t,0}$ describe the local flow conditions on the outlet planes. Based on these information and in combination with the free stream flow quantities, the density at the engine outlet face can be computed. The Mach number on the engine outlet face is determined using the isentropic relationship

$$M = \sqrt{\left[\left(\frac{p_t}{p_0}\right)^{\kappa-1/\kappa} - 1\right] \cdot \frac{2}{\kappa - 1}}. \tag{2.33}$$

Thus, the necessary physical conditions on the boundary face are defined. Moreover, the knowledge about density and flow velocity enables the calculation of the outlet mass flow, which is represented by the integral value over all boundary nodes of the engine outlet face.

The resulting mass flow $\dot{m}$ is then used as input variable for the engine inlet face. Note, in case of several outlet planes, e.g. core and bypass, the sum over all outlet faces is taken into account for a correct balancing between engine inlet and outlet. As additional parameters, the area relation

$$\epsilon_{Fan} = \frac{A_\infty}{A_{Fan}} = \frac{\dot{m}}{A_{Fan} \cdot M_\infty \cdot \sqrt{\kappa \cdot p_\infty \cdot \rho_\infty}} \tag{2.34}$$

and Laval number

$$La = \sqrt{\frac{(\kappa + 1) \cdot M^2}{(\kappa - 1) \cdot M^2 + 2}} \tag{2.35}$$

are introduced for the inlet face. Finally, starting from an initial static pressure on the inlet face, La is adapted in an iterative process until the inlet and outlet mass flow match.

2.1.3 Spatial and time discretization

The discretization of the computational domain into a finite number of control volumes defines the maximum flow resolution. Assuming a constant flow variable for a fixed control volume in space and time, the temporal change of the conservative flow variable $\vec{W}$, (2.1) is defined by:

$$\frac{\delta}{\delta t}\vec{W} = -\frac{1}{V} \iint_S \overline{\overline{F}} \cdot \vec{n} dS. \tag{2.36}$$

$\iint_S \overline{\overline{F}} \cdot \vec{n} dS$ denotes the convective and viscous fluxes over the boundary of the control volume. Thus the change of the flow variables within a control volume is defined by the fluxes over the boundary faces. These fluxes are for instance computed by finite difference formulations.

For the present study, both the convective and viscous fluxes were derived by a second order central scheme in combination with matrix dissipation. This implies that the fluxes are determined by the average of fluxes between neighboring control volumes. However, the simple consideration of the flux averages over the adjacent cells without any information about the directional propagation can result in instabilities. For an improved numerical stability, artificial dissipation is introduced and added to the convective flux. In this particular case matrix dissipation [38] was used, which is an extension of the scalar dissipation approach presented by Jameson, Schmidt and Turkel. It combines second and forth difference terms depending on the local flow characteristic. The second difference term is activated by a pressure sensor in regions with large pressure gradients, like shocks. Thereby, the scheme is switched to a first-order approach reducing the risk of overshoots. The remaining flow field is covered by the second-order accurate forth difference scheme to improve the stability with a minimal amount of dissipation. For the matrix dissipation scheme, the scalar dissipation is additionally extended by individual scaling factors extracted from the convective flux Jacobian instead of one scaling factor for the scalar dissipation, defined by the maximum eigenvalue of the the matrix. Thus, the dissipative terms of each governing equation is multiplied by appropriate eigenvalues leading to a minimized artificial dissipation [31].

Besides the spatial discretization, a discretization in time is essential to solve the time-dependent equations starting from a known initial state until a final steady solution is achieved. In principal, a distinction is made between explicit and implicit schemes. The explicit time-integration, for example Runge-Kutta [39], is characterized by an easy implementation and a moderate amount of computer memory. However, the maximum time-step is limited by the Courant-Friedrichs-Levy (CFL) condition due to stability limitations [40]. Especially for viscous flows and highly stretched grid cells, the required number of iterations increases significantly until a converged steady state is reached. In contrast, the implicit time-integration enables considerably larger time steps without causing instabilities. Thus, less iterations are required to achieve a converged solution. Nevertheless, the implementation is more difficult and the computational effort per iteration is usually higher in comparison with an explicit scheme [31]. For this work, the Backward-Euler implicit time-stepping scheme is applied. The associated system of equations is solved with the aid of the Lower-Upper Symmetric Gauss-Seidel (LUSGS) method [41].

In addition, a multigrid method and local time stepping was utilized to accelerate the convergence [31]. The utilization of multigrid allows for the simulation on a series of derived coarser grids. Thereby, the solution updates from the coarse grids are combined and added with the solutions of the finer grids. The solving of the governing equations on coarser grids can accelerate the achievement of a steady-state on the finest grid. The local time stepping considers the largest possible local time step for the integration of the governing equation with respect ot the size of each control volume. Thus, the convergence is accelerated. However, before obtaining a steady-state result the transient solutions are not temporally accurate. To guarantee a comparability between all results, the Cauchy convergence criterion was activated, monitoring the drag coefficient. The allowed absolute error within 750 iterations was limited to $\Delta C_D = 0.00001$.

2.2 Hybrid grid generation with Centaur

Hybrid grids are composed of prismatic/hexahedral elements and pyramidal/tetrahedral elements. The near surface volume is covered by prismatic/hexahedral elements to obtain a detailed spatial discretization, e.g. to resolve the boundary layer flow and high flow gradients. The pyramidal/tetrahedral elements are used to fill the remaining regions with a minimum number of nodes. The grids for all configurations were created with the commercial grid generator Centaur by CentaurSoft [42]. The grid generator is characterized by a fast and stable grid generation process to later resolve complex three-dimensional flows with a RANS solver. The hybrid grids is based on a mainly unstructured surface grid leading to structured prism layers for the resolution of the near-surface flow. The remaining flow field is covered by tetrahedral elements. To guarantee a sufficient and smooth boundary layer resolution by the prism layers, an initial cell spacing and stretching ratio in wall-normal direction can be defined. The size of the initial cell spacing y_n needs to assure a dimensionless wall distance $y^+ < 1$. This dimensionless parameter is defined by

$$y^+ = \frac{y_n u_\tau \rho}{\mu} \tag{2.37}$$

using the shear stress velocity u_τ

$$u_\tau = \sqrt{\frac{\tau_w}{\rho}} \tag{2.38}$$

and wall shear stress τ_w

$$\tau_w = \frac{1}{2} \cdot c_f \cdot \rho \cdot u^2 \tag{2.39}$$

An empirical estimation of the skin friction coefficient c_f can be found exemplary in [32]. The maximum layer thickness can be estimated by

$$\delta_{max} = 0.37 \frac{l_{ref}}{Re^{0.2}}. \tag{2.40}$$

The stretching ratio in combination with the number of prism layers needs to be selected to build a total height of the prisms layers, which at least have to cover the approximated boundary layer thickness. Besides global parameters controlling the size of surface, prism and tertrahedral cells, local flow refinements can be defined within Centaur by using geometric sources in form of e.g. spheres, hexahedrons and cylinders. These sources are applied to actively manage mesh properties in selected regions. Thereby, the cell size and growth rate of surface, prism and tetrahedral cells can be controlled within the affected source area. Thus additional spatial refinements, for example due to high flow gradients along the wing leading edge, could be achieved. For this work, the so-called *CATIA-to-Centaur Sources* were utilized. These sources enable a direct linkage between the computer aided design (CAD) environment CATIA and the geometric grid-sources used by Centaur by defining the sources by a direct linkage along the geometric model as shown by the magenta lines and surfaces in Fig. 2.1 and Fig. 2.2. As a result, geometrical modification leads to an automatic adaptation of the grid-source location. Thereby, the comparability between the grids for various configurations and geometry variations is significantly improved and uncertainties through the grid generation minimized. In the course of the present investigation, the engine position was significantly changes (e.g. $\Delta X > 800mm$), which is accompanied by modifications of the pylon shape and wing-pylon junction. Thereby. local refinements along the nacelle highlight and junctions could be maintained.

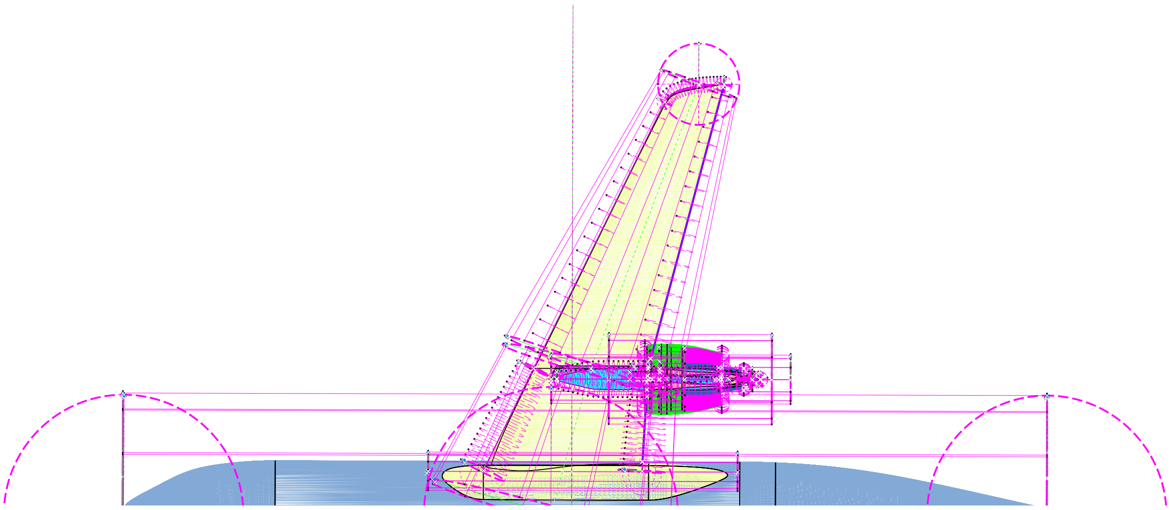

Fig. 2.1 *Geometric sources defined in CATIA V5*

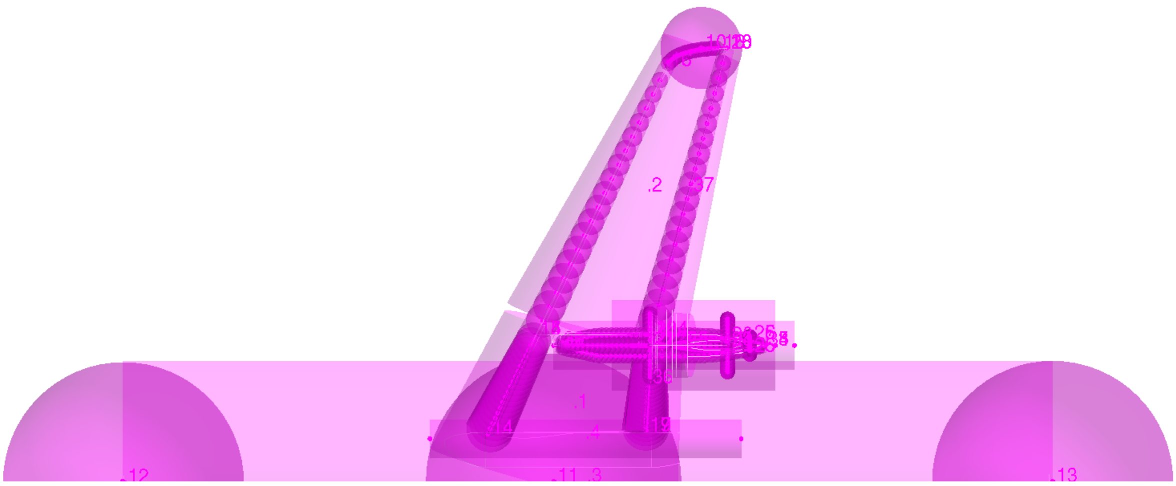

Fig. 2.2 *Geometric sources from CATIA in Centaur*

A representative grid is shown in Fig. 2.3. The total number of grid points is about 31 million including 43 semi-structured prism layers with a stretching ratio of 1.23 and an initial layer thickness of 0.004 mm ($Re = 21mio.$) resulting in a maximum stack height of 128 mm. The verification of an appropriate spatial resolution is provided in chapter 2.4.

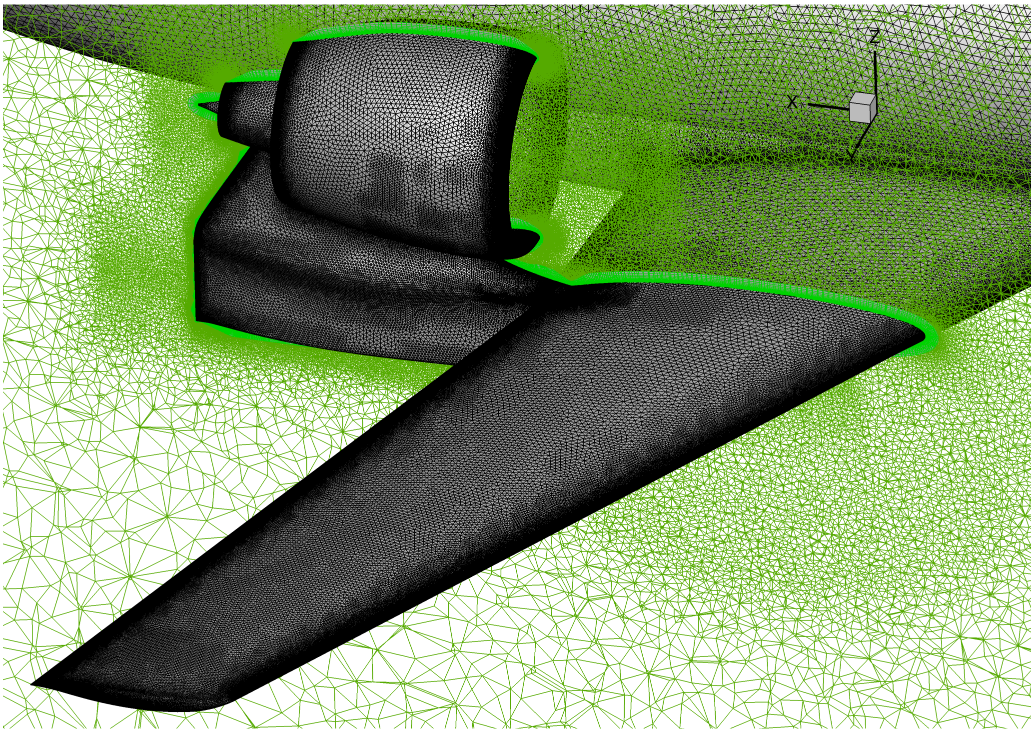

Fig. 2.3 *Representative visualization of Centaur grid with slice through prism (light green) and tetrahedral (dark green) cells*

2.3 Prediction of aerodynamic coefficients with AeroForce and ffd00

A central aspect of the aerodynamic analysis is the determination of aerodynamic coefficients respectively forces to predict the aerodynamic performance of an aircraft. Furthermore, the absolute values or variations of these coefficients can be associated with aerodynamic phenomena, like flow separations or the presence of strong shocks. Thus, the post-processing of numerical flow solutions with the aid of appropriate tools is crucial to obtain a comprehensive impression of aerodynamic characteristics. In case of numerical flow solutions, two different methods for the prediction of aerodynamic forces are available, surface-based and volume-based approaches. Both were applied by the utilization of AeroForce and ffd00 within the following investigations. The basic principals together with pros and cons will be discussed in the following sections.

2.3.1 Surface-based drag evaluation with AeroForce

AeroForce is a DLR in-house tool developed for the data post-processing of numerical flow solutions [28]. The evaluation is based on the surface solution and makes use of pressure and friction values to predict forces and aerodynamic coefficients by integrating over the surface distribution. Consequently, the drag breakdown is limited to the differentiation between friction and pressure drag. Nevertheless, the surface-based approach enables a fragmentation of the overall coefficients for individually defined geometric components, like fuselage, nacelle and wing. In addition, the segmentation of the surface provides the opportunity to book-keep thrust and drag in case of engine powered configurations. An algorithm, which detects the stagnation line at the nacelle highlight, enables the isolation of stream tubes and calculation of net-thrust as well as the accompanied pre-entry and post-exit thrust losses.

The essential AeroForce output includes a table list of force and moment coefficients in the body-fixed and aerodynamic coordinate system. The aerodynamic coefficients are calculated by taking into account the aircraft's incidence. Furthermore, the aerodynamic force coefficients, namely lift, drag and side force, plus the moment coefficients for yawing, rolling and pitching, are subdivided into friction and pressure components. Finally the engine related coefficients are listed. These imply on the one hand the intrinsic or gross thrust, which is calculated by integrating the momentum gain over the simulated engine boundary conditions. Note, the thrust vector is defined parallel to the engine axis and might differ from the aerodynamic x-axis. Consequently, the thrust component affects not only the force vector in direction of flight but may also impact other aerodynamic coefficients. From the airframe side of view, the momentum over the entire stream tube between $-\infty$ to ∞ is relevant to assess the balance between airframe drag and engine net thrust. The difference between net and gross thrust are losses, which can be divided into pre-entry and post-exit drag. To predict the flow state at $-\infty$ and ∞, the mass flow within the stream tube is assumed constant. Furthermore, an isentropic expansion is assumed. The pre-entry losses are equatable to the so-called ram drag, which is composed of the stream tube mass flow and the reference velocity. The post-exit drag depends on the expansion over the engine nozzle. In case, the static pressure at the nozzle exit p_e already reached p_∞, the post-exit losses are minimal. If $p_e > p_\infty$, a post-expansion takes place, resulting in notable post-exit losses. In addition, the friction and pressure losses on the inner engine surfaces, starting from the stagnation line at nacelle highlight over the engine inlet and outlet faces up the the nozzle trailing edge, are taken into account to finally determine the engine net thrust. Since the engine stream tube interacts with the outer surface of the airframe, the forces acting on the stream tube are considered as correction terms on the overall aerodynamic coefficients to receive finally the correct aerodynamic forces.

Concluding, AeroForce enables a detailed thrust-drag bookkeeping and a drag breakdown for specific geometric segments. Thus, the place of origin of aerodynamic forces can be predicted accurately. However, the forces are solely separated into friction and pressure components. Thus, the identification of the actual physical cause, evoking for example a drag rise, is not possible. Therefore, a volume-based evaluation is necessary to gain a more detailed insight.

2.3.2 Volume-based drag evaluation with ffd00

In the course of this investigation, drag evaluation was additionally performed with the aid of ffd00, which was provided by *The Office National d'Etudes et de Recherches Aérospatiales* (ONERA). ffd00 features the identical basis as ffd72 [29], but with a reduced range of functions. ffd00 combines a near-field and far-field drag evaluation. The surface-based approach provides a drag breakdown into friction and pressure drag, analogous to AeroForce. Whereas the volume-approach enables a drag breakdown into induced, viscous pressure and wave drag. Since the pressure drag, extracted from the surface, should equal the volume drag components, the total drag arise from the sum of friction, induced, viscous pressure and wave drag.

The interaction between solid surface and viscous flow results in viscous drag, which is composed of friction and viscous pressure drag. Friction drag is extracted from the surface, while the viscous pressure drag represents the pressure difference caused by examined body and the associated viscous displacement body in the near-field. Wave drag can be understood as an irreversible total pressure loss over a discontinuity in a compressible flow. Finally, the induced drag arises dependent on the lift generated by a finite wing. Thereby, two origins are involved. On the one hand, lift-induced drag occurs whenever a lifting body redirects the airflow, because the change of flow direction requires a force applied to the fluid. Besides the lifting force component perpendicular to the flow, the accompanied force component in flow direction is added to the overall drag. On the other hand the pressure equalization at the wing tips results in a wing tip vortex. These vortices induce an additional drag component, accordingly a pressure drag contribution.

The difference between near-field and far-field drag is called spurious drag and can be used as indicator for the mesh quality, whereby this component should be close to zero. The cause of spurious drag can be subdivided in three components. First, entropy production and total enthalpy changes in regions with high gradients induced by spurious vorticities normal to the velocity streamlines, e.g. around the leading edges, can cause spurious drag. This problem can be addressed by local grid refinements. Second, spurious drag can originate from an irreversible vortex diffusion and thus equals the streamwise loss of induced drag. Consequently, an accurate detection of vortices minimizes spurious drag. Third, the selection of insufficient far-field size can result in an additional spurious drag component.[43]

Summarizing, ffd00 enables a detailed analysis of the physical drag sources throughout this investigation. Thus the impact of an OWN and interaction with an aircraft can be understood and described in more detail.

2.4 Verification of simulation environment

The previous sections described the tools utilized for the numerical evaluation. However, a verification of the settings used for the subsequent investigations needs to be accomplished to ensure an appropriate approximation of the physical behavior. Therefore, a gird convergence study plus a turbulence model variation was carried out.

	Coarse	Mid	Fine
Total number of points	4,072,834	12,694,693	43,356,890
First wall-normal layer spacing	0.006mm	0.0042mm	0.0029mm
Stretching ratio	1.53	1.223	1.1
Max. no. of wall-normal layers	22	44	88

Tab. 2.1 *Properties of the three grid resolution levels*

The spatial discretization was investigated with the aid of three grid density levels. A guidance for a coherent method is given by [44], suggesting a scaling factor of $\sqrt[3]{3} = 1.4422$ for the grid refinement sources to obtain a consistent grid family. Additionally, the parameters controlling the prism layer are adapted for each grid refinement level taking account of y^+ values of about 1 and below. The prism layer height of each case features a different combination of wall-normal stretching ratio and number of layers to achieve a similar coverage of the near-surface volume. The properties of the three grid resolutions are given in Tab. 2.1.

Each grid refinement level was analyzed with the DLR TAU-code at a fixed angle of attack of $\alpha = 3°$ using the specified settings in Sec. 2.1. Furthermore, three different approaches for the turbulence approximation were tested:

- Spalart-Allmaras + Negative formulation
- Spalart-Allmaras + QCR correction
- Reynolds-Stress-Model (lnω-formulation)

The converged numerical results were evaluated with the aid of the surface-based drag prediction tool *AeroForce* providing the overall aerodynamic coefficients $C_L = L/(1/2\rho u_\infty^2 S)$ and $C_D = D/(1/2\rho u_\infty^2 S)$ and additionally a drag breakdown into friction ($C_{D,f}$) and pressure ($C_{D,p}$) drag. The coefficients are plotted over a grid index factor in Fig. 2.4 to Fig. 2.7. The factor is defined by the inverse of the total number of points to the power of 2/3. This illustration was chosen with respect to the Richardson Extrapolation [45], a method to evaluate higher order grid convergence by predicting the target value for an infinite number of grid points ($1/[Gridsize^{2/3}] \rightarrow 0$) [46]. Thereby, a required grid refinement can be identified, which is sufficiently representative for an infinitely fine grid.

Fig. 2.4 displays the progression of the total drag coefficient C_D for the three turbulence model settings with respect to the gridsize. In general, an increasing C_D-value for an increasing number of points can be observed. For the smallest number of points, SA-neg and RSM feature similar absolute values, about 5 drag counts (1 dcts $\widehat{=} 0.00001 C_D$) above the predicted drag coefficient by SA-QCR. With increasing number of points the predicted drag coefficients of RSM and SA-QCR are converging, whereas the SA-neg maintain at nearly constant offset with respect to the results of the SA-QCR turbulence modeling. Comparing the gradients over the grid refinement levels, an asymptotic behavior can be identified for all three approaches. For example, the difference for the SA-QCR between coarse and mid refinement totals 10 dcts., whereas a further refinement, which correlates with a tripling of grid points, results in a drag increase of 2 dcts.

The grid convergence study was performed for a constant angle of attack, thus the variation of the lift coefficient C_L is plotted in Fig. 2.5. Based on this figure, a parallel alignment of C_L for SA-neg and SA-QCR over the grid refinement levels can be observed. The difference is less than 1 lift count (1 lct $\widehat{=} 0.01 C_L$). The results for the RSM turbulence model feature more than 2 lcts difference on for the coarse grid with respect to the the SA turbulence models. This gap between the turbulence models decrease to less than 0.5 lcts between SA-QCR and RSM for the mid and fine grid. The progression of C_L features a similar behavior as discussed for C_D. The largest variation is traceable between the coarse and mid grid. A further refinement results in $\Delta C_L < 1$ lct. As a result it can be stated, that the mid grid refinement level is able to predict the overall aerodynamic

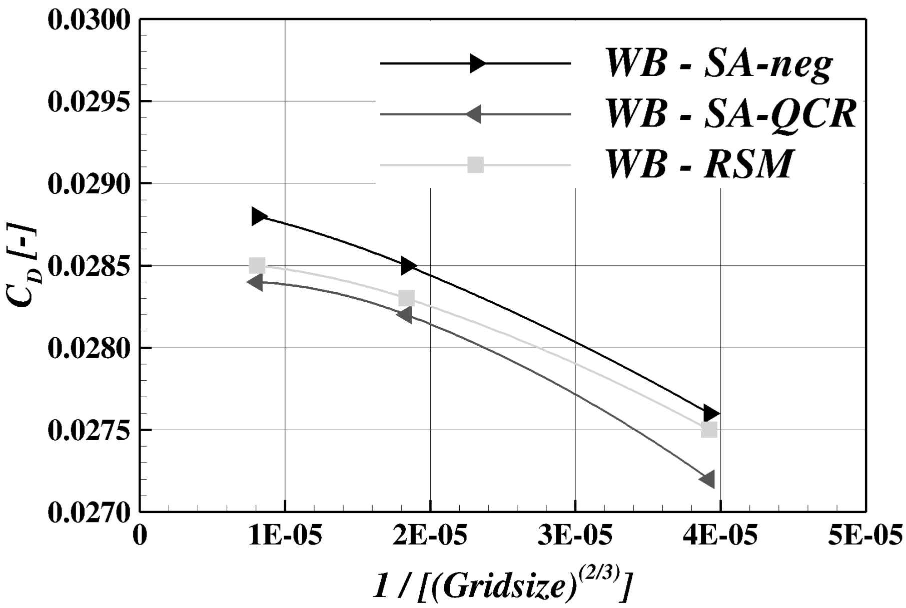

Fig. 2.4 *Total drag*

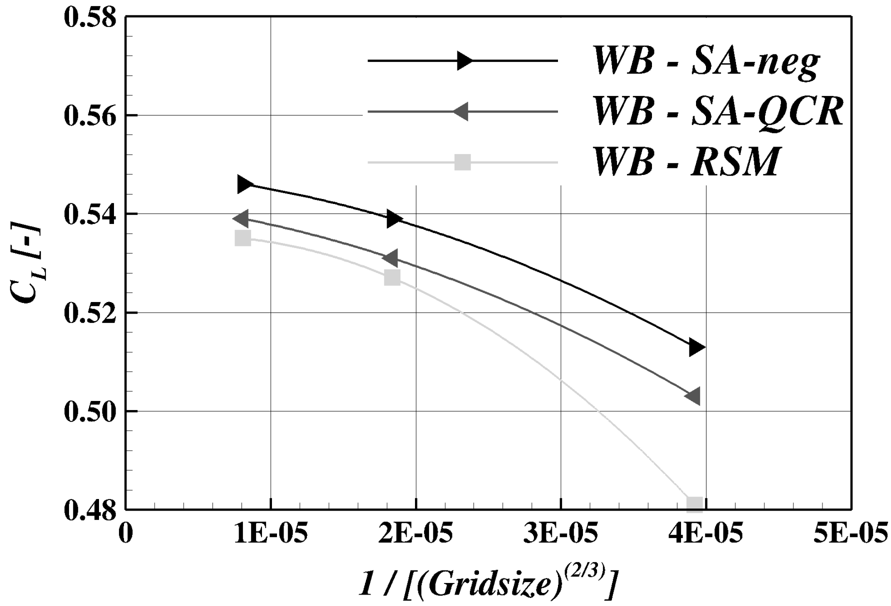

Fig. 2.5 *Total lift*

coefficients for this configuration with sufficient accuracy ($\Delta C_L < 1lct, \Delta C_D < 2dcts$). The required computational cost for the fine grid bear no proportion to the gain in information quality in comparison with the mid refinement level.

Subsequently, the choice of an suitable turbulence model will be discussed. Therefore, not only the total aerodynamic coefficients should be discussed but also the approximation of physical features. As starting point, the separation of C_D into pressure and viscous drag is presented in Fig. 2.6 and Fig. 2.7. For the pressure drag $C_{D,p}$ a good agreement between SA-QCR and RSM is given. The results for SA-neg are aligned parallel with a constant distance of +3 dcts. By contrast, the plot of friction drag $C_{D,f}$ exhibits an identical behavior for SA-neg and SA-QCR and the results for the RSM turbulence model are converging from a difference of 4 dcts. for the coarse grid towards the values

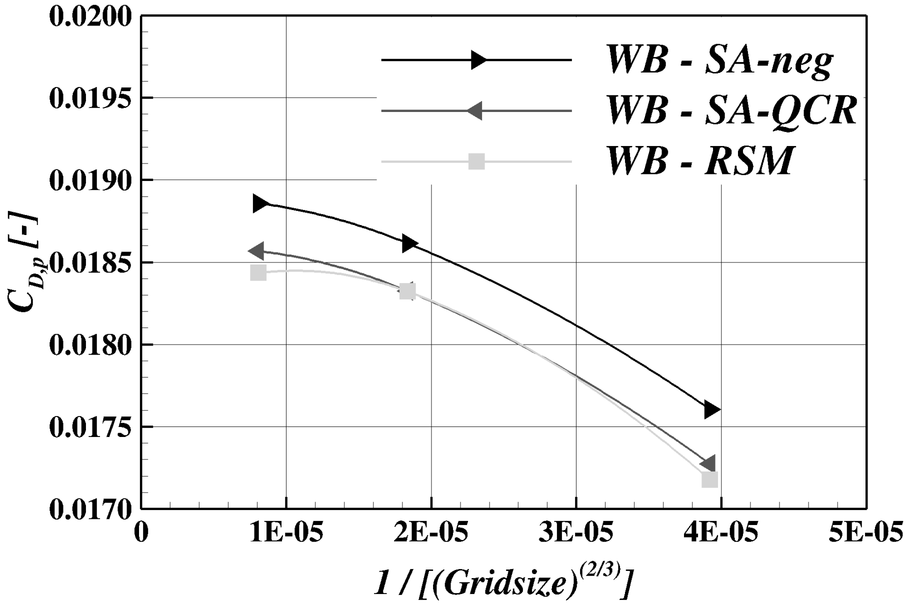

Fig. 2.6 *Pressure drag*

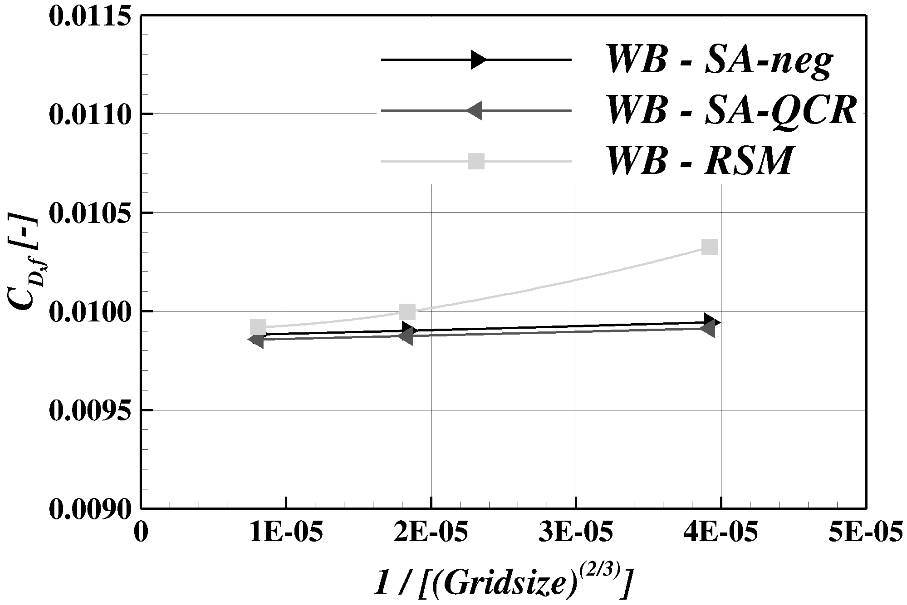

Fig. 2.7 *Friction drag*

of the SA models for the fine grid. Thus, RSM and SA-QCR provide similar results for the mid and fine grid but SA-neg overestimates both C_D and C_L. However, the values for SA-neg on the mid grid are comparable with the results for SA-QCR and RSM on the fine grid. Accordingly, the uncertainty between the turbulence model are within the order of uncertainty between the mid and fine grid.

Concurrently the computational time should be considered because of the proposed parameter variation to investigate two different OWN configurations. The computations on the mid grid revealed the fastest converged solution for SA-neg. In contrast RSM required twice the time and the implementation of SA-QCR in the TAU-code needed nearly triple the time. Consequently, a time efficient simulation is solely achievable with the SA-neg turbulence approach. Nevertheless, the investigations are not only targeting the discussion of drag values. Instead, physical phenomena should be investigated. Thus, the aerodynamic characteristics on the basis of the pressure $c_p = (p - p_\infty)/(p_0 - p_\infty)$ and friction $c_{f,x}$ coefficient is visualized in Fig. 2.8 and Fig. 2.9 for the mid grid level. In addition, a similar evaluation over the grid levels considering the SA-neg turbulence model can be found in appendix A.

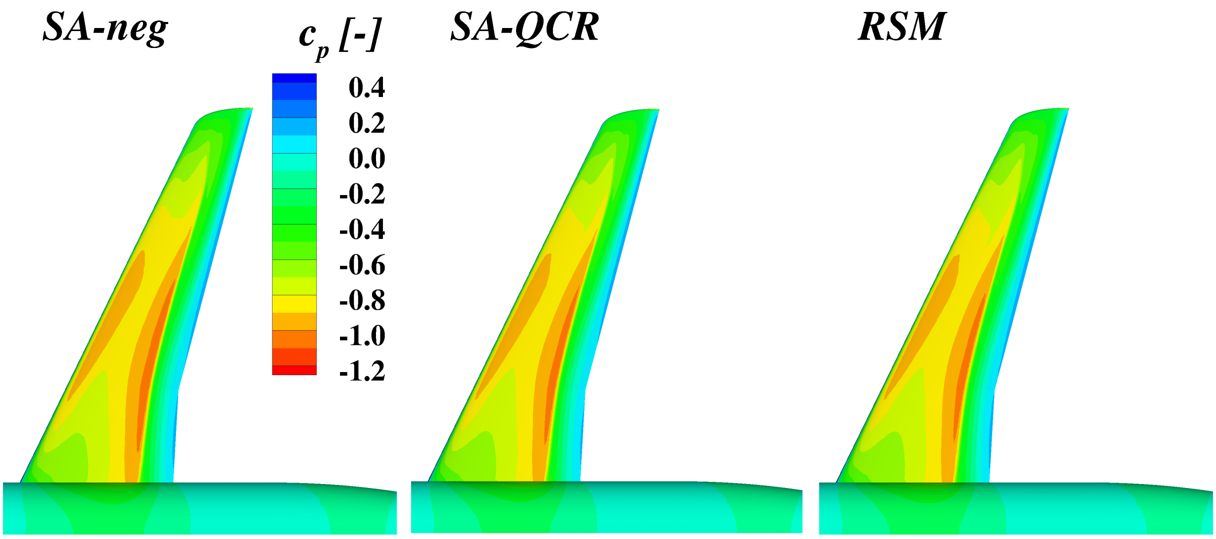

Fig. 2.8 *Top view on pressure distribution of REF3-WB for SA-neg, SA-QCR and RSM for the mid grid level*

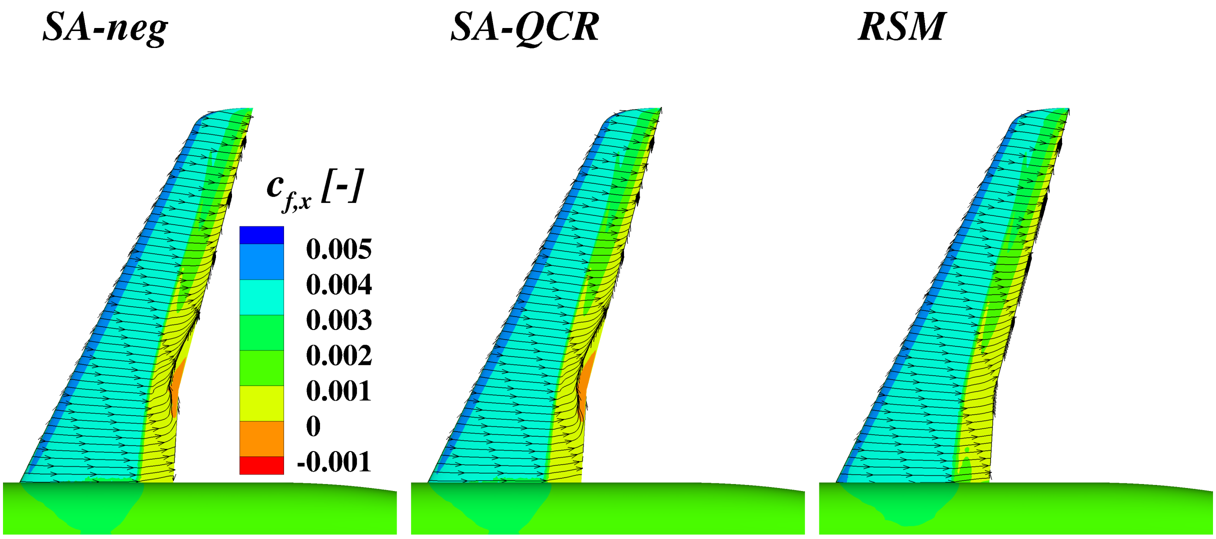

Fig. 2.9 *Top view on skin friction of REF3-WB for SA-neg, SA-QCR and RSM for the mid grid level*

A comparison of the pressure distribution in Fig. 2.8 along the wing upper surface reveals no distinct differences between the three turbulence models. However, the visualization of the skin friction coefficient $c_{f,x}$ in Fig. 2.9 exhibits a small flow separation for the two SA turbulence model settings around the kink at the wing trailing edge. For

RSM, the flow is fully attached. The tendency of the SA turbulence model to a premature flow separation in aerodynamically critical areas is known from various investigations [47]. In the past, a great number of validation cases proved an improved approximation of physical phenomena with the aid of the RSM turbulence model in comparison with SA. However, the results for both SA models with the small flow separation reveal no distinct effect on the pressure drag and the pressure distribution. Consequently, the difference between the three models is still minor.

Summarizing, three different approaches for the turbulence modeling on three different grid refinement levels were evaluated. Initially, the mid grid resolution was classified as sufficient to obtain meaningful information from the numerical calculations. A comparison of the results with the aid of SA-neg, SA-QCR and RSM revealed small differences. The pressure and viscous drag values for SA-QCR and RSM were nearly identical. However, the computational time for RSM and SA-QCR differ from SA-neg by at least a factor of 2. The visualization of pressure and skin friction coefficients revealed a small flow separation for the two SA approaches. In comparison, the RSM result features a fully attached flow. Anyway, there exists one additional limitation due to the utilization of the drag prediction tool ffd00. At this point in time, ffd00 is not able to post-process the results obtained with the RSM turbulence model. Consequently a decision had to be taken between an improved turbulence model and the advantage of the far-field drag breakdown by ffd00 to gather more information about physical drag components. Thus, it has been decided to run all simulations with the Spalart-Allmaras turbulence model extended by the negative formulation. The SA-QCR turbulence model offered no accuracy advantage but would be more time consuming as well as the RSM model. At the same time, RSM and SA-neg converge to comparable values within the grid convergence study, while the correct description of the flow separation cannot be decided without experimental validation data. Thus the SA-neg turbulence model offers the best compromise between computing time, robustness and applicability for the investigation of complex engine installation effects.

2.5 Surrogate-based investigations with the optimization tool POT

The objective of this work is the investigation of a range of geometrical parameters controlling for example the engine's position. Therefore, the optimization environment *Powerful Optimization Tool with Surrogate Modelling* (POT) is utilized. POT is a DLR in-house tool, compiled by Wilke [30]. With the aid of this optimization tool a predefined parameter space can be investigated by a design of experiments (DoE) providing an initial exploration of the parameter range and parameter sensitivity. The subsequent optimization enables the detection of an optimal parameter combination, while during the process the surrogate model will be improved to guarantee an optimal approximation of the physical characteristics by the surrogate model. Finally, the impact of individual parameters and dependencies can be extracted from the surrogate model. Thus, not only a beneficial engine position or wing shape can be identified, but moreover a physical explanation can be provided about the disadvantages of other parameter combinations together with their impact on the objective function. In the following, POT will be outlined and basic principles used for the present investigations are highlighted.

Various optimization tasks without any bond to a certain CFD solver, mesh generator or computer aided design (CAD) software can be solved with the aid of POT. For this purpose, a wide range of algorithms and techniques for direct, single and variable-fidelity surrogate-based optimization is implemented, while the fidelity refers to the accuracy of the applied simulation method. The present work utilized a single fidelity surrogate-based optimization. The optimization procedure can be subdivided into three steps:

- design of experiments (DoE)
- surrogate models
- optimization strategy

In the beginning, a DoE needs to be accomplished to explore the predefined parameter space by a certain number of samples. Based on the DoE sampling a surrogate is created, which represents a first approximation of the actual properties and sensitivities within the multi-dimensional parameter space with respect to the objective function. POT offers a range of algorithms to select an initial sampling to achieve a homogeneous distribution within the parameter space by using a minimal number of sample points. The first data set is crucial with respect to the initial approximation by a surrogate model because the number of subsequent iterations depends on the quality of the initial surrogate model. Otherwise, a large number of additional iterations are necessary for the improvement of the surrogate model until a minimal acceptable uncertainty and prediction error is achieved. For the present investigations, an advanced Latin Hypercube, the Central Voroni Tessellation (CVT) [48] was chosen for the selection of DoE sample points.

The surrogate model is generated based on the simulation data of the individuals of the DoE with the aid of a kriging method [49]. Kriging combines a trend function and radial basis function to obtain a sensible approximation of the objective function depending on the sampling. In addition, several settings, like regression model or treatment of numerical noise, can be adapted to achieve a robust, efficient, and accurate approximation by the surrogate model describing the actual physical behavior. Based on the surrogate model, the optimization is started targeting both, a global optimum but also an optimal representation of the parameter space with the aid of an adaptive sampling strategy. A hybrid optimization approach is utilized, composed of a Differential Evolutionary (DE) algorithm and a non-gradient based simplex pattern search method. By means of this procedure, global regions of interest will be identified by the DE, whereas the pattern search determines the local optimum in these regions more accurate.

3 Aircraft configurations

This work considers two aircraft configurations, selected from the work performed by the Collaborative Research Centre (CRC) 880. In total five concepts were designed within this project [50]. At first, two conventional configurations were designed, representing state of the art technologies, whereat one is equipped with under-the-wing mounted turbo-fan engines and the other with turbo-prop engines. Thereon, three configurations with potential technology assumptions were created: one turbo-prop configuration and two configurations with ultra-high bypass, over-the-wing mounted turbo-fan engines. The preliminary aircraft designs for all five configurations were obtained by the application of the simulation tool PrADO (Preliminary Aircraft Design and Optimization) [51]. The present work focuses on both turbo-fan aircraft with over-wing nacelles (OWN), positioned at about one-third of wing span above the wing trailing edge. The most significant difference between these configurations is the wing planform. The reference aircraft 3 (REF3) is characterized by a double-trapezoid backward swept wing. By contrast, the reference configuration 4 (REF4) features a single-trapezoid forward swept wing. Because both aircraft were driven by the overall aircraft design (OAD) all aspects of an complete design were taken into account. Besides the classical key performance indicators, like mission, aerodynamic performance, weight, and block fuel, selected preliminary assumptions were investigated with higher fidelity methods on the basis of REF3 and REF4. Exemplary, the research topics acoustic [52], active flow control [53] and structure design [54] was investigated in more detail and results were fed back to the OAD. As a consequence, the underlying reference configurations represent a complex, multi-disciplinary design. As part of these investigations, the present work focuses on the aerodynamic installation of UHBR engines above the wing trailing edge. Previous studies by Lockheed Martin, outlined in chapter 1.1, had shown that the interference between wing and OWN is crucial for an efficient design and depends on the engine position, wing planform and shape. However, basic effects describing the interference between a transonic wing and ultra-high bypass OWN were not described yet. Therefore, this study targets the investigation of general installation effects on two representative configurations.

The following sections will elaborate the aircraft configurations REF3 and REF4 from the perspective of the OAD. Furthermore, general aerodynamic features of a forward and backward swept configuration will be presented on the basis of the wing-body-configuration (WB). In general, both aircraft were designed with respect to the same top level aircraft requirements (TLAR)[50]. These demand a mission range of 2000 km with maximum payload (100 PAX with baggage, 2.2t freight). Without freight but maximum passenger number, a range of 2800km should be covered. The cruise velocity is defined at Mach number M = 0.78 at a flight level of 37,000 ft (FL370). Additionally, a short take-off and landing (STOL) capability was demanded to enable the operation with a maximum runway length of 900m.

3.1 Reference aircraft configuration 3

The reference aircraft configuration REF3 is equipped with a double-trapezoidal backward swept wing, designed for a transport mission of 100 PAX over a range of 2000 km at $M = 0.78$. This section provides an insight into the overall aircraft design of REF3 and general aerodynamic characteristics of backward swept wings are discussed on the basis of this configuration.

3.1.1 Overall aircraft design

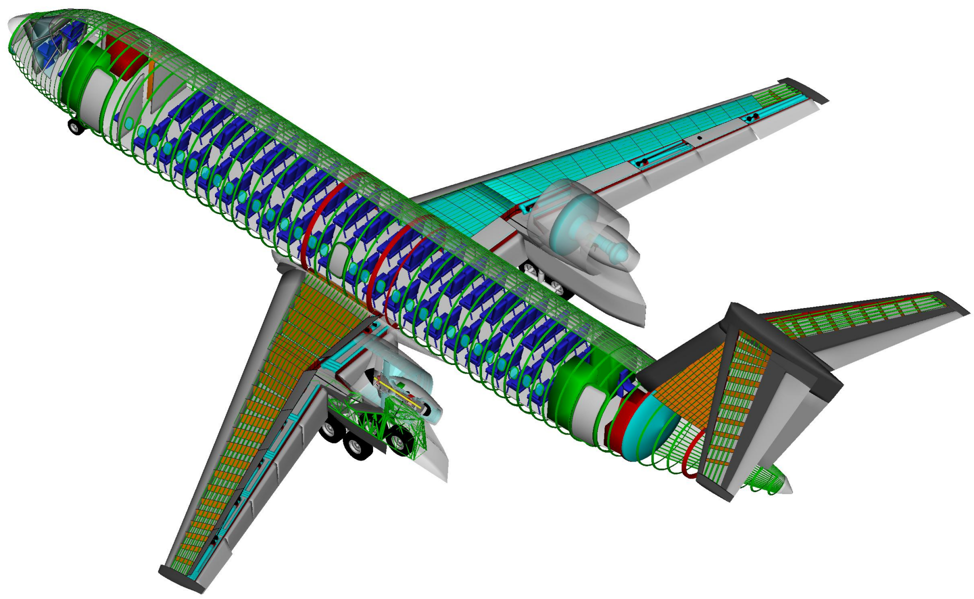

Fig. 3.1 *Sketch of REF3 based on OAD data [2]*

The reference configuration 3 (REF3), illustrated in Fig. 3.1, is designed for a transport mission of 12000 kg payload (100 passengers with baggage and 2.2 t freight) over 2000 km. The cruise Mach number is defined by $M = 0.78$. This necessitates a swept wing with a wing leading edge sweep of 26° (50% chord sweep = 15.2°(inboard) / 20.6°(outboard)). Moreover, turbo-fan engines are required to operate efficiently at $M = 0.78$. The engines are ultra-high bypass ratio (UHBR) engines with an bypass ratio BPR of 17. One feature of the REF3 is the engine position. Instead of an engine installation below the wing, the UHBR engines with a diameter of 2299 mm (fan diameter = 2025 mm) are located over the wing mounted at the wing trailing edge. As a consequence the empennage is a T-tail to eliminate an aerodynamic interaction between horizontal tail plain and the engine jet for cruise conditions such that the necessary handling qualities are ensured. A general view of the principle dimensions is given in Fig. 3.2. The wing reference area totals 99 m^2 with an aspect ratio of 8.35. The wing shape is based on the DLR-F15 airfoil, which was extracted from the FNG wing [55]. The high-lift system is characterized by a combination of various new technologies. The leading edge is equipped with a smart morphing droop nose to increase the maximum angle of attack during take-off and landing. Along the trailing edge, five flaps and one aileron are installed including an active flow control system to increase the maximum lift by blowing air over the trailing edge devices to further increase the high-lift performance [56]. Because of this high-lift system, the REF3 features STOL capabilities allowing the aircraft to operate on short runways of about 900 m with a maximum take-off weight (MTOW) of 46.2 t. The investigation of the high-lift performance is not part of this work. More information can be found in [50] and [53]. The arrangement of the landing gear is unusual for a turbo-fan powered aircraft. It is located below the engines in an enlarged pylon fairing, which is dimensioned to house the retracted undercarriage. This design decision was necessary because of the aircraft's mass distribution and the resulting risk of a tail strike. The center of gravity is shifted significantly rearward due to the engine's location behind the wing, which prevented, in combination with the necessary space for the electrical compressors, the use of a body mounted landing gear.

The expected advantages of the engine position is driven by various aspects. First, the shielding of the wing regarding engine fan noise leads to a reduction of perceived noise on the ground. Additionally, weight savings can be achieved due to the short landing gear and the risk of foreign object damage during ground operation is reduced for the engine. Finally, beneficial aerodynamic installations effects between wing and OWN can be exploited to reduce the overall drag of the aircraft in cruise flight.

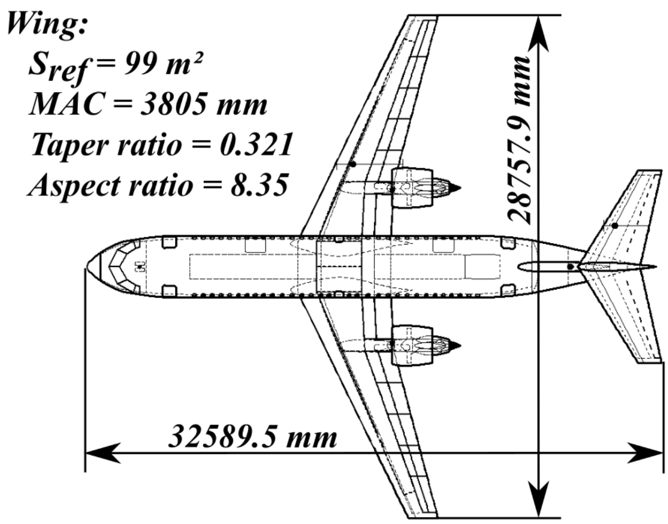

Fig. 3.2 *Principle dimesnions of REF3 [2]*

This work focus on the cruise configuration. The design flight condition is defined at an altitude of 11277 m at $M = 0.78$. The intended aerodynamic performance by the OAD requires a lift-to-drag ratio of 13.6 at a lift coefficient $C_L = 0.469$.

3.1.2 Aerodynamic characteristic of BSW without OWN

The following section focuses on the general aerodynamic features of a backward swept wing, exemplary presented by means of the REF3 WB configuration. Therefore, the wing-body configuration was analyzed with the aid of numerical simulations to assess the characteristics of the BSW without the impact of an engine. The evaluation is carried out at M=0.78 and target lift of $C_L = 0.469$, resulting in an incidence angle of $\alpha = 2.43°$.

The magnitude of wing sweep is driven by the design cruise speed. Thereby, the wing sweep at the chordwise shock position is decisive to minimize the wave drag, originating from compression losses at the closing face of the local area of supersonic flow. Furthermore is known, that an elliptical spanwise lift distribution is beneficial with respect to lift induced drag. This can be achieved by either an elliptical wing planform, which implies a complex and costly manufacturing, or the application of a tapered planform and spanwise twist distribution. Concurrently, the effectiveness of trailing edge high-lift devices reduces with increasing trailing edge sweep angle. As a consequence, the wing planform of most transonic civil aircraft is characterized by a tapered, backward swept wing. In case of REF3, the leading edge sweep totals 26°. Resulting from the double trapezoidal wing planform, the sweep angle at 50% chord is 15.2° for the inner and 20.6° for the outer wing section. Transonic aircraft operating at similar conditions are equipped with twist angles changing from root to tip by up to −5° [57]. The preliminary design for REF3 specified an initial spanwise twist distribution at wing root and kink of 0°, and −6.94° at the tip. The reason behind this unusual spanwise twist distribution is the design objective of REF3 focusing on low speed performance with active blown flaps, which necessitates large negative twist angles to prevent tip stall [57].

An impression of the pressure coefficient c_p on upper and lower wing surface is given in Fig. 3.3. The surface coloring represents the pressure coefficient supported by dashed lines marking the arrangement of the isobars. In addition, the critical pressure coefficient $c_{p,crit}$, indicating the transition between super- and subsonic regions, is highlighted by a red solid line. The upper part of Fig. 3.3 provides a top view on the WB configuration, wheres the lower surface is displayed on the bottom.

On the wing upper surface, the blue area represents the supersonic low pressure region covering almost three quarter chord length in average. The shock position can be identified by both, the color transition from blue to green and the red solid line.

The mid wing section is characterized by an almost constant pressure level along the region of supersonic flow. Downstream of the shock, the pressure rises. The isobars are aligned at constant percentage chord depth between leading and trailing edge. This preferred pressure distribution is representative for a transonic wing based on a supercritical airfoil featuring a rooftop characteristic [58].

Nevertheless, a deviation from this preferred c_p-distribution can be found at wing root and tip, a well known and described phenomena of finite swept wing [59]. On the inner wing section, the formation of a leading edge pressure peak is observable. This disturbance is caused by the intersection of belly and wing leading edge. A smooth pressure decrease in flow direction up to the shock can be observed. Concurrently, the isobars deviate from the preferred alignment and are shifted downstream.

At the wing tip, the pressure distribution is disturbed by the pressure equalization between upper and lower surface. As a result, the area for $M > 1$ ranges not up to the

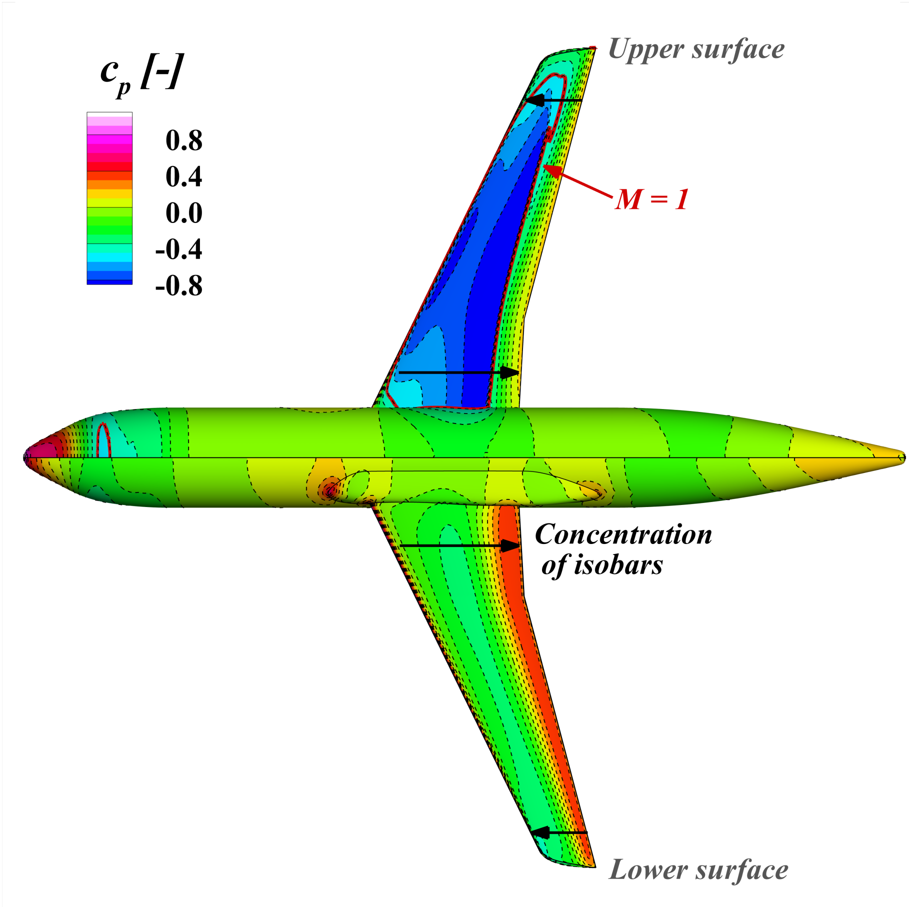

Fig. 3.3 *Visualization of surface pressure coefficient on REF3 WB configuration*

wing tip and the leading edge suction peak is less pronounced. By observation of the dashed lines, an upstream shift of the isobars can be detected. This deviation from the preferred isobar alignment is reversed to the observations at the wing root. The particular shift of the isobars is indicated by black arrows.

This effect is also traceable on the wing lower surface on the bottom of Fig. 3.3. A large part of the lower surface is colored in green, indicating pressure coefficients between $-0.4 < c_p < 0$. At the wing trailing edge, a distinct red strip can be recognized, which implies high pressure values around c_p=0.4. This intended feature is called rear loading and enables a lift gain due to an increased pressure difference between upper and lower surface.

In addition, Fig. 3.4 visualizes streaklines on the REF3 wing. The streaklines are based on the dimensionless surface shear stress vector. The surface coloring displays the skin-friction coefficient in x-direction $c_{f,x}$. This coefficient provides information about the interaction between boundary layer flow and surface. This can be used to identify areas, where the flow is close to separation or in case of $c_{f,x} < 0$ most likely already separated. For orientation, the area of local supersonic flow is again outlined by the red solid line. First, the streaklines on upper and lower side are not orientated in line of flight but lean outboard following the leading edge sweep. After a few percent chord length, the streaklines are reorientation inboard through a flow acceleration perpendicular to the wing leading edge following the main curvature. This effect decreases with increasing distance covered. At the wing trailing edge, the streaklines are pointing again outboard,

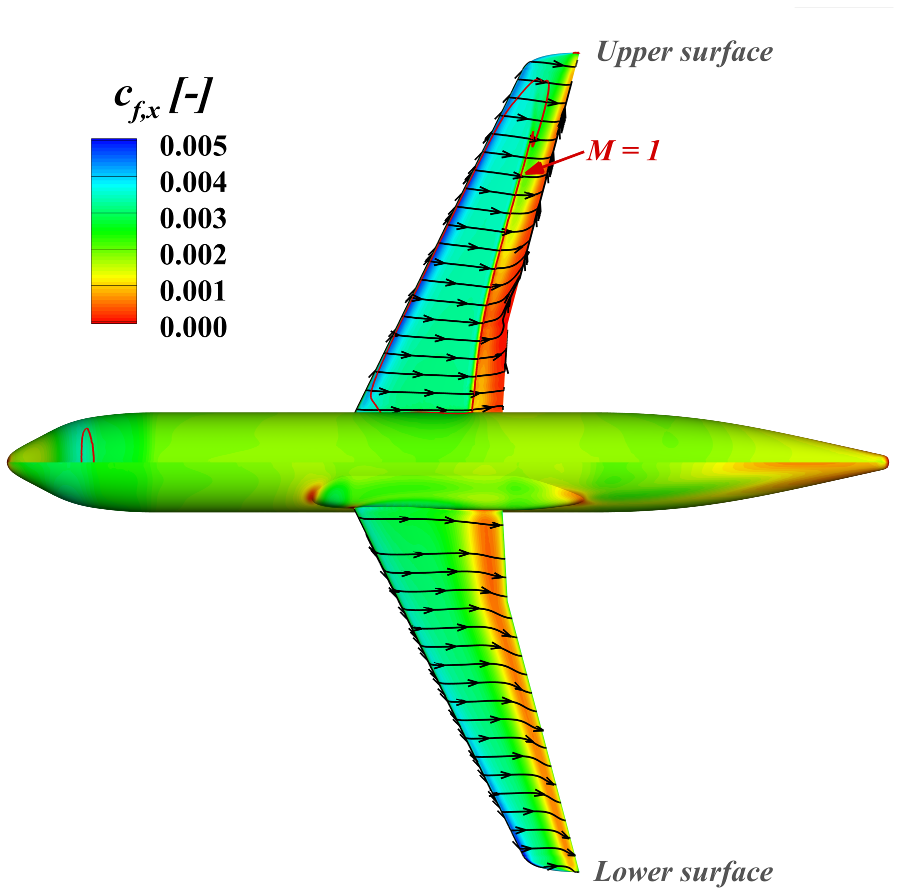

Fig. 3.4 *Visualization of skin friction coefficient and streaklines on REF3 WB configuration*

revealing a crossflow towards the wing tip evoked by the backward sweep. This trend is amplified by a decreasing vector component in x-direction. The drop in $c_{f,x}$ occurs on the upper wing surface downstream of the shock and on the lower wing in the region of the rear loading. The disturbance induced by the transition from super- to subsonic flow results in a distinct weakening of the boundary layer flow. However, reverse flow and thus a flow separation could not be detected for the WB configuration in cruise flight conditions. Consequently, pressure information is propagating on a backward swept wing in particular from inboard to outboard.

Summarizing, the REF3 WB-configuration represents the design of a common transonic wing, which is characterized by a supercritical airfoil and a backward swept, tapered wing. Solely the values of the wing twist distribution deviates from the usual known ranges due to the challenging high-lift requirements. Known features of a finite swept wing could be detected at wing root and tip. The WB-configuration reveals no flow separations at the defined cruise flight conditions. Consequently, the REF3 WB-configuration is suited to investigate the integration of an over-wing-nacelle.

3.2 Reference aircraft configuration 4

The reference aircraft configuration REF4 is equipped with a single-trapezoidal forward swept wing, designed for a transport mission of 100 PAX over a range of 2000 km at $M = 0.78$. This section provides an insight into the overall aircraft design of REF4 and general aerodynamic characteristics of forward swept wings are discussed on the basis of this configuration.

3.2.1 Overall aircraft design

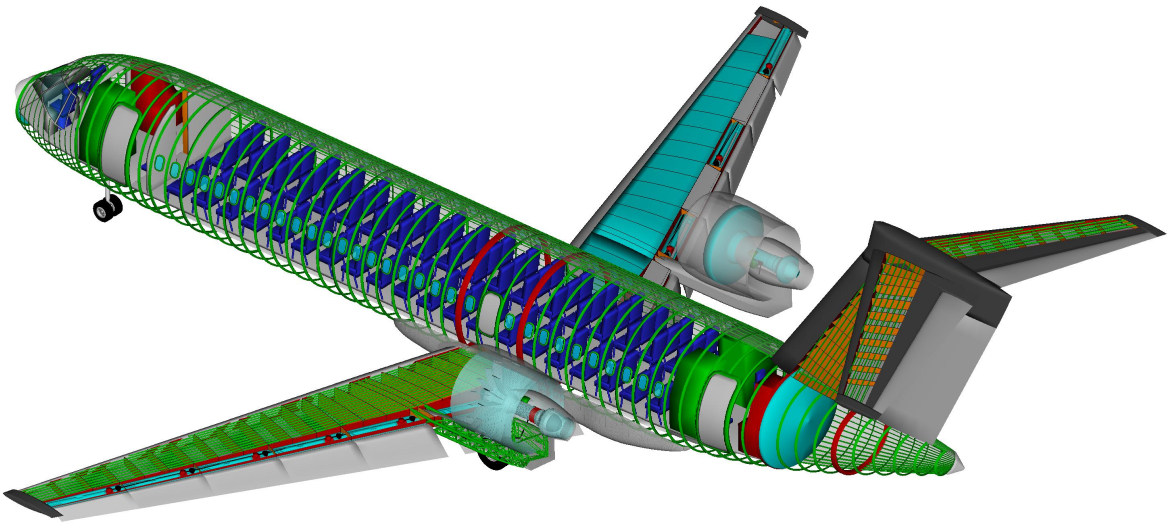

Fig. 3.5 *Sketch of REF4 based on OAD data [3]*

The reference configuration 4 (REF4) is illustrated in Fig. 3.5. Most aircraft data are identical to REF3. The wing reference area totals also 99 m^2 with an aspect ratio 8.35. The wing shape is based on the DLR-F15 airfoil [60]. The required transport mission of 100 passengers over 2000 km is identical to REF3. Analogous to REF3, the high-lift system is characterized by a combination of smart morphing droop nose and an active flow control system at the trailing edge, composed of five flaps and one aileron. Because of this high-lift system, the REF4 features STOL capabilities allowing the aircraft to operate on short runways of about 900m with a maximum take-off weight (MTOW) of 45.5 t.

The most significant design change is the wing planform. The REF4 features a single trapezoidal forward swept wing with a 50%-chord sweep angle of 20.7° to operate at $M = 0.78$, resulting in a leading edge sweep angle of 14°. The utilized UHBR engines with BPR of 17 are identical for both configurations and also located at the wing trailing edge above the wing. The modified wing planform results in a slightly decreased wing span of 28.75 m and mean aerodynamic chord MAC = 3.77 m for a constant aerodynamic reference area S_{ref}=99 m^2. The general difference between REF4 and REF3 is illustrated in Fig. 3.6.

Based on Fig. 3.6, a significant rearward shift of the wing mounting can be identified. The difference totals 3.1 m. As a consequence, the landing gear can be placed at the wing-belly junction and retracted into the fuselage, which in turn effects the engine pylon. The wetted pylon area is reduced by a factor of 3 (Δwetted area = 13.05 m^2) and the mass per pylon is decreasing by 236 kg. The fuselage weight increases by about 530 kg due to the skin thickening in front of the wing connection and the necessary pressure bulkheads in the main wheel bay[3].

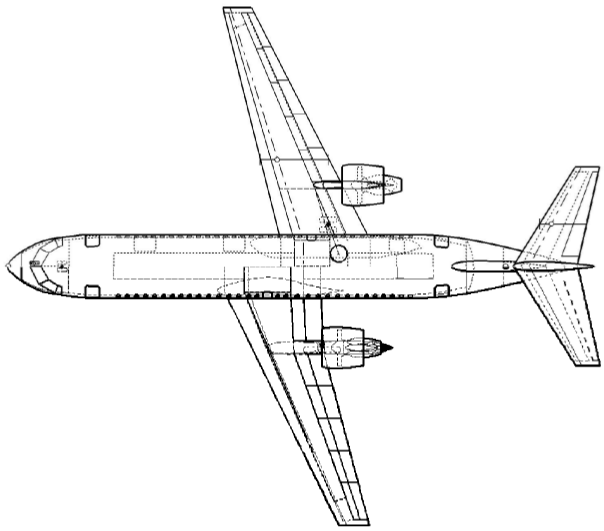

Fig. 3.6 *Compariosn of REF4 and REF3 [2] [3]*

The REF4 operates in cruise flight at an altitude of 11277m at M = 0.78. The intended aerodynamic performance is defined by a lift-to-drag ratio of 13.6 for a lift coefficient C_L = 0.479.

3.2.2 Aerodynamic characteristic of FSW without OWN

Subsequent, the general aerodynamic features of a forward swept wing will be discussed based on the REF4 WB configuration. Thereby, characteristics of a FSW in absence of an engine can be analyzed. The evaluation is accomplished at M = 0.78 and target lift C_L = 0.479, resulting in an angle of attack α of 1.485°.

Accounting for the design cruise speed, the wing planform requires an appropriate sweep angle. Analogous to REF3, the wing sweep at 50% chord is set to 20.7°. In combination with the tapered wing, the sweep angle at the leading edge (14°) is smaller then for the trailing edge (27°). In addition, the forward swept wing requires a spanwise twist distribution, which features the largest twist angle of 2.82° at the wing tip and 0° at the wing root. This twist variation complies with the LamAiR design [24]. The beneficial feature of lower twist angles to obtain similar spanwise lift distributions was also stated by Hepperle [61], while comparing backward and forward swept configurations. Note, this wing twist is contrariwise to the backward swept wing. In addition, forward swept configurations are characterized by an inboard wing loading. This is advantageous for the wing structure. However, the inboard loading in combination with an increasing angle of attack might evoke wing stalls in the root section instead of the tip region. This might be beneficial with respect to maneuverability due to usable ailerons but causes a detrimental pitch-up moment.

Fig. 3.7 illustrates the surface pressure distribution on the WB-configuration of REF4. The surface coloring represents the pressure coefficient supported by dashed lines marking the arrangement of the isobars. In addition, the critical pressure coefficient $c_{p,crit}$

$$c_{p,crit} = \frac{1}{1/2\kappa M_\infty^2}\left[\left(\frac{1+1/2(\kappa-1)M_\infty^2}{1/2(\kappa+1)}\right)^{\kappa/\kappa-1} - 1\right] \tag{3.1}$$

is highlighted by a red solid line. This coefficient indicates a local Mach number of 1, thus the transition between super- and subsonic regions. The upper part of Fig. 3.7 provides a top view on the WB configuration, wheres the lower surface is displayed on the bottom.

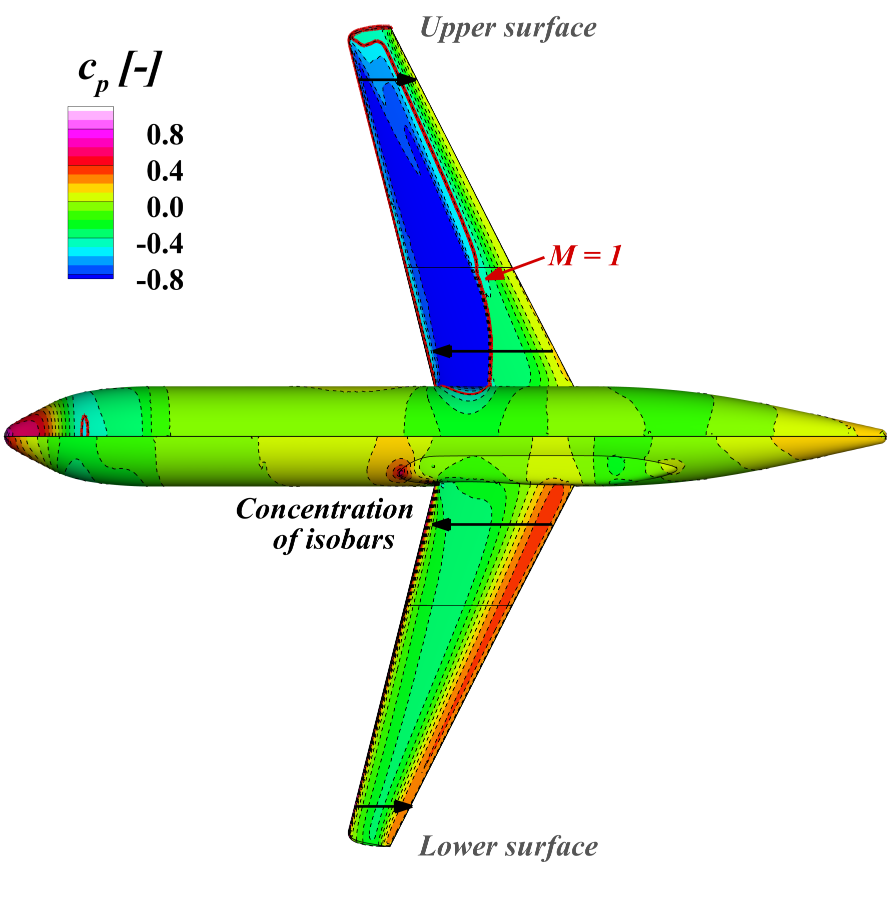

Fig. 3.7 *Visualization of surface pressure coefficient on REF4 WB configuration*

The surface pressure distribution on the upper wing reveals a uniform blue area in the mid wing section, representing a large low pressure region over the first 65% of chord in average. This feature is caused by utilization of the same supercritical airfoil as for REF3. However, the red line, indicating the area of supersonic flow is not directly located downstream of the dark blue area instead in a region of gradual color change in chordwise direction, which is indicating a smooth transition from super- a subsonic flow for this particular flow condition. The isobars on the mid wing section are aligned at constant relative chord depth between leading and trailing edge.

The wing ends are again characterized by the known three-dimensional phenomena of a finite swept wing [59]. In the wing root section, a narrowing of the low pressure region can be observed. Concurrently, the red line is located directly downstream of the shock, which indicates a strong pressure gradient. In general the isobars are shifted upstream at the wing belly junction. This is a known feature of forward swept wings caused by the intersection between belly and wing. Several studies at DLR [24] [25] [61] referred to this issue. Moreover, it is known from [59], that an adaptation of the airfoil thickness can influence this effect. [24] has applied this knowledge to a forward swept configuration while maintaining the negative pressure gradient within the region of supersonic flow by shifting the maximum airfoil thickness aft. A drawback was noted at higher Mach numbers. An increasing wave drag induced by a strengthening of the inboard shock resulted in performance losses. Note, the isobar displacement at wing root of the forward swept wing is contrary to the trend observed on the backward swept wing.

A similar statement can be made with respect to the wing tip. There, a concentration of the isobars towards the trailing edge are observable, contrary to the observations on the BSW. Additionally, a limited extend of the low pressure region up to the wing tip can be noted due to the pressure compensation.

The lower wing surface on the bottom of Fig. 3.7 displays again the observed isobar displacement at root and tip equivalent to the upper wing surface of REF4. Moreover, the high c_p-values, indicated by the red surface coloring, expose the rear loading characteristic of the selected supercritical airfoil.

Finally, the skin friction coefficient $c_{f,x}$ is visualized for REF4 in Fig. 3.8. Again, the streaklines are based on the surface shear stress vector. The surface coloring displays the skin-friction coefficient in x-direction $c_{f,x}$. Like for REF3 this coefficient provides information about the interaction between boundary layer flow and surface. This can be used to identify areas, where the flow is close to separation or in case of $c_{f,x} < 0$ already separated. For orientation, the area of local supersonic flow is outlined by the red solid line. As seen for REF3, the streaklines are not orientated in line of flight. After the initial disturbance along the leading edge, the streaklines lean outboard caused by the flow acceleration along the main curvature orientated perpendicular to the leading edge. At wing trailing edge, the streaklines are pointing inboard, revealing a crossflow towards the wing root due to the increasing local sweep angle caused by the forward swept planform. This trend is amplified by a decreasing velocity vector component in x-direction. On the upper wing of REF4, two red areas are pointing out $c_{f,x}$-values close to zero. One the one hand, a small strip can be found on the inner wing section, directly downstream of the shock. There, the c_p-distribution in Fig. 3.7 indicated a strong pressure shock, which causes a local pressure disturbance associated by an momentum loss in the near-wall flow and thus a weakening of the boundary layer. The benefit of a smooth pressure gradient from super- to subsonic can be noted on the mid and outer wing, where almost no alteration in $c_{f,x}$ can be detected around the shock position. On the other hand, a spanwise spreading red area along the trailing edge is obvious. There, the inboard facing crossflow component dominates the local

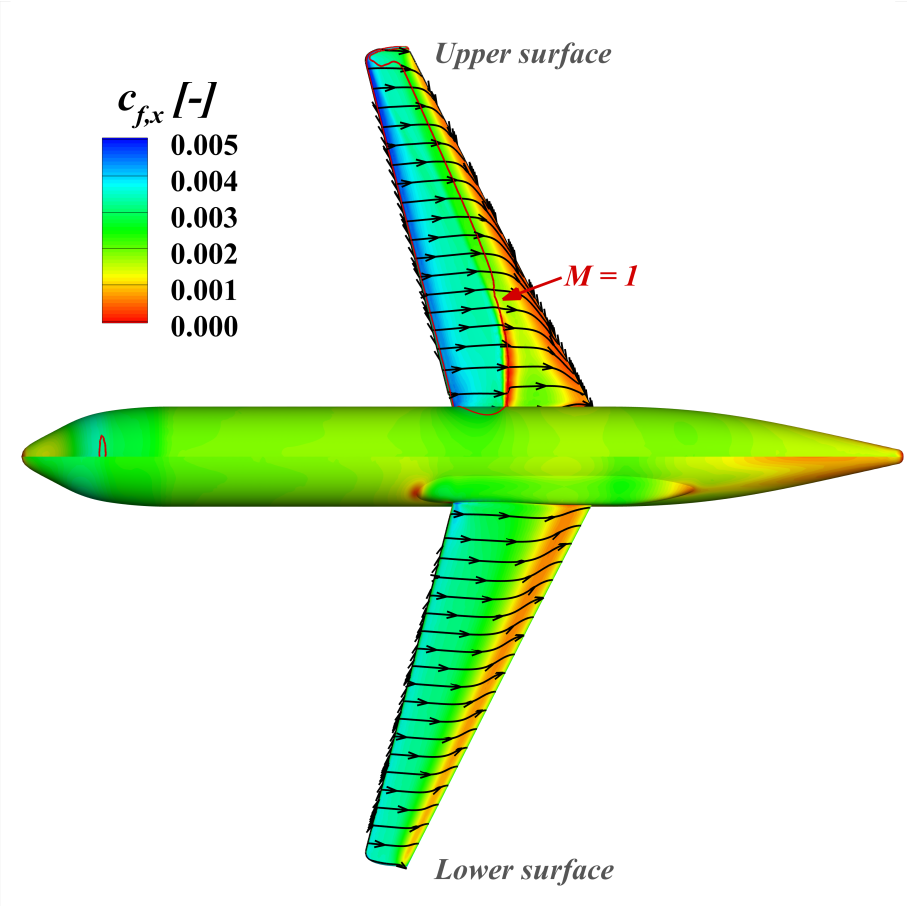

Fig. 3.8 *Visualization of skin friction coefficient and streaklines on REF4 WB configuration*

skin friction vector. Generally, reverse flow and thus a flow separation could not be detected for the WB configuration in cruise flight conditions. Consequently, pressure information propagating on a forward swept wing in particular from wing tip to root.

Summarizing, the REF4 WB-configuration features fundamental and representative characteristics of a forward swept wing operating at transonic speed. The configuration is characterized by a supercritical airfoil in combination with a tapered wing. Known features of a finite forward swept wing could be detected at wing root and tip. The WB-configuration reveals no flow separations at the defined cruise flight conditions. Therefore, this configuration represents a reasonable design of a FSW, which is useful for the investigation of over-wing-nacelle integration.

4 Aerodynamic impact of an OWN on a backward swept wing

Following on the general aerodynamic features of a wing-body configuration including a backward swept wing, this chapter will deal with the aerodynamic installation effects caused by an OWN. Therefore, the fundamental phenomena for an arbitrary over-wing engine position is investigated on the basis of the REF3 in combination with an UHBR engine. To build up a comprehensive understanding of the OWN installation effects, the engine thrust setting and engine position are altered and investigated regarding their impact on pressure distributions, aerodynamic coefficients and associated aerodynamic characteristics.

4.1 General features of OWN installation

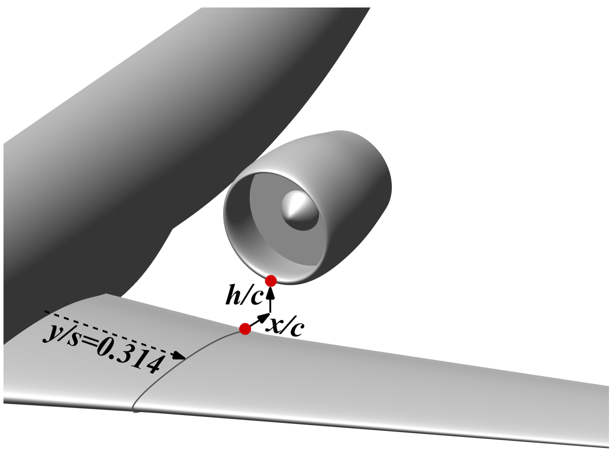

Fig. 4.1 *Sketch to illustrate the engine position definition for REF3*

The following section focuses on the impact of the OWN installation on the backward swept wing. For the engine placement above the wing, several options were outlined in section 1.1. The most promising engine position in combination with an UHBR engine is the installation along the wing trailing edge, so that the engine inlet is placed above the trailing edge. The spanwise engine position was defined at about one-third of the wing, close to the kink between inner and outer wing section. The exact engine position, as sketched in Fig. 4.1, is defined on the basis of two reference points, one on the wing and one on the nacelle. The wing reference point is defined at the wing trailing edge at *y/s = 0.314*. The nacelle reference point is defined on the engine highlight at 6 o'clock position. In the following, the engine position is specified by the horizontal (*x/c*) and vertical (*h/c*) distance between these two points. In the course of this initial investigation, the engine highlight is located at *x/c = 0.0* and *h/c = 0.135* to describe the general features of an OWN installation. The spanwise engine position is fixed at *y/s = 0.314*.

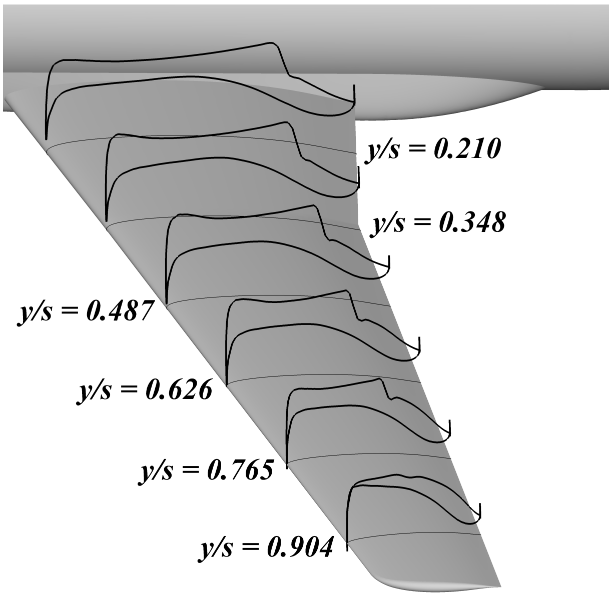

Fig. 4.2 *Pressure coefficient distributions of the WB at α=2.43° for the BSW*

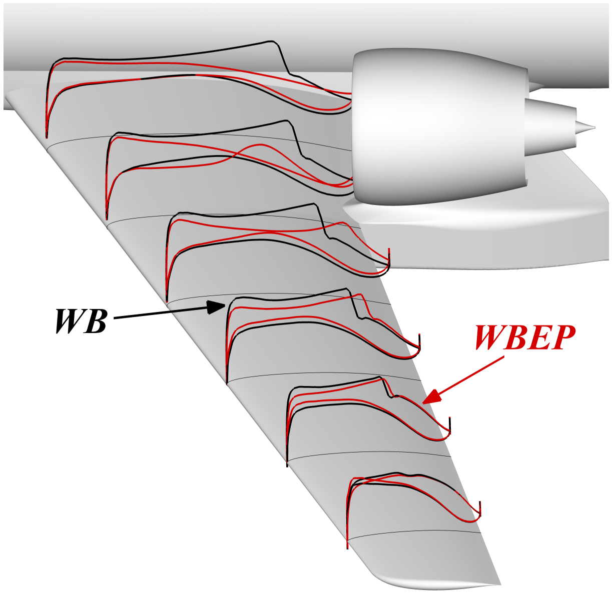

Fig. 4.3 *Impact of OWN engine on pressure distributions of backward swept wing at α=2.43°*

The comparison between WB and Wing/Body/Engine/Pylon (WBEP) configuration is performed at identical angle of attack α and additionally at constant lift coefficient $C_L = 0.469$ at $M = 0.78$ and $Re = 21.5\ mio$. The boundary conditions for the powered engine were specified on the basis of a previous design study with GasTurb[62] [63]. The pressure and temperature ratios for the conditions at the jet outlet planes inside the UHBR engine are given for the bypass as $T_t/T_{t0} = 1.102$ and $p_t/p_0 = 2.021$ and for the core through $T_t/T_{t0} = 2.552$ and $p_t/p_0 = 1.470$. The inlet mass-flow is coupled with the exhaust massflow, which is iteratively derived by the solver from the core and fan jet flow according to the defined engine settings. The resulting thrust is almost equivalent to the overall drag of the WBEP configuration, which results in steady flight conditions. An investigation by Renganathan et. al [64] stated that the interaction for an OWN configuration is dominated by the influence of the wing on the engine, but not vice versa. Thus, a difference between thrust and drag is considered to be acceptable for an aerodynamic evaluation without the necessity to establish an exact thrust/drag balance for all investigated engine positions.

At first, the WB and WBEP configuration at identical angle of attack $\alpha = 2.43°$ will be compared to avoid an additional influence of a varying incidence. Therefore, pressure distributions were extracted at six equidistant spanwise sections. For a qualitative overall impression of the wings surface pressure, the distributions are plotted as transparent overlay above the geometry in Fig. 4.2 for the WB. Note, the pressure distributions are reversed, so negative pressure coefficients point upwards. Thin black lines on the wing surface indicate the underlying airfoil section of each pressure distribution. The

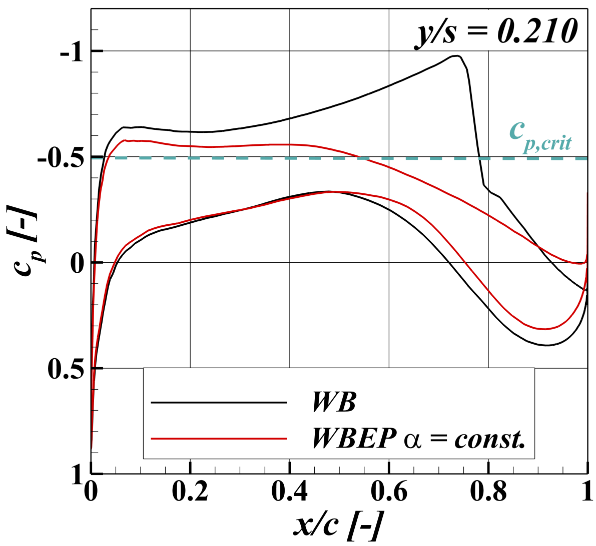

Fig. 4.4 *Pressure coefficient distributions of the WB and WBEP at y/s=0.210 (α=2.43°) for the BSW*

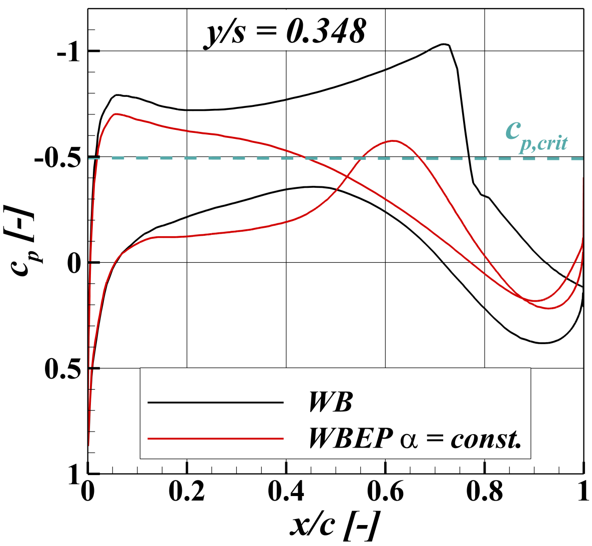

Fig. 4.5 *Pressure coefficient distributions of the WB and WBEP at y/s=0.348 (α=2.43°) for the BSW*

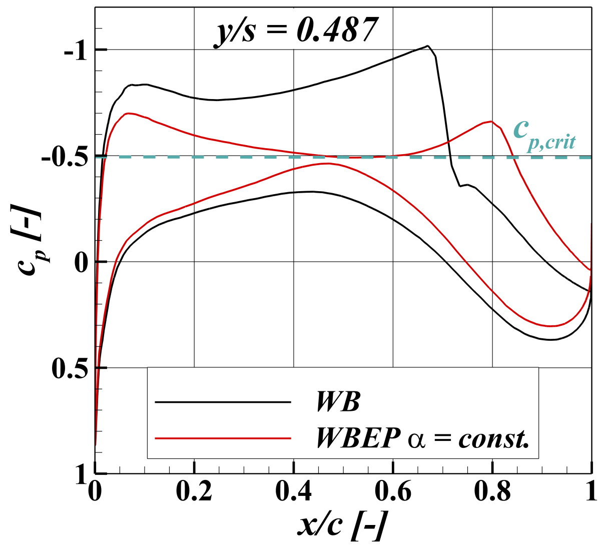

Fig. 4.6 *Pressure coefficient distributions of the WB and WBEP at y/s=0.487 (α=2.43°) for the BSW*

aerodynamic characteristics on the wing of the WB configuration, presented in 3.1.2, can be recognized. Based on these six sections, a typical transonic pressure distribution can be observed. First, the pressure distribution along the suction side features a strong decrease of c_p at the leading edge accompanied by local supersonic flow. Along the first two-thirds of chord the gradients of c_p are small and the local pressure coefficient remains at a low level. The segment of low pressure ends with a strong gradient, indicating the shock position. The appearance of the pressure distribution is a typical transonic rooftop pressure distribution. The pressure distribution on the lower wing is dominated by a rear loading in the aft wing section. For the inner sections, the relative chordwise shock position is closer to the trailing edge. With increasing wing span, the relative shock position shifts upstream until no distinct shock could be detected for the outmost section. This behavior correlates with the three-dimensional effects of a finite backward swept wing, described in 3.1.2. The transition from supersonic to subsonic speed, especially for the inboard wing, is associated with a strong shock. The shock correlates with a strong change in pressure resulting in high drag values.

The impact of the OWN installation on the pressure distributions is presented in Fig. 4.3. In this plot, the c_p-distribution for the WB (black) and WBEP (red) configuration at identical α are assembled to facilitate a qualitative assessment of the engine's presence. Starting with the most inboard section, an extensive increase of c_p on the rear wing, in front of the engine, can be observed. Simultaneously, a detailed plot of the c_p-distribution in Fig. 4.4 reveals a static pressure decrease at the wing trailing edge. This indicates a local flow acceleration, which is caused by the channel between nacelle, wing and fuselage.

The second c_p-distribution on the inner wing section in front of the engine, shown in Fig. 4.3, reveals a distinct increase of c_p on the upper surface from the leading edge down close to the wing trailing edge. In addition, the pressure coefficient on the lower wing surface alternates in comparison with the WB configuration. As highlighted in Fig. 4.5, the red pressure coefficient for the WBEP configuration increases over the first half of the section. Then, a distinct c_p decrease is traceable. This behavior is caused by the pylon mounted on the wing lower surface. The displacement effect of the pylon geometry induces first a flow deceleration in front of the pylon/wing junction, thus c_p decreases, followed by flow acceleration around the elliptical pylon shape.

The two mid sections in Fig. 4.3 feature a downstream shift of the final shock location in comparison with the WB. Moreover, an increasing pressure level of the suction peak and decreasing c_p along the wing lower surface can be observed for the outer c_p-distributions. The varying pressure level can be associated with a reduction of the effective angle of attack α_{eff} along the entire span of the WBEP configuration. However, this assumption contradicts the downstream movement of the shock, exemplary shown in Fig. 4.6 at $y/s = 0.487$. Typically, a decrease of α_{eff} in the linear range around the cruise operation point is associated with an upstream shift of the shock position. Thus the relocation must have an other cause. This feature will be investigated at a later stage. At first, the assumption of an decreasing α_{eff} between WB and WBEP for identical α will be evaluated. This change in α_{eff} implicates an impact on the spanwise load distribution. Consequently, a comparison between both configurations is presented in Fig. 4.7.

The spanwise distribution of the lift coefficient C_L is plotted along the y-axis over the normalized spanwise coordinate y/s. The spanwise lift distribution for the WB is colored in black, while the result for the WBEP at α=const. is represented by a red line. The engine location is marked with the aid of a vertical dashed line at $y/s = 0.314$. For both configurations, a similar variation of C_L for $0 < y/s < 0.13$ can be observed. This is caused by evaluating the lift coefficient over the entire aircraft including fuselage and belly. Starting from $y/s = 0$, C_L is rising up to a first maximum caused by an increasing presence of the belly in combination with large chordwise fuselage sections. Due to the normalization of the lift force with respect to the mean aerodynamic chord, the local lift coefficient $\delta C_L/\delta(y/s)$ obtains high values. Then, $\delta C_L/\delta(y/s)$ drops to a local minimum caused by the declining slice planes of the fuselage sections in y-direction.

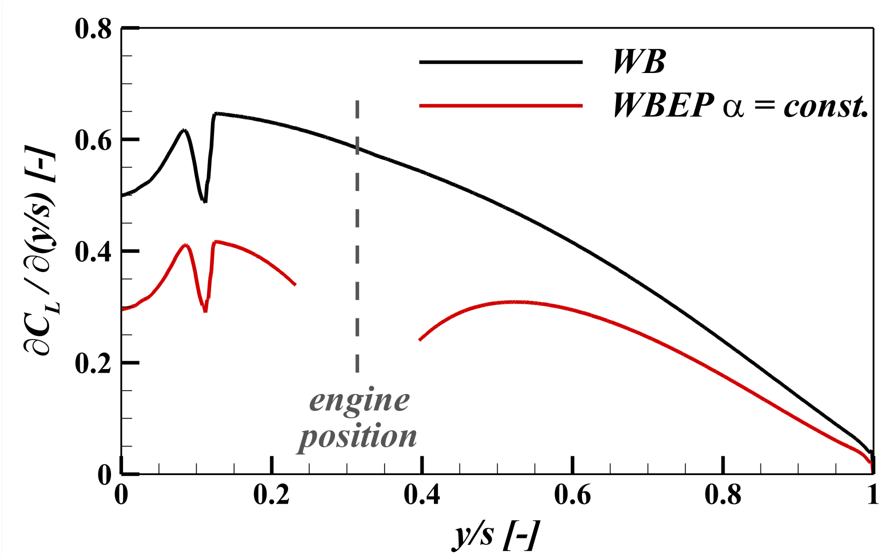

Fig. 4.7 *Spanwise lift distribution of WB and WBEP for α=const. for the BSW*

Simultaneous, the minimum marks the junction between belly and wing. The new increase of $\delta C_L/\delta(y/s)$ is based on spanwise slices, which contain shares of wing and fuselage. At the second local maximum, the lift integration over the extracted spanwise section includes only the wing. Based on Fig. 4.7, a distinct lift loss for the WBEP can be observed, caused by the OWN installation. Inboard of the engine, the local lift coefficient $\delta C_L/\delta(y/s)$ of the WBEP is reduced by one-third of the WB. Outboard of the engine, the relative local lift losses are even higher. For an increasing spanwise location, the difference in C_L between WBEP and WB is decreasing. Consequently, the OWN installation causes a decreasing effective angle of attack α_{eff}, which affects the entire wing and results in significant lift losses for an identical α.

To verify the hypothesis of a decreasing effective angle of attack, the local angle of attack is evaluated. Therefore, the local angle of attack α_{local} is calculated from

$$\alpha_{local} = arctan2\left(\frac{w}{u}\right) * 180°/\pi. \tag{4.1}$$

An analysis of the α_{local} for the WB and WBEP configuration at α=2.43° is presented in Fig. 4.8 and Fig. 4.10. Therefore, the flow field data is visualized on a volume slice, which is positioned about 10% x/c in front and parallel to the wing leading edge, as shown in Fig. 4.9. Red indicates high α_{local}, while blue represents $\alpha_{local} \leq 0°$. By comparing the extension of the red area, an impact of the OWN installation on α_{local} along the full wing span for α=const. can be identified. Around the fuselage, the highest values for α_{local} can be observed due to the flow around the inclined fuselage. The comparison of Fig. 4.8 and Fig. 4.10 gives the impression of an decreasing α_{local} due to the OWN installation. To quantify the change of α_{local} between WB and WBEP configuration, an extract of each data set was projected on an artificial plane to allow a direct quantification of $\Delta\alpha_{local}$.

The result is presented in Fig. 4.11. The green coloring in front of the wing represents a reduction of α_{local} by about 0.45° along the evaluated volume slice due to the OWN installation. This area ranges from the fuselage up to the wing tip and reaches a $\Delta\alpha_{local}$ of about -0.8° in front of the outer wing section. Thus it is proven, that the installation of the UHBR-OWN results in a reduced effective angle of attack at α=const..

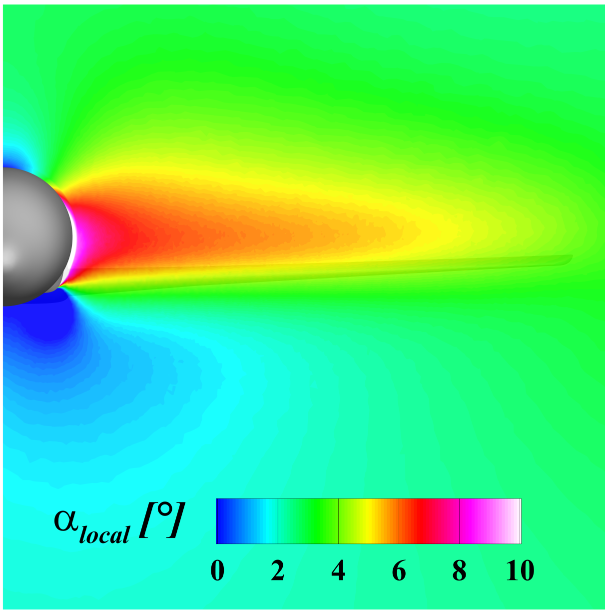

Fig. 4.8 *Local angle of attack in front of WB configuration on a volume slice parallel to the wing leading edge at α=2.43°*

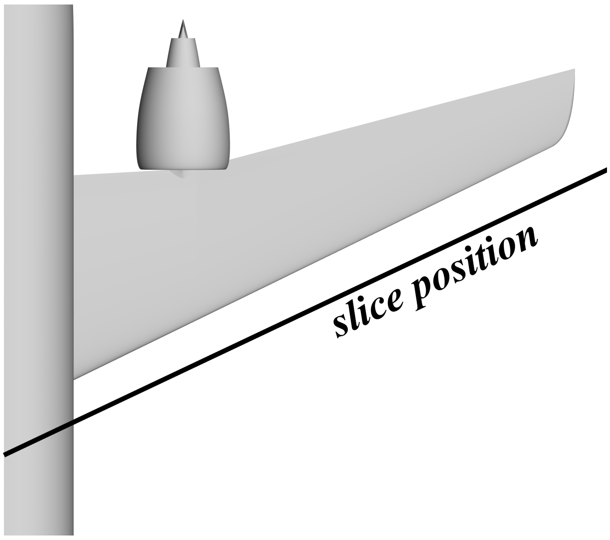

Fig. 4.9 *Slice position for analysis of local angle of attack*

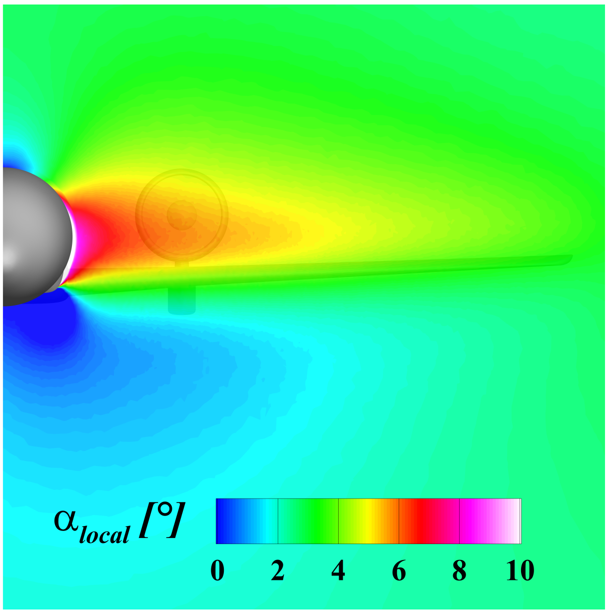

Fig. 4.10 *Local angle of attack in front of WBEP configuration on a volume slice parallel to the wing leading edge at α=2.43°*

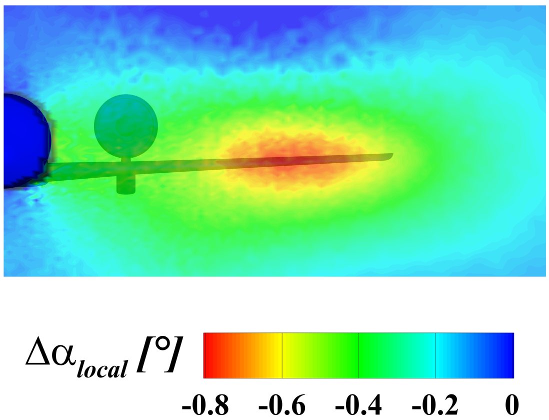

Fig. 4.11 *Visualization of $\Delta\alpha_{local}$ in front of the wing due to the OWN installation*

To emphasize the impact of the OWN on the transonic characteristic of the wing, iso-Mach lines were extracted from the volume solution. Regions for $M > 1$ are illustrated for identical spanwise locations for both WB and WBEP in Fig. 4.12. Note, additional supersonic regions on the nacelle are blanked out. Based on this visualization, a distinct reduction of the area of supersonic flow can be observed, especially for the three inner

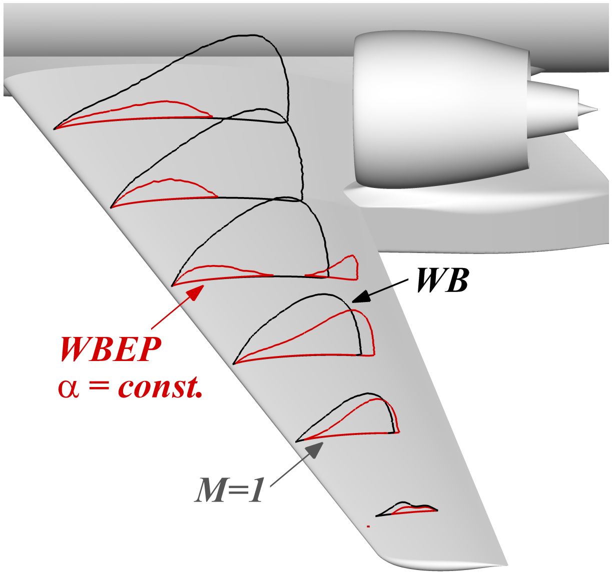

Fig. 4.12 *Regions of $M > 1$ for WB and WBEP at α=2.43° for the BSW*

sections. This agrees with Fig. 4.4 and Fig. 4.5 showing a forward shift of the shock location from $x/c \approx 0.8$ (WB) to about $x/c \approx 0.5$ (WBEP). Moreover, a double shock structure in the third section and a downstream shift of the shock position for the remaining outer sections can be detected for the WBEP.

In summary, the installation of an over-wing nacelle on a backward swept wing has a significant impact on the upper wing pressure distribution. Three main effects can be observed:

1. Pressure level on rear wing in front of the engine increases
2. Decrease of effective angle of attack α_{eff} along the entire wing span
3. Flow acceleration at wing trailing edge caused by the displacement effect of the nacelle

In total, the installation of an UHBR-OWN engine on the REF3 configuration causes an overall lift coefficient reduction by about 40% at identical α. Consequently, α needs to be increased to achieve a comparable lift coefficient C_L for the WBEP. The investigation of the resulting flow characteristics at identical C_L allows for a further insight into the interaction between powered engine and the upstream located wing.

Initially, an illustration of the areas of supersonic flow comparing the WBEP at α=const. (red) and WBEP at C_L=const. (green) with respect to WB is presented in Fig. 4.13. For this purpose α was increased by 1.42° to obtain the same lift coefficient as the WB configuration.

On the basis of this plot, a larger area of supersonic flow can be observed in all sections for the WBEP at C_L=const. However, the area increases mainly in vertical direction, while the shock positions remain nearly constant despite the increasing α. Only the outer sections reveal a minor downstream shift of the shock location, which meets one's exceptions due to an increasing incidence. In addition, the double shock characteristic

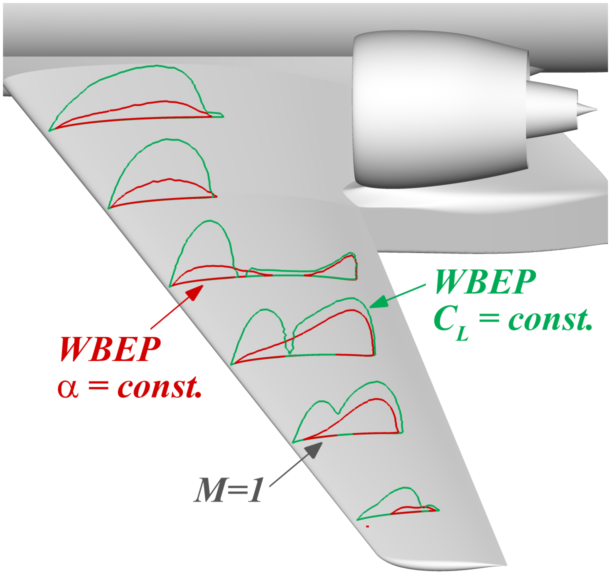

Fig. 4.13 *Regions of $M > 1$ for WBEP at C_L=const. and WBEP at α=const. for the BSW*

becomes more obvious and expands further outboard along the two mid-sections due to the increasing α and associated aerodynamic load.

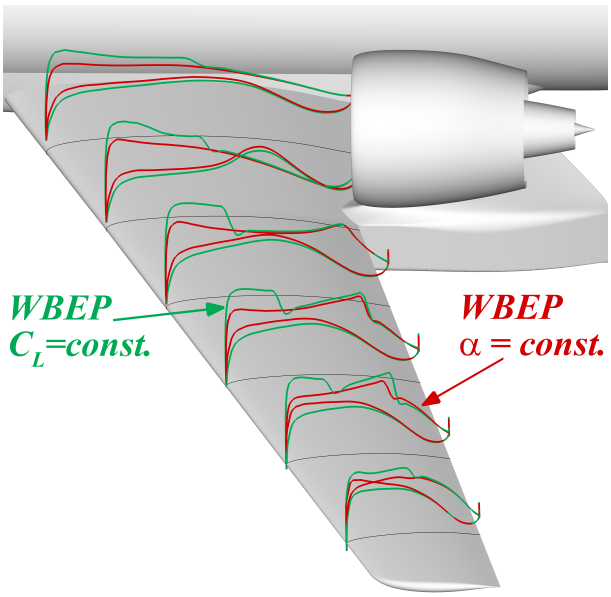

Fig. 4.14 *Qualitative pressure distributions comparing WBEP at C_L=const. and WBEP at α=const. for the BSW*

Continuing with an illustration of the surface pressure coefficient c_p, qualitative pressure distributions for both WBEP configurations are shown in Fig. 4.14 as transparent overlays based on the same six sections extracted along the wing span. Comparing against the WBEP at α=const., the effect of an increasing α becomes apparent along the wing leading edge. The pressure level on the lower wing surface is increased, concurrent the pressure level on the upper wing surface is decreasing right up to the shock position. Thus, the area enclosed by the pressure distribution is increasing, which implies an increasing aerodynamic force.

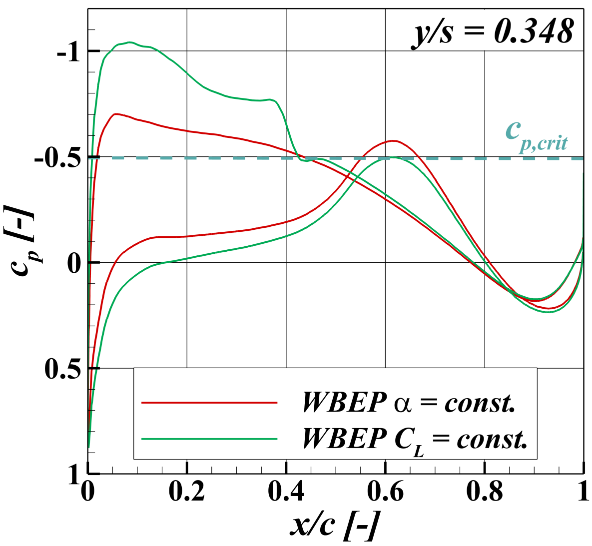

Fig. 4.15 *Pressure coefficient distributions of the WBEP for C_L=const. and α=const. at y/s=0.348 for the BSW*

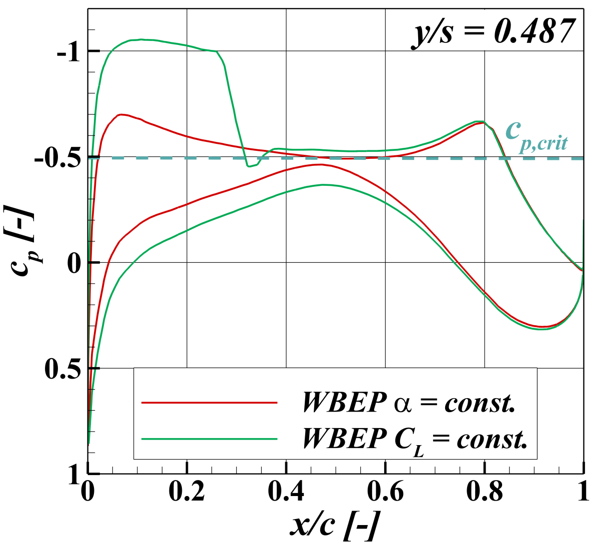

Fig. 4.16 *Pressure coefficient distributions of the WBEP for C_L=const. and α=const. at y/s=0.487 for the BSW*

Exemplary, two pressure sections are plotted in Fig. 4.15 and Fig. 4.16 for a detailed analysis. Therefore, the pressure coefficient c_p is plotted over the normalized local wing chord x/c. Additionally, the critical pressure coefficient $c_{p,crit}$ is plotted by a light blue dashed line to mark the transition between sub- and supersonic areas. Fig. 4.15 was extracted at $y/s = 0.348$ close to the engine's spanwise position. The pressure coefficient on the lower surface reveals the expected increase of c_p resulting from the increased α. The upper surface features a distinct pressure decrease up to $x/c \approx 45\%$. The indication of the critical pressure coefficient $c_{p,crit}$ clarifies, that the variation of the upper surface pressure is limited to the supersonic segment. Downstream of the transition from supersonic to subsonic speed, the static pressure coefficient is nearly identical for both configurations. Concluding from this observation, it can be assumed that the presence of the powered engine is dominating the pressure coefficients locally on the rear wing despite increasing the angle of attack by 1.42°. A similar behavior can be observed in Fig. 4.16, which shows the pressure distributions at $y/s = 0.487$. In case of the WBEP at C_L=const., this section reveals a distinct pressure increase of about $\Delta c_p \approx 0.5$ on the upper surface, resulting in a strong shock. Consequently, a disturbance is induced into the ensuing pressure distribution leading to a minor deviation from the rear upper surface distribution of the WBEP at α=const. Nevertheless, the shape and magnitude of the second pressure peak at $x/c = 80\%$ is almost identical for both configurations.

The preceding evaluation suggests a dominant impact of the powered engine on the upper rear wing pressure distribution. The shock locations on the inner wing sections are unaltered in spite of a distinct incidence increase. Therefore, a direct comparison of the surface pressure coefficients Δc_p between WBEP at C_L=const. and α=const. could provide further insights.

Fig. 4.17 shows a top view on the WBEP configuration. In this plot, red indicates a pressure increase from WBEP at α=const. to WBEP at C_L=const., while blue represents

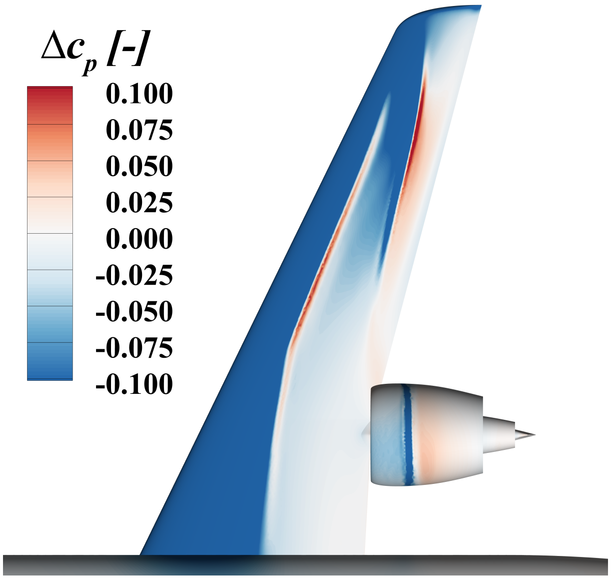

Fig. 4.17 *Pressure difference between WBEP at C_L=const. and WBEP at α=const. for the BSW*

a decrease of c_p. The light colored area highlights regions with almost no static pressure deviation. Because both simulations were performed on the identical grid, a differentiation of the surface pressure coefficient could be achieved. The blue region along the wing leading edge and outer wing describes the decrease of c_p caused by the increased α to obtain the target C_L of the WB configuration. The red stripes identify the shock positions, which intensifies with increasing aerodynamic loads but remain at the same chordwise position. Accordingly, the engine's impact propagates exclusively with an elliptical characteristic in the the area of subsonic flow. There, information are redirected both down- and upstream. The hyperbolic characteristic of supersonic flows forward information solely in downstream direction. Consequently can be assumed, that the chordwise shock position is defined by the subsonic streamtube induced by the powered engine.

Finally, the spanwise load distributions for the WB and both WBEP configurations are shown in Fig. 4.18. The shapes of the WBEP configurations are similar, showing a uniform increase of the local lift coefficient along the wing span. By comparison with the WB configuration can be stated, that the lift loss on the inner wing section is compensated by higher aerodynamic loads along the outer wing to achieve identical overall lift coefficients.

4.2 Impact of engine's thrust setting

In the previous section, a distinct impact of the engine's presence on the aerodynamic characteristic of the wing was found, especially at the rear section. To build up a superior understanding of the interference between engine and wing, the REF3 was investigated under consideration of a different engine power setting at target $\alpha = 2.43°$. For a detailed insight, the largest physically reasonable variation of the engine settings was realized by adjusting the power setting from cruise to zero net thrust (ZNT). Therefore, the boundary

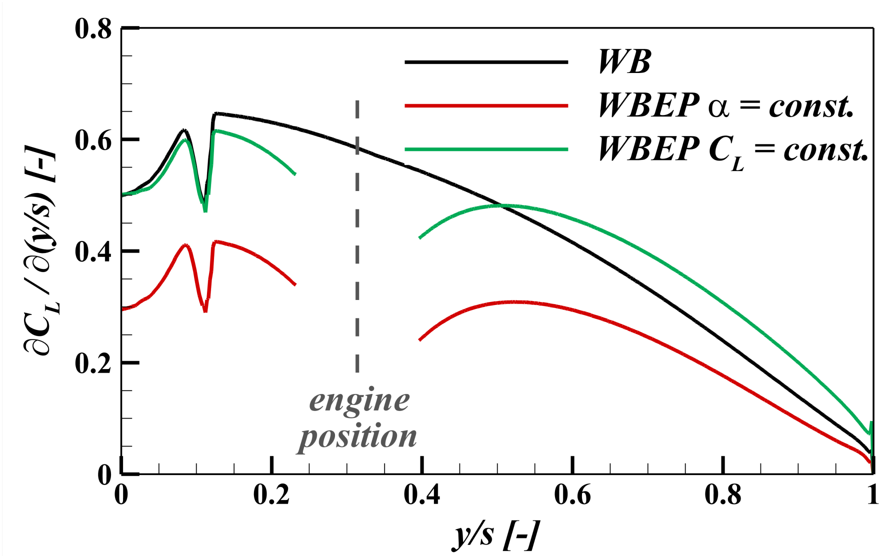

Fig. 4.18 *Spanwise lift distribution of WB, WBEP at α=const. and WBEP at C_L=const. for the BSW*

conditions at bypass and core outlet were set in order to simulate an approximately zero net thrust. This was achieved by choosing a pressure ratio of $p_t/p_0 = 1.49466$, which is equivalent to the isentropic ratio

$$\left(1 + \frac{\kappa - 1}{2} \cdot M_\infty^2\right)^{\kappa/\kappa-1} \tag{4.2}$$

at $M = 0.78$ and $\kappa = 1.4$. The temperature ratio was set to 1.

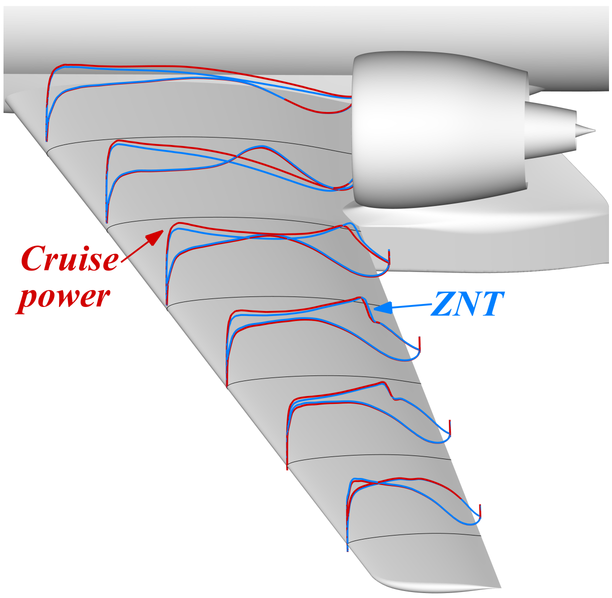

Fig. 4.19 *Qualitative pressure distributions comparing WBEP at α=2.43° for two varying engine settings on the BSW*

A qualitative illustration of the resulting pressure distributions along the REF3 is shown in Fig. 4.19. The red curves represent the known pressure distributions for the engine's design point in cruise flight, whereas the blue lines describe the pressure distributions in the presence of the OWN at ZNT. Based on this comparison, an increasing pressure level on the two inboard upper wing sections can be observed. The outer wing sections are featuring a decreasing suction peak and a slightly decreasing pressure level along the front lower wing due to the ZNT power setting. This implies a reduction of the effective angle of attack α_{eff}.

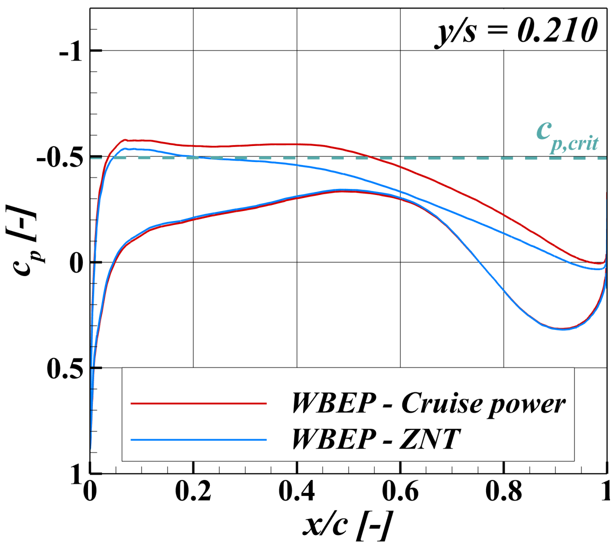

Fig. 4.20 *Pressure coefficient distributions of the WBEP at y/s = 0.210 for varying engine conditions on the BSW*

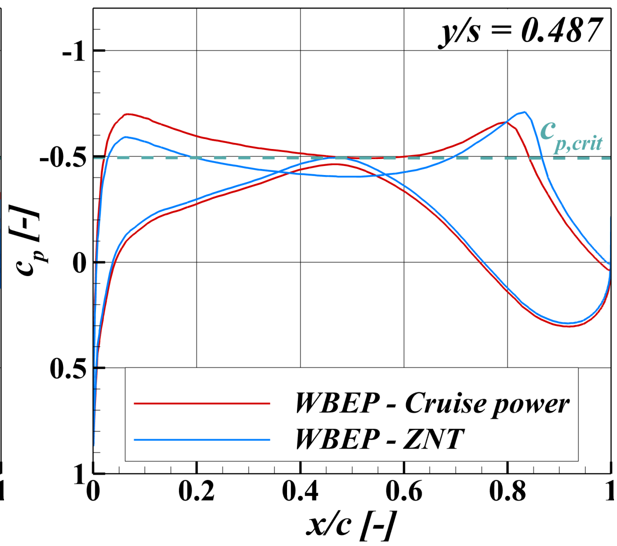

Fig. 4.21 *Pressure coefficient distributions of the WBEP at y/s = 0.487 for varying engine conditions on the BSW*

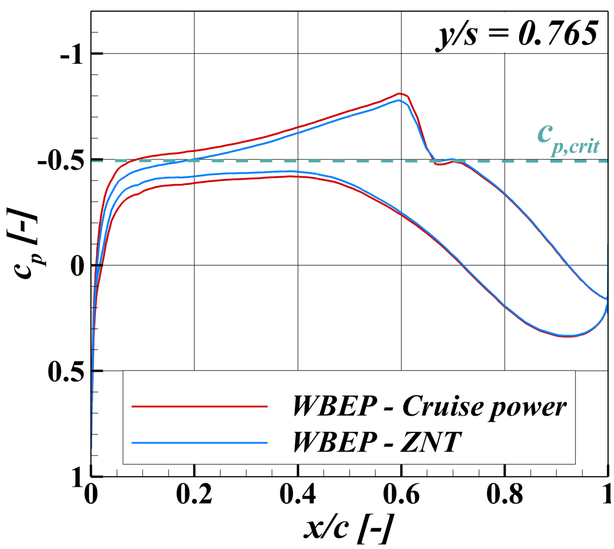

Fig. 4.22 *Pressure coefficient distributions of the WBEP at y/s = 0.765 for varying engine conditions on the BSW*

For a detailed analysis, selected pressure distributions are presented in more detail in Fig. 4.20 to Fig. 4.22. Fig. 4.20 compares the c_p-distributions for both engine settings at $y/s = 0.210$, inboard of the nacelle. The decreasing engine thrust and associated engine's inlet mass flow affects mainly the upper wing surface. The pressure level increases from trailing to leading edge, which results in a reduced area of supersonic flow. The wing lower surface is nearly unaffected by the varying engine thrust.

The increasing pressure level is also evident over the first 80% x/c at $y/s = 0.487$ in Fig. 4.21. By contrast, the second suction peak on the rear wing increases. The cause for this flow acceleration is attributed to the flow displacement, induced by the engine nacelle. In this case, the mass flow decrease leads to a stagnation line movement at the nacelle highlight towards the engine inlet. As a consequence, the flow coming over the wings upper surface experiences a stronger redirection and acceleration around the nacelle lip in comparison with the cruise thrust setting, which amplifies the effect. Thus, this additional flow acceleration and displacement along the nacelle lip affects the rear wing pressure level and results in an increasing suction peak at $x/c \approx 80\%$.

Comparing the c_p-distributions further outboard at $y/s = 0.765$, the effect of a decreasing effective angle of attack α_{eff} can be observed by a decreasing pressure difference between upper and lower wing surface along the front airfoil section. Contrary to expectations, the shock location remains at the same chordwise position. The expected upstream displacement of the shock due to the decreasing α_{eff} is probably compensated by the increased flow acceleration induced by the nacelle.

In summary, the engine power setting at ZNT influences the wing, which experiences a further increase of the upper surface pressure level and spanwise reduction of α_{eff} resulting in an overall lift reduction at constant α.

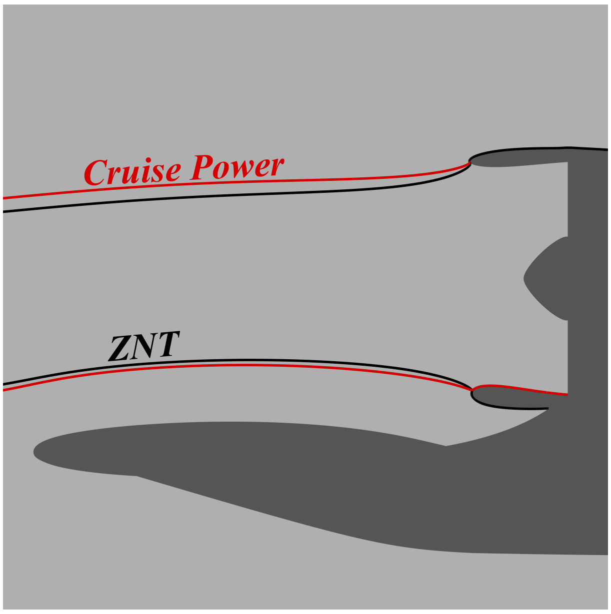

Fig. 4.23 *Visualization of the streamtubes comparing WBEP at α=const. for two varying engine settings on the BSW*

After discussing the effect of engine thrust variation on the wing aerodynamics, the following part will focus on the analysis of engine inflow and streamtube. At first, the streamtube of both engine power settings is compared in Fig. 4.23. This figure was created by extracting volume slices in the engine symmetry plane and drawing streamtraces, which take into account the three-dimensional velocity components, starting from the stagnation point at upper and lower nacelle leading edge. Fig. 4.23 illustrates the streamtube of the design cruise point in red and the ZNT power setting in black. On the basis of this visualization, the narrowing of the streamtube entering the engine as a result of the mass flow reduction and the associated thrust minimization, can be observed. Moreover, the movement of the stagnation points towards the fan caused by the mass flow reduction is traceable. Nevertheless, the streamtube deformation is not symmetrical. The boundary, which is closer to the wing surface, features a comparatively small displacement with respect to the upper streamtube boundary. This observation suggest, that the wing affects the streamtube.

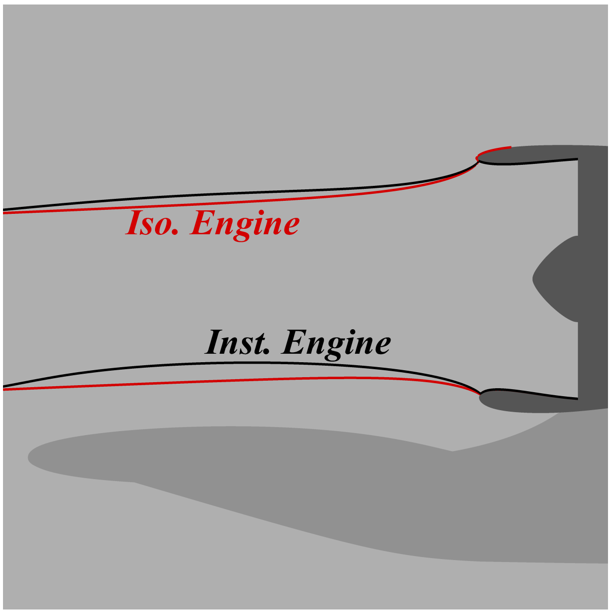

Fig. 4.24 *Visualization of the streamtubes comparing an installed and isolated engine at ZNT power setting on the BSW*

To assess the influence of the wing on the engine inflow, Fig. 4.24 compares the streamtubes of an installed and isolated engine at identical power setting, in this case ZNT. This plot reveals the deformation of the lower streamtube boundary induced by the wing's presence. The deformation complies with the shape of the upper wing surface.

In combination with the observations from Fig. 4.23, the wing seems to limit the expansion of the streamtube for higher thrust level. The necessary mass flow increase is achieved by sucking in additional air from the uncovered upper boundary of the streamtube. Thus the streamtube expansion can be found especially their.

For further evaluation of the interaction between wing upper surface and engine inflow, Fig. 4.25 illustrates the difference of the pressure coefficient c_p between the two engine settings in the engine symmetry plane. The difference is calculated by subtracting the results for the cruise point thrust level from the results for ZNT. Red coloring indicates a pressure increase, while blue represents a pressure decrease with respect to the ZNT case. In Fig. 4.25 a large red area on top of the nacelle leading edge can be observed. This implies an increasing pressure coefficient c_p by increasing the engine's thrust. The observation correlates with the already described flow acceleration along

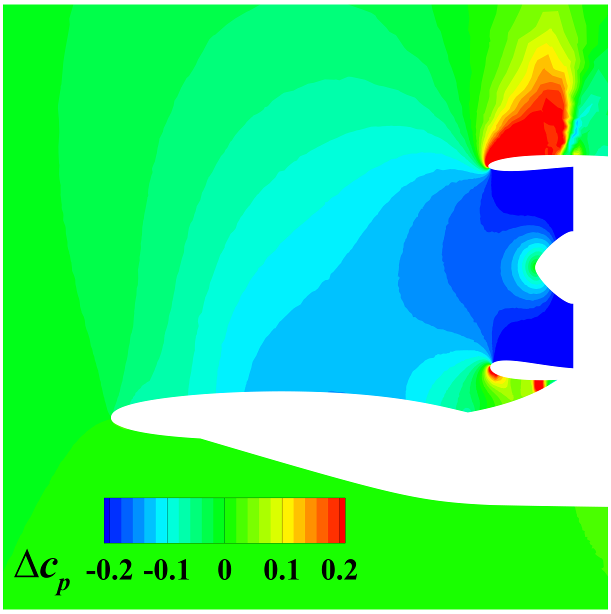

Fig. 4.25 *Visualization of pressure difference in engine symmetry plane between ZNT and cruise design point power setting for the BSW*

the outer nacelle leading edge due to the ZNT power setting. Furthermore, a blue curved channel between engine inlet and wing upper surface can be identified. In this region Δc_p totals approximately -0.12. This creates the impression, that the increasing thrust level generates a suction channel between engine and wing upper surface. That would explain the limited expansion of the streamtube towards the wing, which builds a physical blockage. Furthermore, a direct impact of the engine inlet pressure on the wing upper surface pressure level can be confirmed.

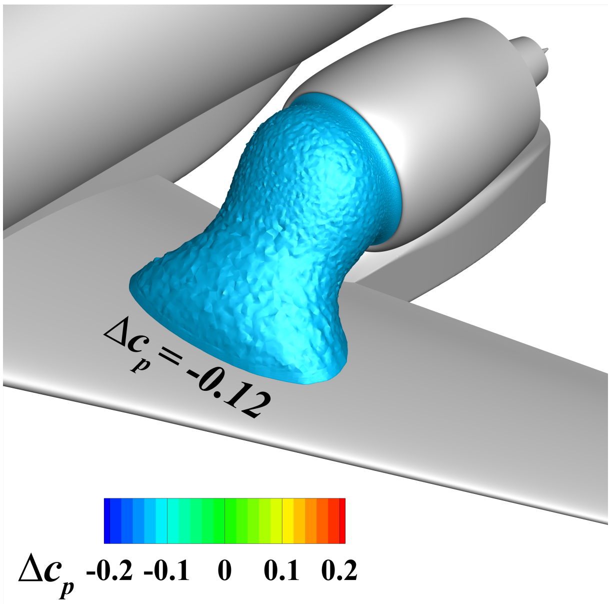

Fig. 4.26 *Visualization of iso-surface for Δc_p=-0.12 between ZNT and cruise design point power setting for the BSW*

The three-dimensional extent of this channel is visualized by an iso-surface for $\Delta c_p = -0.12$ in Fig. 4.26. The shape is reminiscent of a vacuum cleaner. Consequently, it can be stated that the upper wing surface pressure in front of the engine has a direct correlation with the engine thrust level. Thus, an increasing engine thrust, which implies a drop in c_p, results in a decreasing pressure coefficient on the wing upper surface in front of the engine inlet and by association an increasing lift coefficient, because the lower wing surface is unaffected.

4.3 Impact of OWN engine installation on drag coefficient

In the following, the impact of the OWN on the backward swept wing is analyzed with respect to aerodynamic coefficients and physical drag components. In the course of this analysis, WB and WBEP configuration of REF3 were evaluated at a constant lift coefficient of 0.465. The overall drag of the WBEP at target lift totals 317 drag counts (dcts.) at $\alpha = 3.84°$. Compared to the WB configuration, which achieves target C_L at $\alpha = 2.43°$, an increase of 66 drag counts has been ascertained due to the engine integration. The source of this significant drag rise needs to be identified. An evaluation of the drag components with the aid of a software allowing for a far-field drag analysis (ffd00 [29]) provides some indication. The diagram in Fig. 4.27 compares the drag components of the WB and WBEP configuration for C_L=const.. The bar diagram consists of four categories, which represent the physical drag breakdown provided by the far-field drag analysis. The bars are laid over each other for a simple comparison between WB (gray) and WBEP (green). Based on this figure, an increase in each individual drag component due to the engine integration can be observed. The largest relative increment

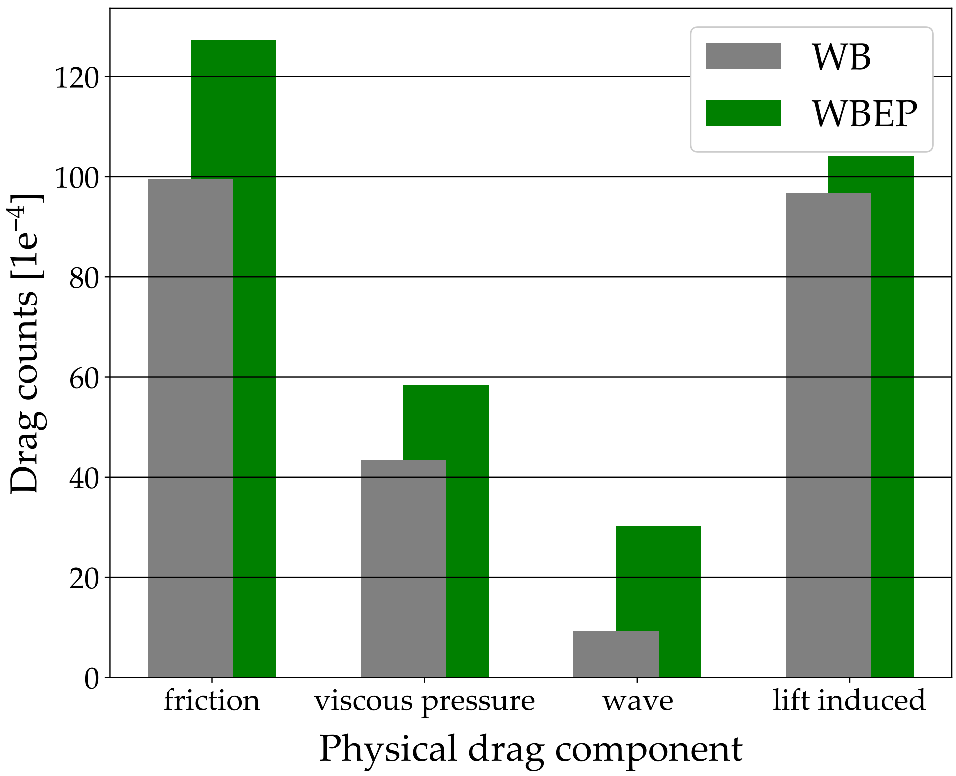

Fig. 4.27 *Drag components of WB and WBEP for the BSW*

can be assigned to the viscous pressure and wave drag components. The friction drag increment can be explained by the increase of the wetted area by about 27% due to the installation of the pylon and nacelle. The increased lift induced drag originates from the fact that the spanwise lift distribution of the WB configuration is disturbed by the OWN. Due to the engine installation the local lift along the inboard wing is reduced. This necessitates a higher α of 3.84° and correlates with an increase of the local lift on the outer wing, as shown in Fig. 4.18, to reach target lift. As already presented in the previous section, the engine installation at the wing trailing edge causes an substantial impact on the wing aerodynamics. Based on the chordwise c_p-distributions an alteration of the shock position was observed. For the WB configuration, the shock is positioned within the last quarter of the chord length. In contrast, due to the engine installation, the shock along the inboard wing section is shifted significantly upstream for identical C_L and a double shock structure on the outboard wing is evident.

Simultaneously, a comparison between isolated and installed nacelle, presented in Fig. 4.28, reveals an alteration of the area of supersonic flow around the nacelle. The dashed lines indicate $M = 1$, while black represents the installed configuration and red the isolated nacelle. On the upper nacelle, the enclosed area for the installed engine is almost double the size in comparison with the isolated nacelle. This is caused by positioning the engine in the high velocity flow field above the wing. The additional flow acceleration along the nacelle leads to the extended area of supersonic flow and thus higher pre-shock Mach numbers. The Exception to this can be found on the lower nacelle. There the area with $M > 1$ is significantly smaller due to the flow disturbance induced by the pylon intersection.

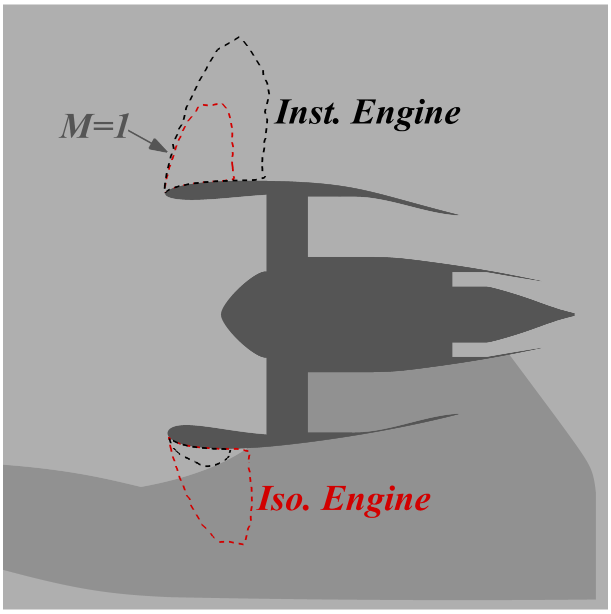

Fig. 4.28 *Comparison of areas of supersonic flow between installed and isolated nacelle on the BSW*

Taking the above described effects into account, the increase of wave drag due to the engine installation can be explained. The OWN installation on the REF3 is accompanied by a large pylon, which is not only used as structural joint between engine and wing but in addition serves as aerodynamic fairing for the main landing gear. Due to the dimension of the pylon fairing, a distinct aerodynamic impact can be assumed, especially on the drag coefficient. Thus the influence of the pylon should be taken into account and determined. Therefore, an additional configuration, composed of wing, body and engine (WBE), is analyzed.

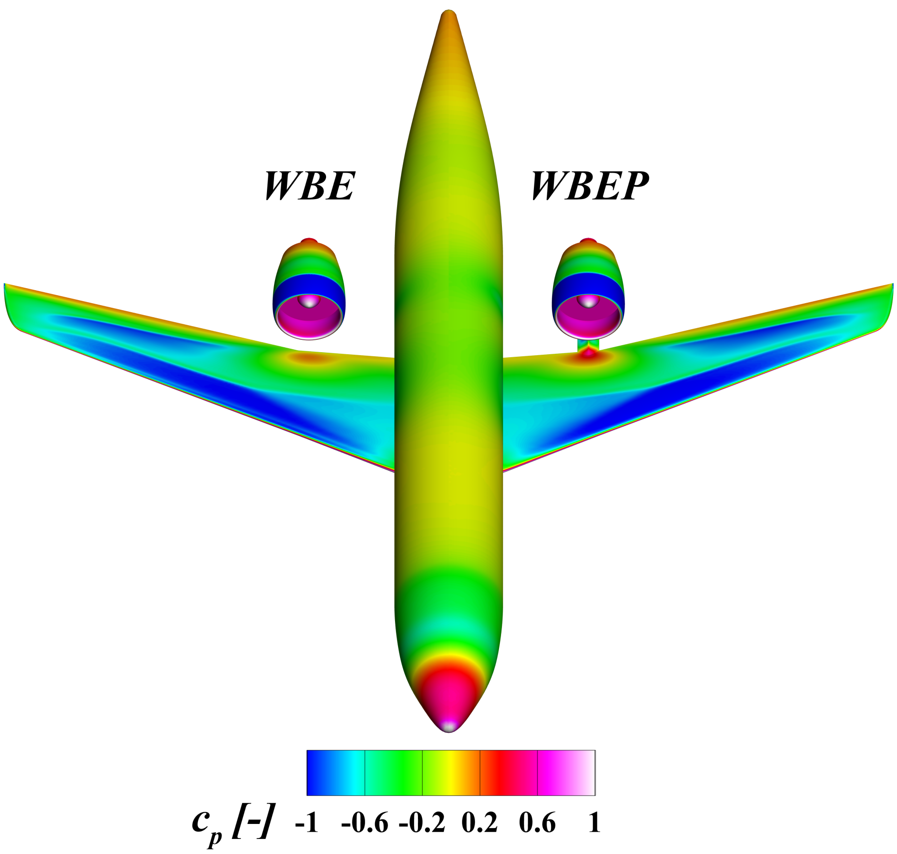

Fig. 4.29 *Comparison of surface pressure distribution on WBE and WBEP indentical α on the BSW*

At first, a comparison of the flow features of WBE (left) and WBEP (right) is provided in Fig. 4.29. The engines are located for both configurations at the identical position. To assure a similar upstream effect of the powered engine, the engine boundary conditions of the WBE configuration was defined by a target inlet mass-flow to assure an identical static pressure on the inlet face. This modification was necessary, since the absence of the pylon in the nozzle would have affected the engine mass-flow, while keeping the pressure and temperature ratios on the outlet faces unchanged. The identical static inlet pressure can be observed by the coloring of the surface with respect to c_p in Fig. 4.29. Furthermore, only small and local variations in the surface pressure distribution between WBE and WBEP can be noted. The upstream shift of the shock as well as the double shock structure on the outer wing can be identified in accordance on both sides. Nevertheless, an area with $c_p > 0$ is present below the free flying nacelle of the WBE configuration. This can also be identified on the WBEP configuration at the junction of pylon and wing. However, this comparison clarifies, that this local positive pressure coefficient is mainly induced by the OWN and just amplified by the presence of the pylon.

However, this first comparison reveals neither a beneficial nor detrimental impact of the enlarged pylon fairing on the aerodynamic characteristics of the wing. To assess the drag increase, the physical drag components of the WBE configuration were extracted with the aid of far-field drag analysis at target C_L and compared with WB and WBEP. The results are plotted in Fig. 4.30.

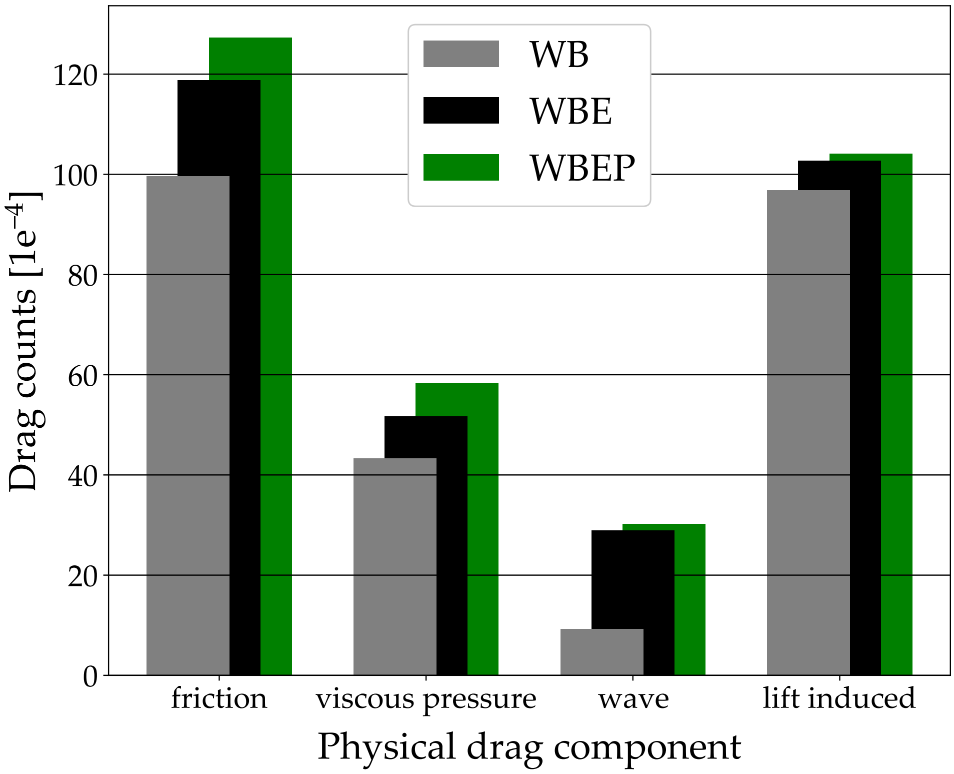

Fig. 4.30 *Drag components of WB, WBE and WBEP for the BSW*

The bar diagram consists of four categories, which represent the physical drag breakdown into friction, viscous pressure, wave and lift induced drag provided by far-field drag analysis. The bars are laid over each other for a simple comparison between WB (gray), WBE (black) and WBEP (green). Consequently, a comparison between the black and gray bar represents the impact of the installed but free flying nacelle and the difference between green and black bar is associated with the pylon installation. Almost the total difference in wave and lift induced drag between WB and WBEP is caused by the OWN installation. This correlates with the observations in Fig. 4.29, which reveals almost no impact of the pylon installation on the surface pressure distribution. Instead, only about half of the viscous pressure drag and two-third of the friction drag can be ascribed to the engine installation. An investigation of the isolated engine at $\alpha = 3.84°$ confirms, that the nacelle is accompanied by about 20 dcts. friction drag and 7 dcts. viscous pressure drag. This result of the isolated simulation matches the identified viscous pressure and friction drag increase between WB and WBE. However, the observed total wave drag increase between WB and WBEP configurations is about twice as large as the detected wave drag component for the isolated nacelle. Thus, it can be stated, that the OWN installation causes and disproportional wave drag increase. The remaining drag difference between WBE and WBEP is caused by the pylon. The drag increase correlates with the size of the large engine pylon. To assure this assumption, the spanwise distribution of the viscous pressure drag is shown in Fig. 4.31, comparing the WBE and WBEP configuration.

The viscous pressure drag is plotted along the y-axis over the normalized wing span.

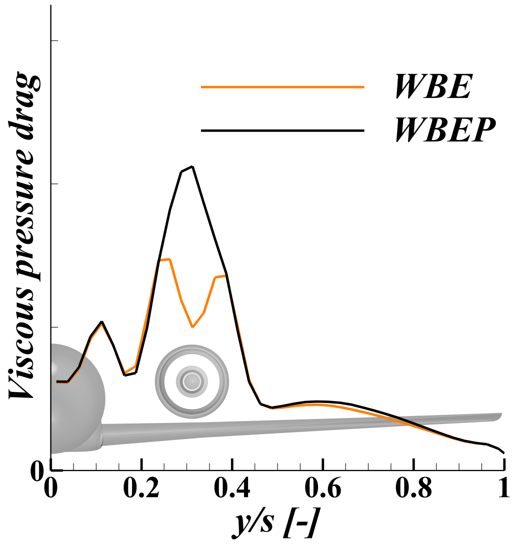

Fig. 4.31 *Spanwise distribution of viscous pressure drag for WBE and WBEP for the BSW*

For reference, the WBE configuration is plotted from rear view in the background. The orange line represents the WBE, while the results extracted from the WBEP are plotted in black. This comparison reveals a good agreement between the two configurations for $y < 0.24$ and $y > 0.39$. However, a significant deviation of the viscous pressure drag can be observed around the engine. In case of the WBE, two local maxima can be detected at the outer nacelle edges, including a drop at the nacelle axis. By contrast, the WBEP is dominated by one maximum at the engine symmetry plane, which is concurrently the pylon position. As a consequence, the viscous pressure increase can explicitly be assigned to the presence of the pylon and the associated boundary layer displacement thickness.

In summary, the OWN installation results in a significant drag rise of about 66 drag counts with disproportional large contributions of the wave and pressure drag components. The wave and lift induced drag is exclusively dominated by the pure presence of the ONW nacelle. Whereas the friction and viscous drag increase is evoked by the installation of OWN as well as pylon, since these parts are accompanied by a considerable increase in wetted area.

4.4 Interference effects on BSW caused by OWN position variation

The following section provides further insight into the general installation effects of an OWN on a backward swept configuration at transonic cruise conditions. For this purpose, the aerodynamic coefficients of the wing in dependence of the OWN engine position are analyzed. The spanwise engine position is kept unchanged at $y/s = 0.314$. Variations in horizontal and vertical direction are considered. However, the associated parameter space is limited because of the restrictions of the landing gear fairing below the nacelle, which was necessary for REF3. The horizontal engine position x/c ranges from -2.5% to +2.5% mean aerodynamic chord around the wing trailing edge. The vertical distance reflects an engine position between 10% to 15% mean aerodynamic chord length above the wing trailing edge. At first, aerodynamic coefficients of the wing component are shown to provide an overview and for identification of trends and samples for a subsequent detailed analysis. In Fig. 4.32 and Fig. 4.33 the componentwise lift and drag coefficients of the wing for all samples are illustrated within the investigated parameter space. The sampling was achieved with the aid of the surrogate-based method, described in section 2.5. The vertical distance is referred to as *h/c* and plotted along the y-axis. The x-axis represents the horizontal distanced as *x/c*. Negative values for *x/c* indicate an overlap of nacelle highlight and wing trailing edge. Each colored square corresponds to an investigated sample point, while the coloring reflects the contour value.

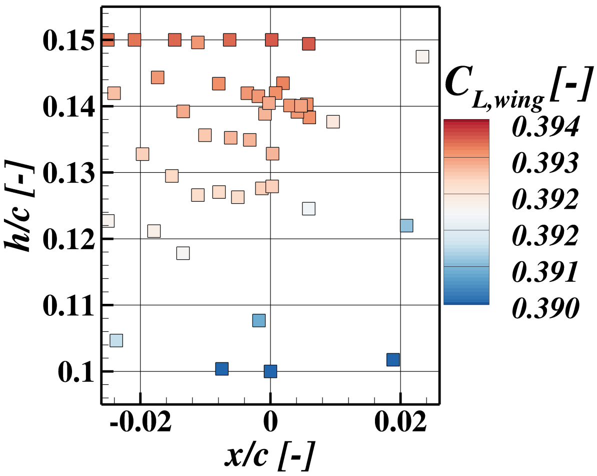

Fig. 4.32 *Componentwise lift coefficient C_L of BSW in the presence of the OWN*

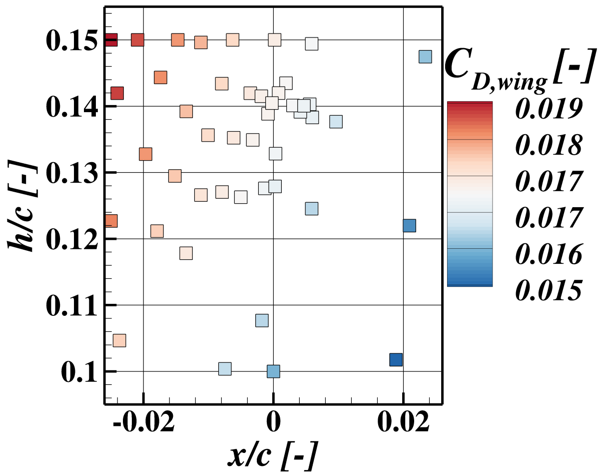

Fig. 4.33 *Componentwise lift coefficient C_D of BSW in the presence of the OWN*

All samples are performed with a target lift coefficient of $C_L = 0.46944$ for the full aircraft by adapting the angle of attack α. In case of disturbances of the wing lift, other aircraft components, e.g. fuselage or nacelle, have to compensate the wing lift variation to reach the overall target coefficient. As a result, a trend within the data can be observed. The variation of $C_{L,wing}$ over the parameter space is within a range of 0.5 lcts.. The lowest $C_{L,wing}$ is given for the minimal vertical distance between wing and nacelle. An increase of the wing lift component is traceable for an increasing overlap of nacelle and wing. But generally, the dominant trend depends on an increase of the vertical distance between nacelle and wing.

By contrast, the wing drag component $C_{D,wing}$ in Fig. 4.33 ranges from 150 up to 190 dcts.. This significant impact of the engine position on the wing drag component is dominated by the horizontal distance between nacelle and wing. The most downstream positions of the engine result in the lowest wing drag contribution. Moreover, a slight decrease of $C_{D,wing}$ with increasing vertical distance can be observed.

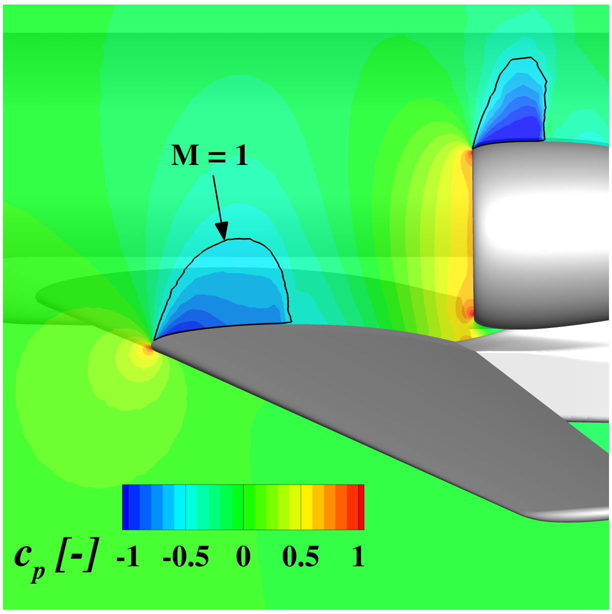

Fig. 4.34 *Volume slice showing the pressure coefficient at y/s=0.314 (h/c=0.10) for the BSW*

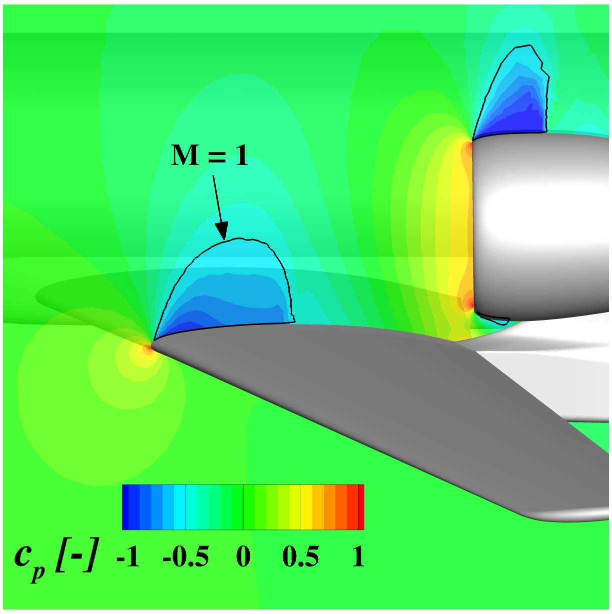

Fig. 4.35 *Volume slice showing the pressure coefficient at y/s=0.314 (h/c=0.127) for the BSW*

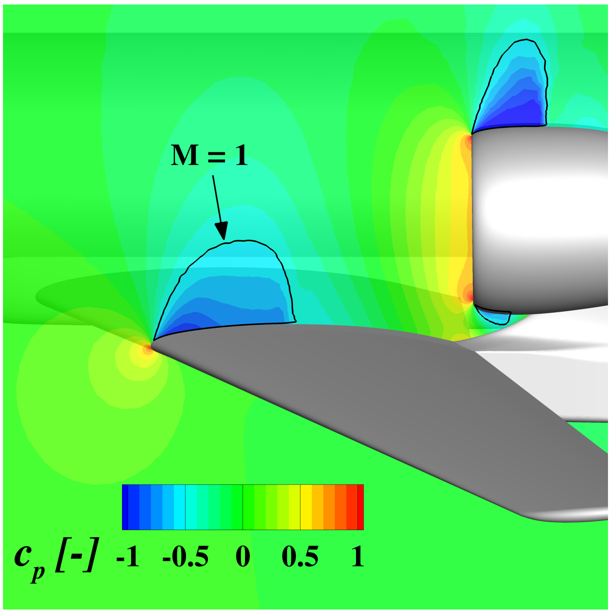

Fig. 4.36 *Volume slice showing the pressure coefficient at y/s=0.314 (h/c=0.15) for the BSW*

For detailed investigations with respect to the lift coefficient $C_{L,wing}$, three samples were selected at x/c=0 with vertical distances h/c of 0.1, 0.127 and 0.15. Fig. 4.34 to Fig. 4.36 provide a lateral view on the pressure coefficient c_p in a volume slice at the engine symmetry plane. For orientation, the slice is transparent and the critical pressure coefficient $c_{p,crit}$, representing M = 1, is marked by a black solid line. The contour level ranges from -1 to +1, while blue indicates pressure coefficients close to -1 and red colors c_p-values in the range of +1. The vertical distance between nacelle and wing is changing, whereas the horizontal distance is identical. All three figures feature a region of supersonic flow on wing and nacelle upper surface. With increasing vertical distance, a flow with $M > 1$ occurs on the nacelle lower leading edge. However, based on this illustration no obvious variations between the three configurations with respect to the wing can be observed.

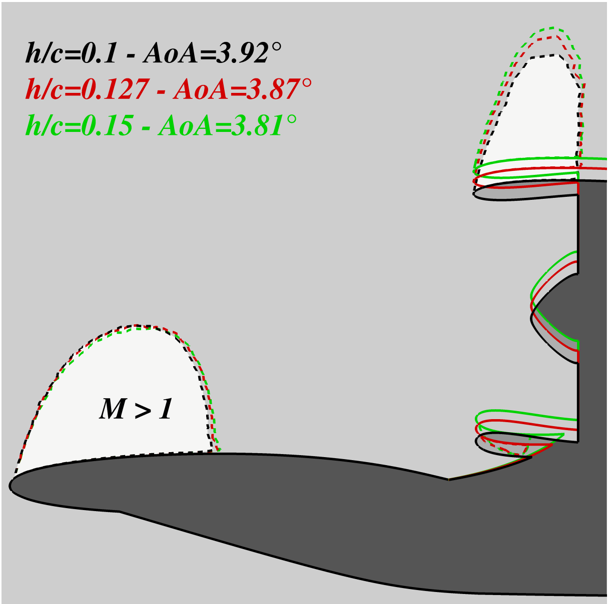

Fig. 4.37 *Comparison of the iso-Mach lines for varying vertical distance on the BSW*

Thus, the iso-Mach lines for M=1 are consolidated in Fig. 4.37. The plot shows a superposition of volume slices through the engine symmetry plane. Thus, not only the wing and engine cross section but also a cut through the pylon is visible in dark gray. To bring the dashed iso-Mach lines and different vertical engine positions in context, the colors of the nacelle outer edges and iso lines are harmonized. Furthermore, the regions of supersonic flow are exemplary highlighted white for the configuration with $h/c = 0.1$. The legend additionally provides the necessary angle of attack α to achieve target C_L. Based on Fig. 4.37, a minimal downstream shift of the shock position can be observed with increasing vertical distance. In addition, it should be noted, that the angle of attack decreases from 3.915° to 3.81° with increasing vertical distance. Thus, it can be stated that the shock position shifts downstream despite a decreasing α.

However, the variation of $C_{L,wing}$ cannot solely be attributed to the alterations of the area of supersonic flow. For that reason, the surface pressure distributions for the three samples are plotted in Fig. 4.38. The pressure coefficient c_p is plotted reverse along the y-axis over the normalized wing chord x/c. In addition, the figure contains a zoomed section around the shock position. Note, the pressure distribution visualizes mainly the wing upper surface. The lower wing surface is cut at about x/c=0.25 due to the intersection of wing lower surface and engine pylon. The coloring for the identification of the engine positions is identical with Fig. 4.37. Based on the pressure distributions, the downstream shift of the shock is confirmed. Moreover, an expected increasing $c_{p,min}$ for an decreasing α can be detected. The reason for the increasing lift coefficient can be found along the rear wing. The pressure coefficient along the upper surface decreases with increasing vertical distance. Concluding from this observation, a direct impact of the nacelle's presence on the pressure coefficient along the wing upper surface can be stated. With increasing vertical distance, the wing is less affected by the OWN. Thus the

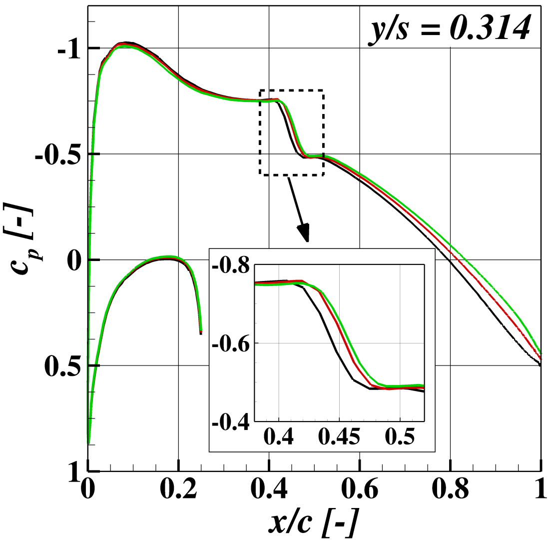

Fig. 4.38 *Comparison of the pressure distributions for h/c=0.1 (black), h/c=0.127 (red) and h/c=0.15 (green) on the BSW*

integral area of the lift curve increases due to an decreasing pressure coefficient along the upper rear wing. Consequently, in the area of the engine connection more lift can be generated by the wing resulting in an increasing $C_{L,wing}$.

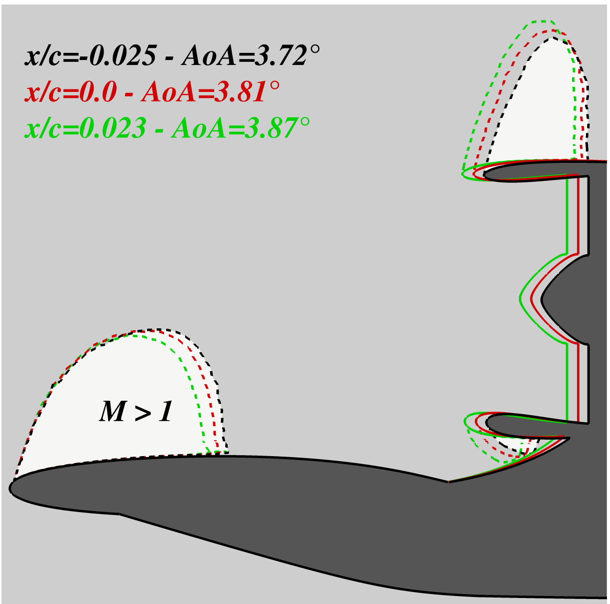

Fig. 4.39 *Comparison of the iso-Mach lines for varying horizontal distance on the BSW*

The detailed analysis of the trend for the drag coefficient $C_{D,wing}$ is based on three samples at about 0.15 h/c for -0.025 x/c, 0.0 x/c, and 0.023 x/c. Fig. 4.39 shows a superposition of volume slices through the engine symmetry plane analogous to Fig. 4.37. The wing, engine and pylon cross section is visible in dark gray. Different colors were selected to bring the dashed iso-Mach lines and different vertical engine positions in context. Furthermore, the regions of supersonic flow are exemplary highlighted white for the configuration with $x/c = -0.025$. The legend additionally provides the necessary angle of attack α to achieve target C_L.

Starting from the engine position with the largest overlap of wing and nacelle (green) an increasing area of supersonic flow by a downstream shift of the engine can be noted. The corresponding angle of attack decreases with increasing horizontal distance. This trend is reflected by the decreasing area of supersonic flow on the nacelle, which is located at similar mounting height. The target lift values for the configuration with distinctive overlap of nacelle and wing was reached for α=3.87°. Whereas the configuration with most downstream located nacelle achieves target lift at α=3.72°. In addition, a direct correlation between horizontal engine position and wing shock location can be identified. The magnitude of engine and shock displacement are in the same order of magnitude. A comparison of the pressure distribution provides further details.

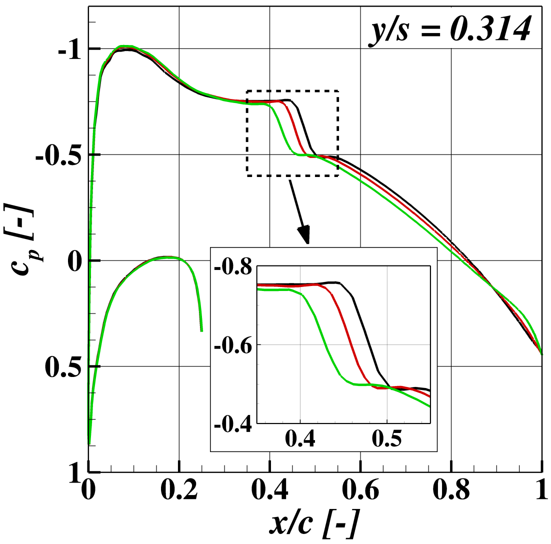

Fig. 4.40 *Comparison of the pressure distributions for x/c=-0.025 (black), x/c=0.0 (red) and x/c=0.023 (green) on the BSW*

Fig. 4.40 presents the pressure coefficient c_p plotted reverse along the y-axis over the normalized wing chord x/c. In addition, the figure contains a zoomed section around the shock position. As in Fig. 4.38, the pressure distribution depicts mainly the wing upper surface. The lower wing surface is cut at about x/c=0.25 due to the intersection of wing lower surface and engine pylon. The coloring for the identification of the engine positions is identical with Fig. 4.39. The comparison of the c_p-distributions confirms the relocation of the shock by about 5% due to the horizontal engine shift from -2.5% x/c to +2.3% x/c. On the rear wing the pressure level is lower for the engines positioned further aft. The distributions are crossing each other at about 90% x/c till they reach almost identical c_p-levels at the wing trailing edge. Consequently, the horizontal engine position has a minor impact on the wing lift in comparison with the vertical engine position. Instead, the evaluation of the horizontal positions implies a significant impact on the drag coefficient. However, the previous analysis provides no clear evidence for the strong wing drag increase, resulting from the upstream shift of the nacelle. Therefore, a far-field drag analysis was conducted to gather more information regarding the origin of drag increase.

Tab. 4.1 *Drag breakdown for horizontal position variation*

		Horizontal position x/c		
		-0.025	*0*	*0.023*
Drag components	*friction drag*	127.4	127.4	126.7
	vis. pressure drag	61.5	59.0	84.3
	wave drag	38.8	30.3	25.1
	induced drag	104.4	103.9	107.4
	Total drag	332.1	320.6	343.5

The physical drag breakdown is listed in Tab. 4.1. Each column represents an engine position. The physical drag components are listed along the rows including the overall total sum. The friction drag component is nearly constant over the three different horizontal engine positions. The viscous pressure drag component is decreasing for an increasing overlap between nacelle and wing. By contrast, the wave drag component increases for an increasing overlap. The induced drag component exhibits minor changes, but an increase by about 3 dcts. for the most aft engine position is traceable. Because of the opposed trends for viscous pressure and wave drag, the drag minimum can be found for the location of the nacelle highlight above the wing trailing edge.

Following, the origin of viscous pressure and wave drag variation will be investigated by visualizing the three-dimensional flow field. Three configurations are presented in detail. First, the focus is set on local regions with supersonic flow. Therefore, not only one half of the aircraft is presented but the full aircraft by mirroring the flow solution. Thus, features outboard as well as inboard of the engine and the pylon can be detected through the transparent fuselage. The surface is colored with respect to the pressure coefficient c_p. To detect the volumetric extent of supersonic flow, iso-surfaces representing $M = 1.2$ are plotted in magenta to stand out from the surface contour. In Fig. 4.41 to Fig. 4.43 three main supersonic flow regions can be identified: at the wing leading edge, around the nacelle leading edge, and outboard wing trailing edge. For the most upstream position, the second shock along the outer wing trailing edge expands. In addition, the largest region of supersonic flow on the nacelle is present for this engine position, which is confirmed by Fig. 4.37. By shifting the engine downstream, both regions of supersonic flow, on the nacelle and outer wing, shrink. Thus, it can be assumed that the wave drag component decreases, which would in turn explain the wave drag variation from 38.82 dcts. for x/c=-0.025 to 25.13 dcts. for x/c=0.023.

Viscous pressure drag is an indicator for the boundary layer displacement thickness induced exemplary by geometries or flow separations. Since the geometry variations are only minor, the reason for the significantly increased viscous pressure drag must be expected to be caused by flow separations. Instead of visualizing $c_f < 0$, iso-surfaces for flow velocities of $-1m/s$ in x-direction are illustrated in Fig. 4.44, Fig. 4.45, and Fig. 4.46 to identify critical regions and illustrate the accompanied displacement thickness. Note, the illustration with the aid of $x_{vel} = -1\text{m/s}$ does not represent the exact size of the flow separation, but is used as indicator for the volumetric expansion of reverse flows. The

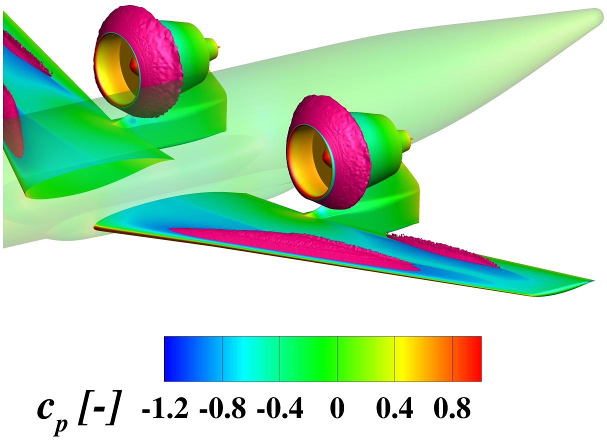

Fig. 4.41 *Visualization of Iso-Mach surfaces for M=1.2 (x/c=-0.025) for the BSW*

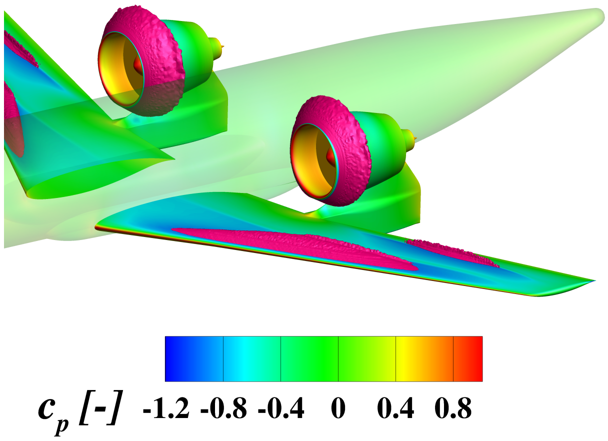

Fig. 4.42 *Visualization of Iso-Mach surfaces for M=1.2 (x/c=0.0) for the BSW*

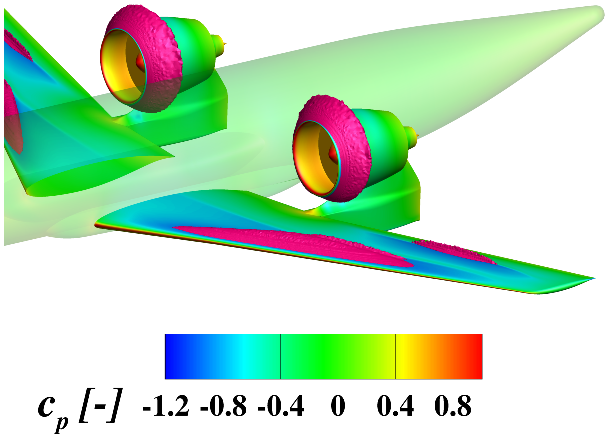

Fig. 4.43 *Visualization of Iso-Mach surfaces for M=1.2 (x/c=0.023) for the BSW*

three configurations are presented analogous to Fig. 4.43. However, the contour is not colorized by any variable but kept neutral in gray. The iso-surfaces, indicating flow separations, are colored in magenta as contrast to the surface shade.

In case of the foremost engine position ($x/c = -0.025$), flow separations on the inboard and outboard nacelle are traceable just behind the low pressure region around the nacelle leading edge. Thus, a shock induced flow separation can be presumed. Furthermore, a small flow separation can be observed on the inboard pylon at the junction with the nacelle trailing edge. For the engine position at $x/c = 0.0$ the nacelle flow separation is

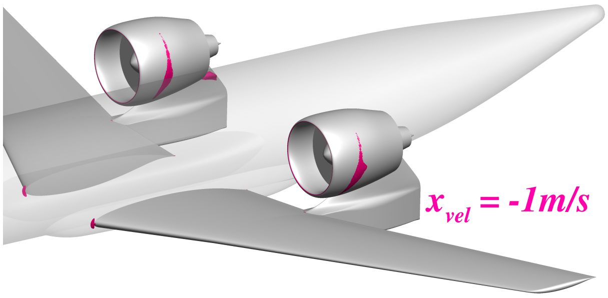

Fig. 4.44 *Visualization of iso-surfaces for x_{vel}=-1 m/s (x/c=-0.025) on the BSW*

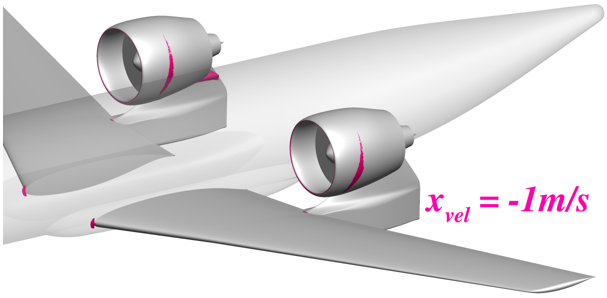

Fig. 4.45 *Visualization of iso-surfaces for x_{vel}=-1 m/s (x/c=0.0) on the BSW*

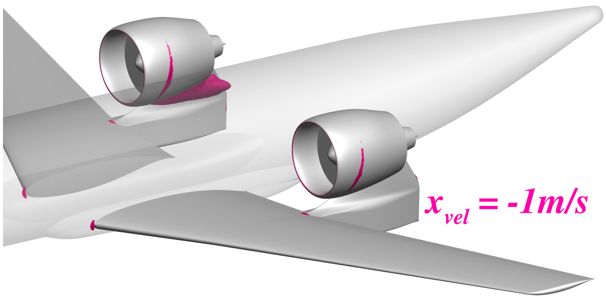

Fig. 4.46 *Visualization of iso-surfaces for x_{vel}=-1 m/s (x/c=0.023) on the BSW*

reduced in comparison with the the engine position at $x/c = -0.025$. In contrast, the volume of return flow at the inboard pylon trailing edge is increased. For the most aft engine position at $x/c = 0.023$, the flow separation on inner and outer nacelle is nearly vanished. However, a large flow separation occurs in the inner junction of nacelle and pylon. The starting point of this flow separation is the intersection between pylon leading edge and nacelle lower surface. As shown in Fig. 4.39 the area of supersonic flow ends just in front of the pylon leading edge, which introduces an additional flow disturbance. This finally leads to a flow separation at the very front of the pylon nacelle junction. These observations match the behavior of the viscous pressure drag. By shifting the engine from the foremost engine position downstream, the flow separations on the nacelle become smaller associated with an decreasing viscous pressure drag. Accompanied by the large flow separation on the pylon for the most downstream position, the viscous pressure drag increases by about 25 dcts.

Summarizing, the vertical distance between nacelle and wing affects the pressure coefficient on the rear wing and causes there, at the spanwise location of the engine, a local lift reduction. Thus the REF3 needs to operate at a higher angle of attack to achieve the identical overall lift coefficient C_L by generating additional lift on other components, like fuselage and nacelle. A distinct correlation between wing drag component $C_{D,wing}$ and horizontal engine position was found. An overlap of nacelle highlight and wing trailing edge implies a significant drag rise on the wing component due to the presence of a double shock on the outer backward swept wing. This effect is superimposed by a drag rise induced by a distinct flow separation in the pylon nacelle junction for the most downstream engine position. The particular flow separation can be addressed to the special pylon design of the REF3, which was not adapted with regard to varying engine position to suppress such phenomena.

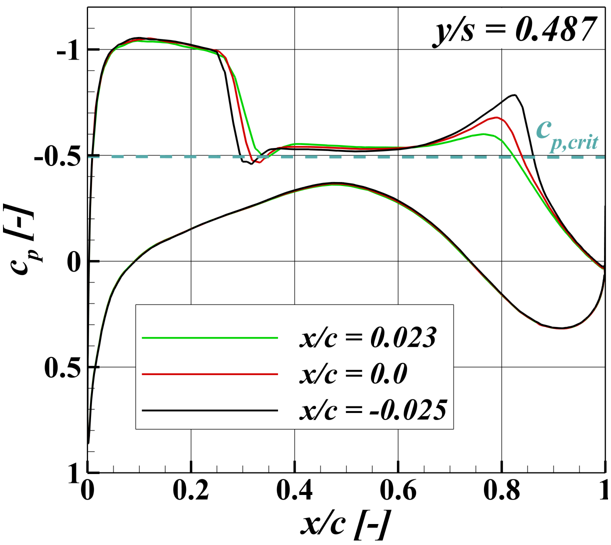

Fig. 4.47 *Comparison of pressure distributions at* $y/s = 0.487$ *for varying horizontal engines positions on the BSW*

As complement, the horizontal position variation can be utilized to examine the low pressure region on the outer rear wing to clarify if the nacelle is the correlating cause as initially assumed. While describing the general impact of the OWN on the backward swept wing at the beginning of this chapter, a downstream shift of the shock position on the outer wing could be observed (Fig. 4.6), despite the assumption of a decreasing effective angle of attack. This contradiction was not explained yet. The cause for this behavior can be induced by the nacelle displacement and overlap with the backward swept outer wing section. This leads to the assumption, that the flow acceleration has to increase by shifting the engine upstream, resulting to an increasing interference effect. For verification, pressure distributions at $y/s = 0.487$ for the three horizontal engine positions are compared in Fig. 4.47. Beside the pressure distribution, the critical

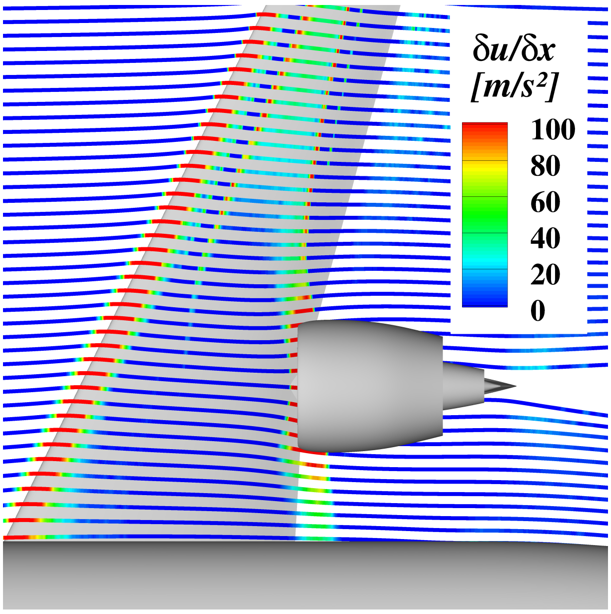

Fig. 4.48 *Visualization of $\delta u/\delta x$ along ribbons based on the velocity vector for the BSW*

pressure coefficient $c_{p,crit}$ is marked with the aid of a light blue dashed line. The pressure distributions verify a direct interaction between nacelle and the low pressure region at $x/c \approx 0.8$. The most upstream engine position at $x/c = -0.025$ (red) induces a distinct flow acceleration, while the remaining pressure distribution is unaffected in comparison with the other distributions, except for the shock location. By shifting the engine downstream, therefore increasing the distance between nacelle and wing, the pressure peak flattens. Consequently, the flow acceleration around the nacelle leading edge is amplified with increasing overlap between engine and wing.

For completion, the configuration with the largest overlap of $x/c = -0.025$ was utilized to visualize the velocity gradient $\delta u/\delta x$ as contour along ribbons following the local velocity vector. The ribbons were extracted on a z-plane, which was positioned at the height of the lower nacelle leading edge. Fig. 4.48 reveals in a top view on the one hand, the displacement effect of the nacelle on the approaching flow and the redirection in spanwise direction. One the other hand, the flow acceleration around the nacelle is visible due to the ribbons coloring, which spreads in inboard and outboard direction and expose a interaction with the upstream shock on the outer wing. Consequently, it can be stated that the OWN installation not only creates a channel between wing, fuselage and nacelle but induces additionally a flow acceleration on the outer wing, resulting in a low pressure peak along the rear wing.

5 Aerodynamic impact of an OWN on a forward swept wing

Following on the investigations of installation effects caused by an OWN in combination with a backward swept wing (BSW), this chapter will deal with the aerodynamic installation effects between OWN and FSW. Therefore, the principal phenomena for an arbitrary over-wing engine position was investigated on the basis of the REF4 in combination with an UHBR engine. Subsequently, the OWN installation was investigated analogous to chapter 4 regarding their impact on pressure distributions, aerodynamic coefficients and associated aerodynamic characteristics by modifying the engine position.

5.1 General features of OWN installation

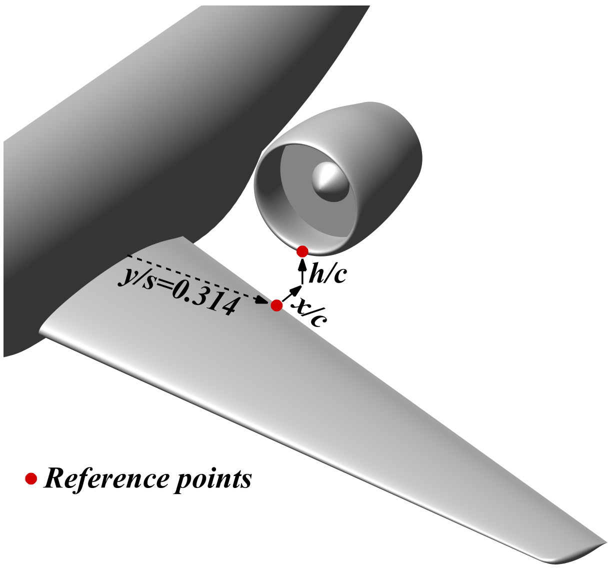

Fig. 5.1 *Sketch to illustrate the engine position definition for REF4*

The following section will focus on the interference effects between OWN and forward swept wing. The analysis will be obtained on the basis of the REF4 configuration with engines installed at identical relative position, as defined for REF3. This implies a spanwise location at $y/s = 0.314$ as well as a horizontal and vertical distance of $x/c = 0.0$ and $h/c = 0.135$ between wing trailing edge and the engine highlight at 6 o'clock position, as sketched in Fig. 5.1. Furthermore, identical pressure and temperature ratios on the engine outlet planes were chosen, defining the power setting in cruise flight.

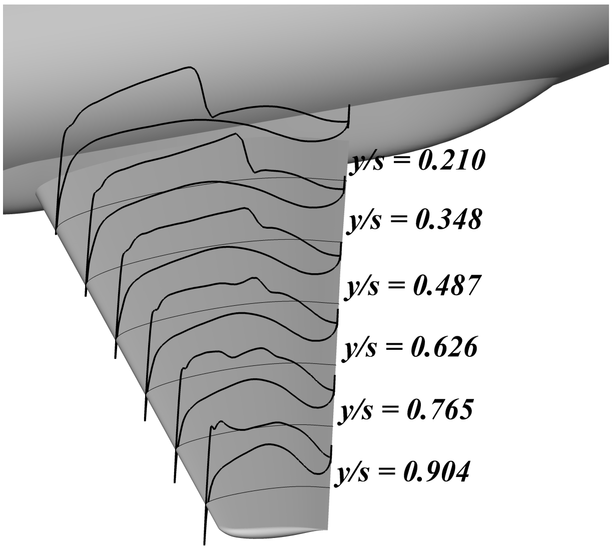

Fig. 5.2 *Pressure coefficient distribution of the WB with FSW at α=1.485°*

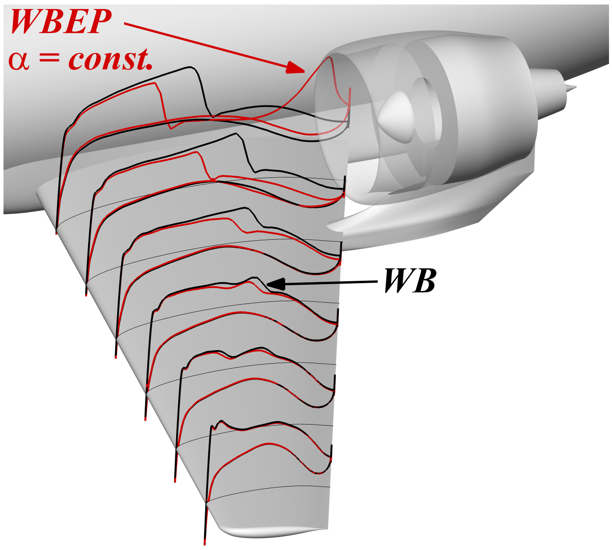

Fig. 5.3 *Comparison of pressure coefficient distributions for WB and WBEP at $\alpha = 1.485°$ for the FSW*

The general impact of the OWN on the forward swept wing will be analyzed. The WB and WBEP of REF4 at identical $\alpha = 1.485°$ will be compared, which corresponds to the necessary angle of attack of the WB configuration to achieve the target lift coefficient $C_L = 0.479$. Analogous to REF3, the qualitative pressure distributions are visualized for the WB in Fig. 5.2 and for both configurations in Fig. 5.3. The c_p-distributions were extracted at six equidistant sections between $y/s = 0.210$ and $y/s = 0.904$ and projected as hologram above the wing. These illustrations provide an overall impression of the wing aerodynamics.

Based on Fig. 5.2 the basic characteristics of the forward swept wing of REF4 in absence of the engine are visible. Based on these six sections, a typical transonic pressure distribution of a forward swept wing can be detected. As for REF3, the wing is based on the DLR-F15 airfoil [60]. First, the pressure distribution along the suction side features a strong decrease of c_p at the leading edge resulting in local supersonic flow. Along the first half of chord the gradients of c_p are small and the local pressure coefficient remains at a low level. The segment of low pressure ends with a strong gradient, especially on the inner wing, indicating the shock position. The appearance of the outer pressure distributions is comparable with a rooftop pressure distribution. Along the inner wing sections, the pressure coefficient on the upper wing features a continuous pressure decrease up to 50% chord. The pressure distribution on the lower wing is dominated by a rear loading in the aft wing section. For the inner sections, the relative chordwise shock position is located at about 50% chord. With increasing wing span, the relative shock position shifts downstream until no distinct shock could be detected for the outmost section. This behavior correlates with the three-dimensional effects of a finite forward swept wing, described in 3.2.2. The transition from supersonic to subsonic speed, especially for the inboard wing, is associated with high pressure gradients. This indicates a strong shock resulting in high drag values.

A first impression of the impact of the OWN installation at α=const. on the FSW is shown in Fig. 5.3. For reference, the c_p-distributions of the WB configuration are included as black lines, while the pressure distributions of the WBEP are colored in red. Moreover, the front engine is transparent to provide view on the rear part of the most inboard pressure section. In general, the pressure distributions for the three inner sections is almost identical along the first 50% chord length. Along the rear wing an extensive increase of c_p is noticeable, associated with an upstream shift of the shock position. Simultaneous, the section inboard of the OWN features a pronounced suction peak close to the trailing edge. This decrease of c_p is caused by a flow acceleration through the channel developed between nacelle, wing and fuselage. Outboard of the engine, the alterations between the pressure distributions of WB and WBEP diminish with increasing spanwise position. Nevertheless, around the leading edge a slight increase of c_p on the upper wing and c_p decrease on the lower wing surface indicates a decreasing effective angle of attack α_{eff} for the WBEP. Finally should be noted, that the smaller pylon of REF4, by relocating the landing gear, has minimal impact on the lower side pressure distribution. For REF3, a distinct flow acceleration was traceable close to junction of lower wing and pylon. In case of REF4, solely a slight disturbance in the c_p-distributions next to the pylon can be observed .

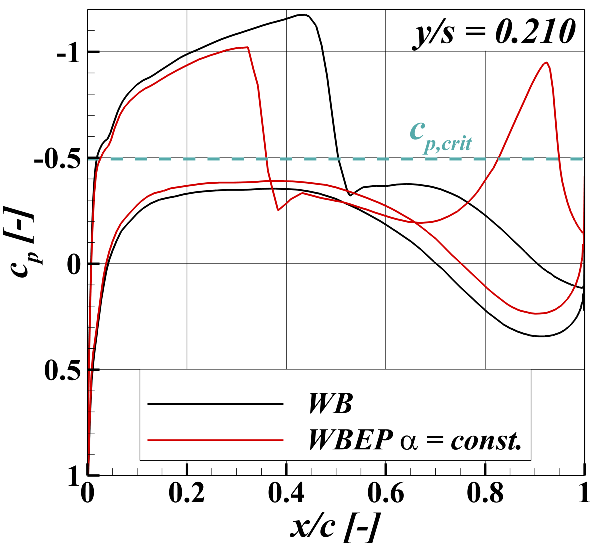

Fig. 5.4 *Pressure coefficient distribution of the WB and WBEP at* $y/s = 0.210$ ($\alpha = 1.485°$) *for the FSW*

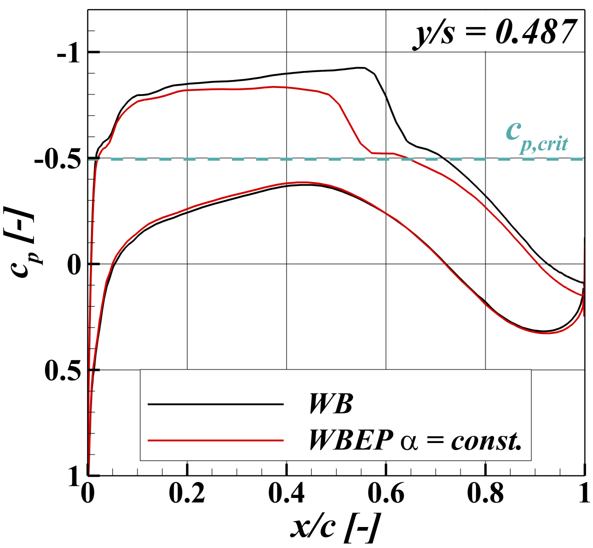

Fig. 5.5 *Pressure coefficient distribution of the WB and WBEP at* $y/s = 0.487$ ($\alpha = 1.485°$) *for the FSW*

A detailed plot of the pressure distributions at $y/s = 0.210$ and $y/s = 0.487$ comparing the WB and WBEP at constant α is shown in Fig. 5.4 and Fig. 5.5, respectively the pressure coefficient c_p is plotted reverse along the y-axis over the normalized wing chord. In addition, the critical pressure coefficient $c_{p,crit}$ is highlighted with the aid of a horizontal dashed line to identify the transition between sub- and supersonic regions. With the aid of this figure, the upstream shift of the shock location can be quantified. At $y/s = 0.210$ the displacement caused by the OWN installation totals about 15% chord, whereas the section at $y/s = 0.487$ reveals about half the displacement. In addition, the decreasing pressure difference between upper and lower wing surface, especially around the leading edge is more obvious in both sections, indicating a decreasing α_{eff}. Furthermore, the c_p-distribution at $y/s = 0.210$ reveals a pronounced pressure drop below $c_{p,crit}$ at the wing trailing edge, induced by the flow acceleration through the channel formed by nacelle, wing and fuselage. The magnitude of the rear pressure peak reaches nearly the same level as the low pressure region on the front section and is associated with a local supersonic flow.

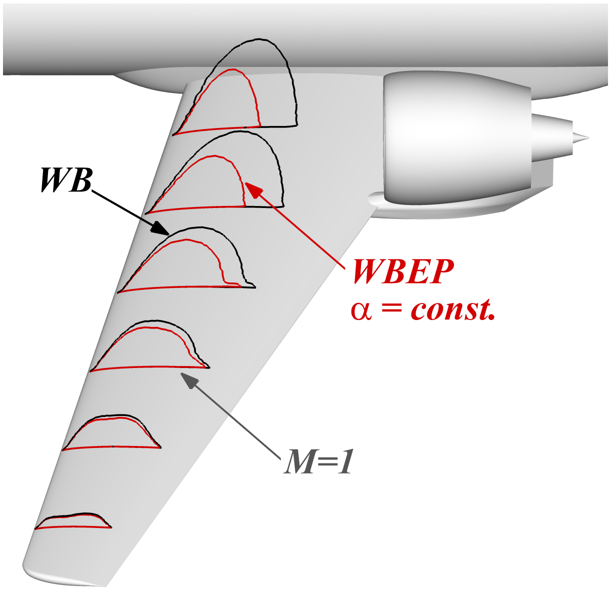

Fig. 5.6 *Regions of $M > 1$ for WB and WBEP at $\alpha = 1.485°$ for the FSW*

The evaluation of the pressure distributions has shown that a significant impact, caused by the OWN installation, can be found on the upper wing, while the pressure distributions along the lower wing are almost unaffected. To investigate in more detail the impact of the OWN installation on the transsonic features on the upper wing, Fig. 5.6 illustrates the regions of supersonic flow by iso-lines for $M = 1$. The iso-Mach lines were extracted from the volume solution analogous to the pressure distributions at the same six spanwise locations. Thus, not only the extension of supersonic flow along the wing surface, but the volumetric extent can be assessed. For comparison, both WB (black) and WBEP (red) are combined in one plot.

By means of the three inboard sections close to the OWN, the significant reduction of supersonic area and upstream shift of shock location is notable. Moreover, this visualization reveals a declining alteration between WB and WBEP with increasing spanwise distance to the engine. The two most outboard sections of the WBEP are consistent with the results of the WB for identical α. Thus can be stated, that the OWN affects mainly the inner half span of the forward swept wing. This can be addressed to the forward swept wing, which offers a maximum distance between OWN and wing tip as well as a inboard oriented crossflow. Consequently, the presence of the OWN seems to have almost no affect on the outer wing sections of REF4.

For completion, the spanwise lift distributions of WB and WBEP at identical α are presented in Fig. 5.7. The figure presents the progression of the local lift coefficient $\delta C_L/\delta(y/s)$ along the y-axis over the normalized spanwise coordinate y/s. For orientation, the engine position is highlighted by a vertical dashed line. A primary effect of the

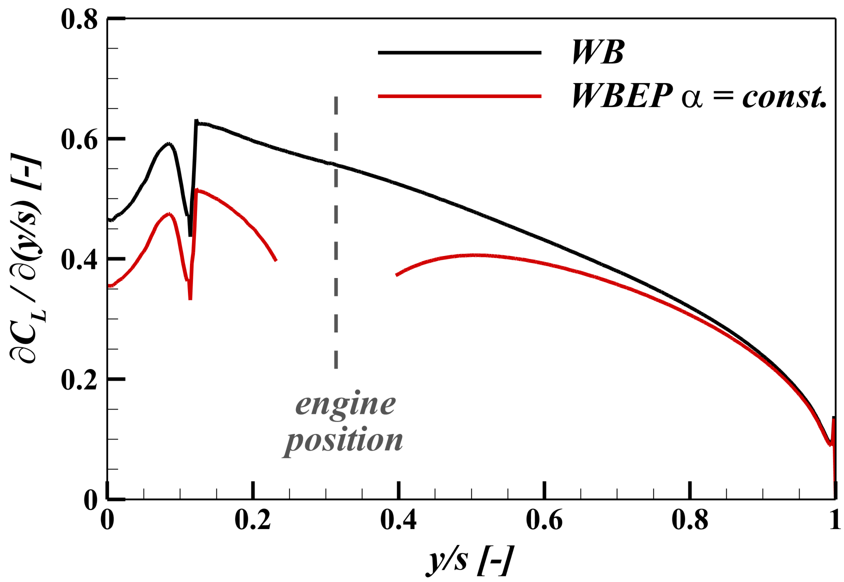

Fig. 5.7 *Spanwise lift distribution of WB and WBEP for α = 1.485° for the FSW*

OWN installation can be found over the first 50% span of the WBEP. A distinct lift drop around the engine position is obvious. Concurrently, the declining impact of the OWN on the outer wing is notable by the converging trend between WB and WBEP with increasing span. In total, the overall lift coefficient is reduced by about 20% at identical α because of the OWN installation. However, this is equivalent with half of the lift loss observed for the backward swept wing installation of REF3.

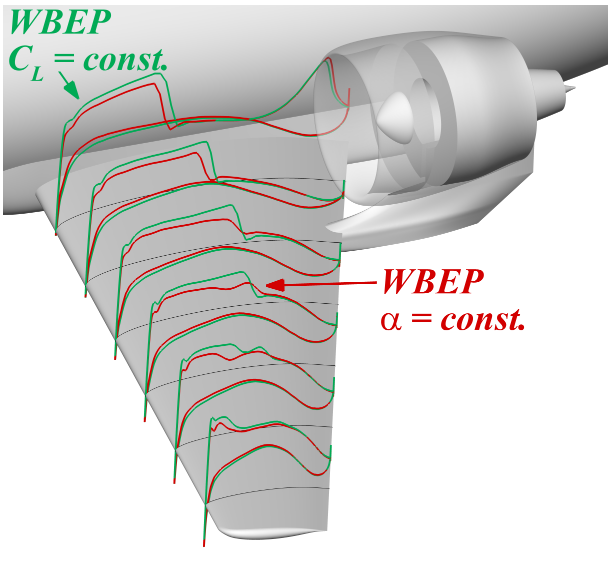

Fig. 5.8 *Comparison of pressure coefficient distributions for WBEP at C_L=const. and α=const. for the FSW*

In summary, the installation of an over-wing nacelle on a forward swept wing has a significant impact on the upper wing pressure distribution. Three main effects can be observed:

1. OWN has a dominant impact on the inner half of the upper wing;

2. Pressure level on rear wing in front of the engine increases;
3. Distinct flow acceleration caused by a channel between nacelle, wing and fuselage.

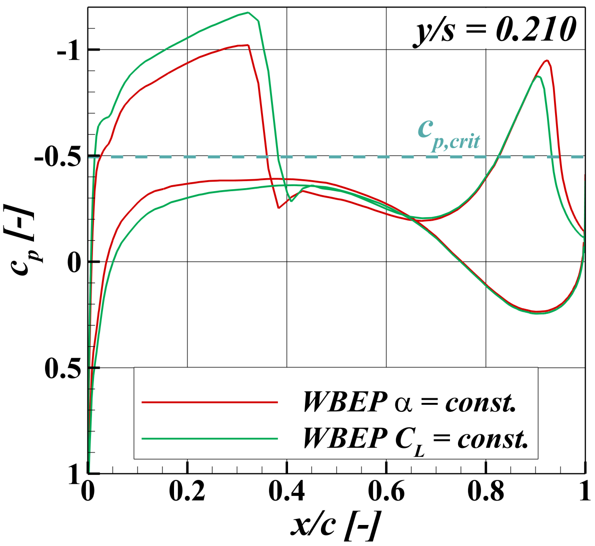

Fig. 5.9 *Pressure coefficient distribution comparing the WBEP for α=const. and target C_L (y/s = 0.210) for the FSW*

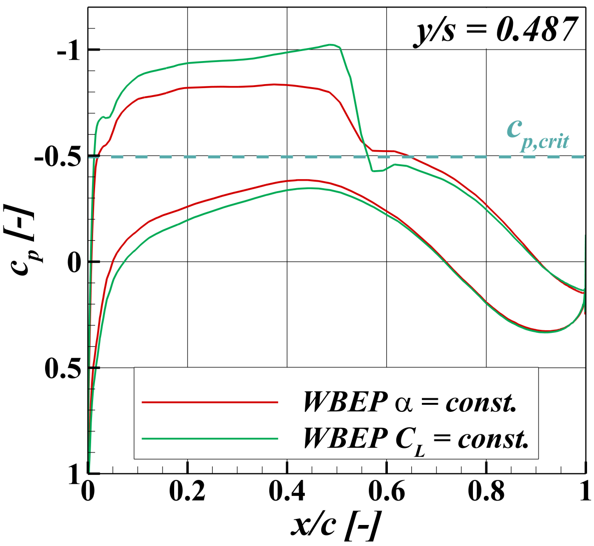

Fig. 5.10 *Pressure coefficient distribution comparing the WBEP for α=const. and target C_L (y/s = 0.487) for the FSW*

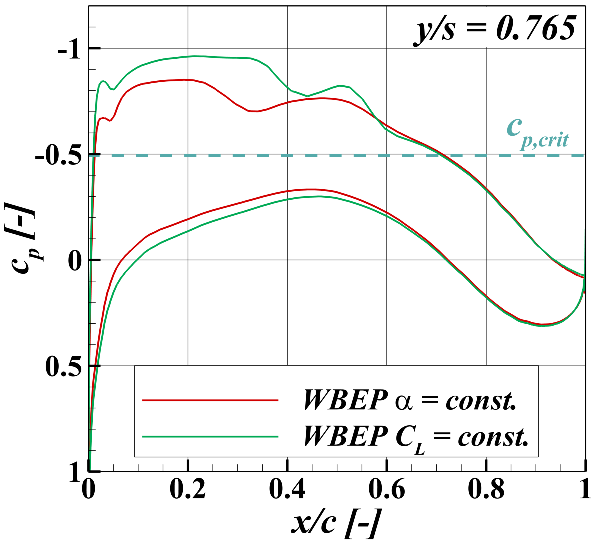

Fig. 5.11 *Pressure coefficient distribution comparing the WBEP for α=const. and target C_L (y/s = 0.765) for the FSW*

Subsequently, the interference and balance between OWN and FSW is investigated by comparing the WBEP configuration at target α and target lift coefficient. Therefore, the angle of attack α was increased by 0.76° starting from the WBEP at α=1.485° to achieve the target lift of C_L=0.479. As starting point, qualitative pressure distributions for both configurations are presented in Fig. 5.8.

The c_p-distributions are plotted again as hologram above the wing. The red distributions reflect the known results from Fig. 5.3 for the WBEP at target α, extended by the outcome of the WBEP at target lift represented by green lines. This visual comparison exposes an increasing pressure difference between wing upper and lower surface for all sections resulting from the increasing incidence angle. Especially, within the front half of the wing upper surface, a distinct decrease of c_p can be observed for the results of C_L=const.. Moreover, the negative pressure gradient extends for the two inboard sections further downstream. The pressure distributions along the rear wing exhibit almost no alteration. Nevertheless, the flow acceleration inboard of the engine slightly decreases. A detailed assessment of the changes in the outer sections on the basis of this qualitative plot is not possible. Thus, exemplary pressure distributions are presented in Fig. 5.9 to Fig. 5.11.

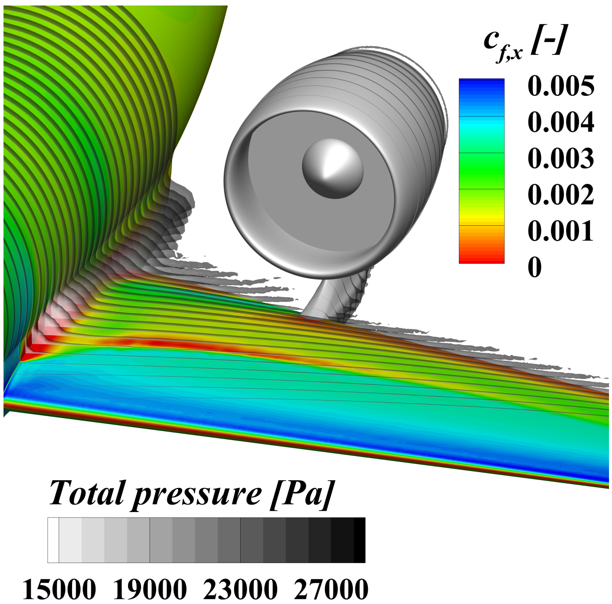

Fig. 5.12 *Visualization of corner flow separation using $c_{f,x}$ on the surface contour and total pressure losses along spanwise volume slices for the FSW at C_L=const.*

The c_p-distribution for y/s = 0.210, shown in Fig. 5.9 reveals the expected behavior due to the increasing angle of attack α. The low pressure region along the upper surface extends and simultaneous the c_p level along the lower wing surface increases. However, the rear suction peak decreases. The reason for this behavior is found by evaluating regions of separated flow. In 3.2.2, the challenges related to the wing/fuselage junction and risk of flow separations in association with forward swept wings were already discussed. An evaluation of the junction flow of the WBEP at target C_L, outlined in Fig. 5.12, reveals a corner flow separation. The surface contour is colored by the skin friction coefficient $c_{f,x}$. Red areas ($c_{f,x} \leq 0$) indicating local flow separations. The flow separation originates from the increased shock strength, induced by sudden pressure drop of Δc_p ≈0.9 in combination with the isobar concentration towards the wing leading edge in the wing/fuselage junction. As a consequence of this local flow separation at about 40% chord, the mass flow approaching the channel between nacelle, fuselage and wing at about 80% chord is diminished due to total pressure losses, highlighted by the gray-colored spanwise volume slices, and thus the corresponding flow acceleration decreases.

Fig. 5.10 presents the c_p-distribution at y/s = 0.487. The pressure distribution for the WBEP at target C_L features a sharp increase in c_p as well, concluding an extended low pressure region. Although, the increasing shock strength causes no flow separation outboard of the engine, the boundary layer flow will be highly loaded and an increased wave drag component can be assumed. As to be expected, the smaller incidence of WBEP at α=const. is associated with a smaller shock strength and thus smoother transition from supersonic to subsonic flow.

The surface pressure distributions in Fig. 5.11 representing the section at y/s = 0.765 are both characterized by a smooth transition from supersonic to subsonic speed at $x/c \approx 0.7$. Moreover, the increasing pressure difference between lower and upper wing surface, caused by the increased incidence to reach target C_L, is as expected.

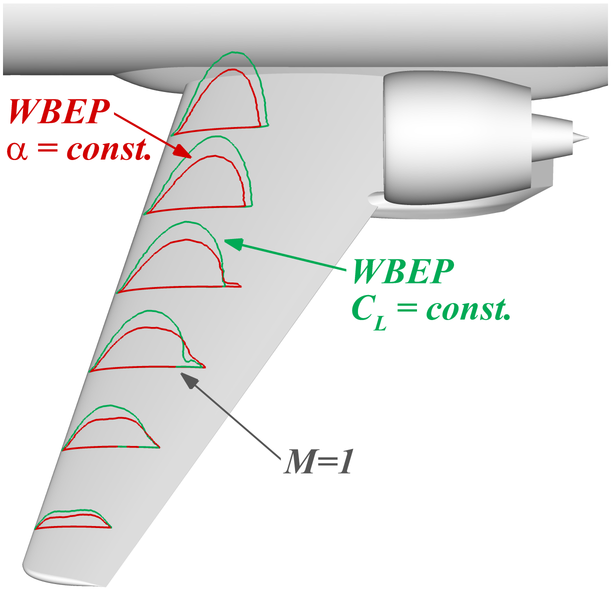

Fig. 5.13 *Regions of M>1 for WBEP at α=const. and C_L=const. for the FSW*

The displacement of the shock locations and extension of local supersonic flow is evaluated by visualizing the iso-Mach lines for $M = 1$ in all six sections along the wing is shown in Fig. 5.13. Based on the comparison for WBEP at α=const. and C_L=const. an extended area of supersonic flow can be observed for all six sections. However, the shock position for the four outer sections is almost unaltered despite the increasing α, whereas a downstream shift of the shock location with increasing incidence is present for the two inboard sections, in front of the engine. This behavior on the forward swept wing of REF4 is opposite to the observations on REF3. There, a downstream movement of the shock position for the outer sections is observable with increasing incidence and the inner shock position is fixed.

Subsequently, the surface pressure difference of the WBEP REF4 between α=const. and C_L=const. is illustrated in Fig. 5.14. The results for C_L=const. were subtracted from the flow solution at α=const.. In this plot, red indicates a pressure increase from WBEP at α=const. to WBEP at C_L=const., while blue represents a decrease of c_p. Light colored areas indicate regions with almost no static pressure deviation. Based on the blue

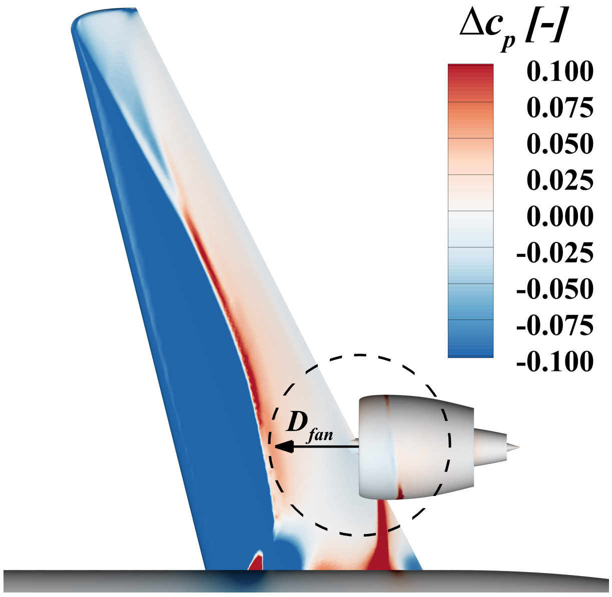

Fig. 5.14 *Pressure difference between WBEP at C_L=const. and α=const. for the FSW*

colored areas along the front wing section, the pressure decrease due to the increasing α can be identified. Whereas red colored regions, representing an increasing pressure coefficient, can be discovered at the mid wing shock position and in the channel between nacelle, wing and fuselage. As already observed for the REF3, there is an area in front of the engine featuring almost no pressure change despite the increasing incidence. The upstream extend in the engine symmetry plane equals about the size of the engine fan diameter. This was also found for the REF3. The light colored area ranges along the wing trailing edge from the engine up to the wing tip. On the mid wing section, a red strip is notable, indicating the increasing shock strength, which was already observed in the pressure section at $y/s = 0.487$. By focusing on the wing/fuselage junction, a small red spot can be identified in the first quarter of the wing chord, followed by a region of negative Δc_p. This spot highlights the origin of the local flow separation, whose flow displacement afterwards affects the mass flow through the channel between nacelle, wing and fuselage. Based on this evaluation, it can be assumed that the OWN affects a delimited area in front of the engine inlet. The shock location is shifted significantly upstream due to the OWN installation, and the characteristic of a forward swept wing in the wing/fuselage junction amplifies the displacement inboards. By increasing the angle of attack, the shock is shifted back downstream. However, the adverse pressure gradient induced by the engine inlet suspends the displacement as soon as the shock reaches the area governed by the OWN. In case of REF4, the airfoil section outboard of the engine benefits from the increased distance to the OWN because of the forward sweep. Thus, this area is less affected as observed for REF3. Nevertheless, the OWN has an influence on the forward swept outer wing due to the information propagation between the upstream located wing tip and the inboard trailing edge. Consequently, the presence of the OWN can affect the subsonic region of the outer wing sections of REF4, but not the area of supersonic flow, since information are only propagating in both directions for $M < 1$. A simulation at higher angle of attack, which is not additionally presented, confirmed, that the downstream movement of the shock stops at the same distance to the engine inlet plane as observed for REF3.

5.2 Impact of OWN engine installation on drag coefficient

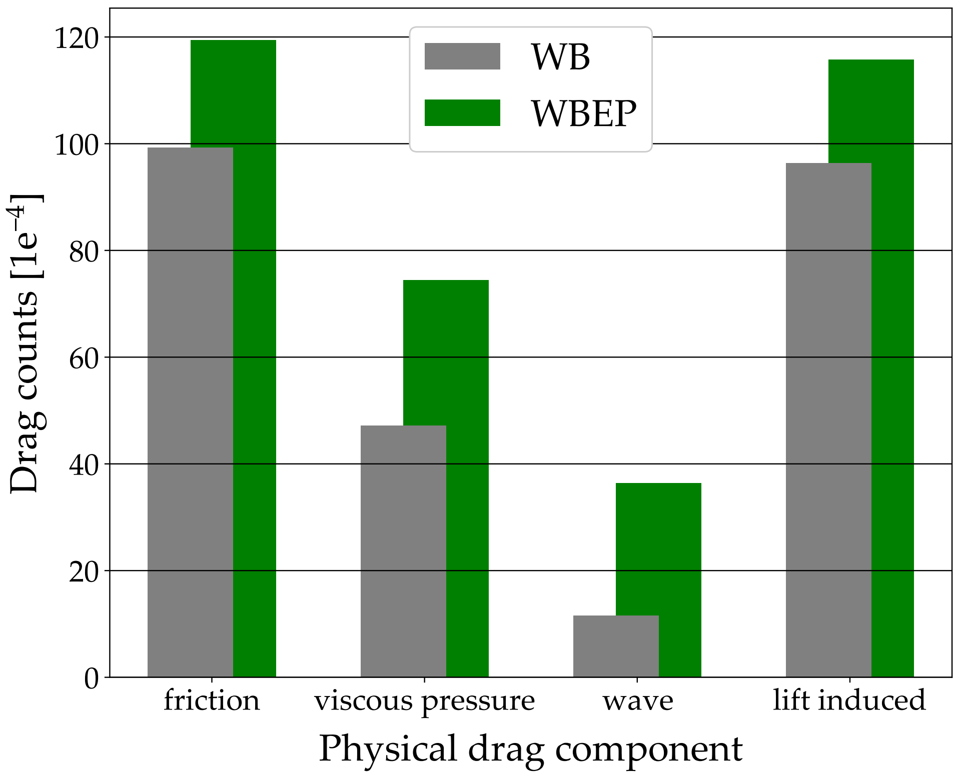

Fig. 5.15 *Drag components of WB and WBEP for the FSW*

The following section focuses on the drag breakdown of WB and WBEP at target C_L to assess the influence of the OWN installation on the drag coefficient in case of the forward swept wing configuration. The physical drag components was evaluated with the aid of the farfield drag evaluation tool. The diagram in Fig. 5.15 compares the drag components of the WB and WBEP configuration for C_L=const.. The bar diagram consists of four categories, which represent the physical drag breakdown provided by the far-field drag analysis. The bars are overlapping for a simple comparison between WB (gray) and WBEP (green). Based on this figure, an increase in each individual drag component due to the engine integration can be observed. However, the raise of wave and viscous pressure drag needs to be emphasized due to the large relative increase. Resulting from the OWN installation, both coefficients double in comparison with the WB configuration. The wave drag increase of 25 dcts. can be ascribed to two sources. On the one hand, the OWN installation creates a channel between nacelle, wing and fuselage, which induces a flow acceleration to $M > 1$, as already presented in 5.1.

A visualization of iso-Mach surfaces, colored in orange, at local $M = 1.2$ for WB and WBEP at target C_L is given in Fig. 5.16. On the left, the WB at $\alpha = 1.49°$ is compared with the flow solution of the WBEP at $\alpha = 2.25°$ on the right. Thus, the area of supersonic flow is traceable around the nacelle leading edge including a distinct expansion on the inboard facing nacelle surface. Thus can be stated, that part of the additional wave drag originates from the supersonic flow around the nacelle. By comparison of the iso-surfaces along the wings of WB and WBEP, the impact of the increasing angle of attack α is traceable. The extension of high pre-shock Mach numbers indicates the

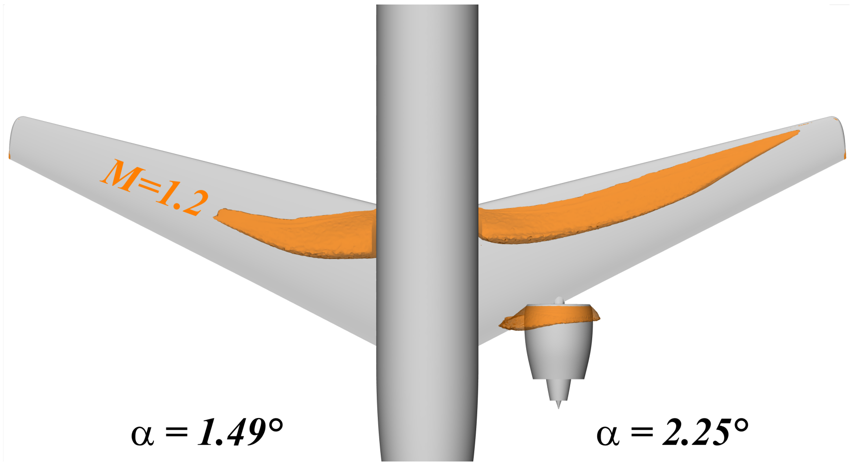

Fig. 5.16 *Iso-Mach surface at M=1.2 for WB and WBEP at target C_L on the FSW*

second source of the increasing wave drag. As shown in the previous section, the increase of α resulted in an decreasing pressure coefficient in the region of supersonic flow. This is associated with an increasing Mach number and larger pressure jumps across the shock. By comparison of the iso-Mach surface in Fig. 5.16 the increase of Mach number, especially outboard of the nacelle, is apparent. Thus, the higher Mach number on the wing of the WBEP can be identified as additional source of the significant wave drag increase.

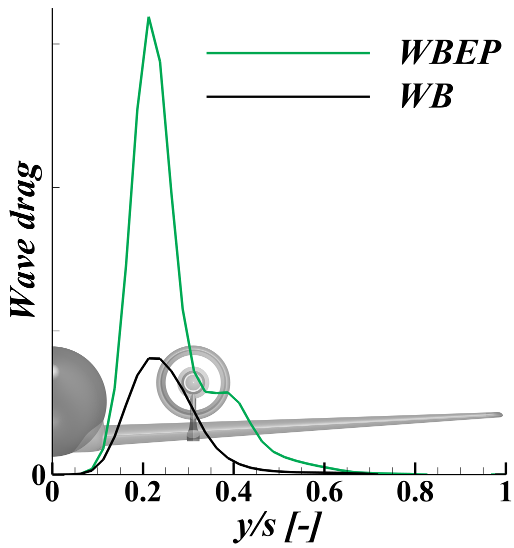

Fig. 5.17 *Spanwise distribution of wave drag for WB and WBEP at target C_L for the FSW*

To confirm this assumption, the spanwise plots of the wave drag component provided by far-field drag analysis were evaluated. Fig. 5.17 compares the spanwise distribution of the wave drag for WB and WBEP. The quantity of generated wave drag is plotted along the wing span. For orientation, the geometry of REF4 is plotted from rear view in the background. The results for the WB configuration are colored in black, while the outcome of the WBEP evaluation is plotted in green. For the WB configuration, wave drag occurs mainly along the inner wing section between $y/s = 0.140$ and $y/s = 0.417$. This correlates with the iso-Mach surface in Fig. 5.16. Resulting from the OWN installation, an increasing wave drag occurs around the engine position including a significant peak inboard of the engine. In addition, a raise in wave drag outboard of the engine can be noted. This is probably caused by the increased shock strength induced by the higher α. Consequently, it can be stated that the flow acceleration through the channel between nacelle, wing and fuselage is the main reason for the wave drag increase.

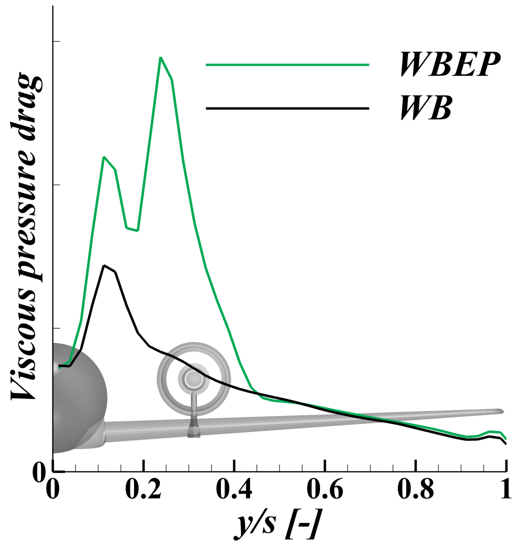

Fig. 5.18 *Spanwise distribution of viscous pressure drag for WB and WBEP at target C_L for the FSW*

Following, the origin of the increasing viscous pressure drag is evaluated. Analogous to Fig. 5.17, the spanwise progression of the viscous pressure drag is presented based on the far-field drag analysis in Fig. 5.18. Thus, the quantity of generated viscous pressure drag is plotted along the wing span. For orientation, the geometry of REF4 is plotted from rear view in the background. The results for the WB configuration are colored in black, while the outcome of the WBEP evaluation is plotted in green. Starting with the WB configuration, the highest values of viscous pressure drag can be found around the fuselage. On the one hand, the flow displacement and boundary layer thickness due to the fuselage length causes high viscous pressure losses. On the other hand, the problematic region of the forward swept wing is again obvious. The wing/fuselage junction of REF4 implicates an upstream shift and amplification of the shock in comparison to a backward swept wing. In case of the WB configuration, the flow is still attached, however the disturbance on the front airfoil section results in an early weakening and thickening of the boundary layer. As a consequence, the viscous pressure drag of the WB features a global maximum in the wing/fuselage junction. Comparing, the spanwise distributions of WB and WBEP, the change induced by the OWN is limited to a section between fuselage and outer nacelle edge. In case of the WBEP, the peak in viscous pressure at the wing/fuselage junction is still present and even further increased. This can be assigned to the occurrence of flow separations. In addition, a new global maximum can be observed at the spanwise location of the nacelle with an emphasis on the inboard engine. The flow displacement by the UHBR nacelle in combination with areas of supersonic flow results in an additional loading of the boundary layer and local flow separations. These effects cause a significant increase in viscous pressure drag for the WBEP and will be discussed in more detail in the following chapter.

The increasing friction drag can be assigned to the increased wetted area and the increase in induced drag originates from the disturbance of the spanwise lift distribution by the OWN. A comparison between WBE and WBEP configuration reveals a minor impact of the pylon installation. The overall drag increases by about 8 dcts., while the predominant change relates to pressure induced drag components. Thus, REF4 benefits from the modified landing gear mounting and the associated smaller pylon fairing in comparison with REF3.

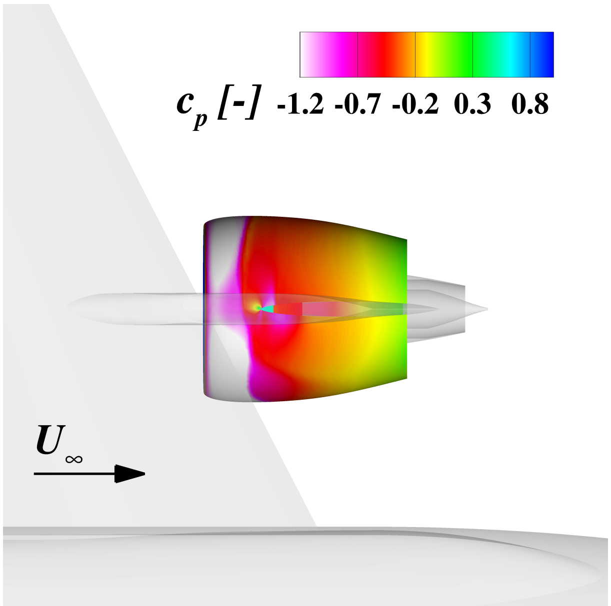

Fig. 5.19 *Bottom view on nacelle/pylon/wing junction of the FSW*

Furthermore, the view from the bottom on the junction between pylon and nacelle in Fig. 5.19 reveals a disturbance of the low pressure region at the nacelle leading edge. This low pressure region on the forward facing surface is beneficial with respect to drag, because the resulting force is facing in direction of flight. However, the investigation of this beneficial interference effect on the nacelle leading is not part of this thesis. A detailed investigation of this phenomena and a derived explanation on the basis of a generic test case by Lange and Kotzem can be found in [65].

5.3 Interference effects on FSW caused by OWN position variation

Subsequent to the description of general effects caused by OWN installation on a forward swept wing, a parameter study concerning the horizontal and vertical distance between engine and wing trailing edge was performed with the aid of a surrogate-based optimization tool. Therefore, the wing trailing edge at $y/s = 0.314$ and the nacelle highlight at 6 o'clock position were defined as reference points, analogous to REF3.

In case of REF4, the parameter space in horizontal direction ranges between -10% to +10% chord around the wing trailing edge. The vertical distance was investigated from 10% up to 20% chord above the wing trailing edge. This parameter space is larger than for REF3 due to a more flexible pylon design, which was constrained by the landing gear housing of REF3. Consequential, a sanity check of the results for REF3 can be accomplished and transferability on an extended parameter space. The evaluation is based on sample points, which were determined at identical target lift for each individual parameter variation. Furthermore, the convergence of the RANS simulation was assured by applying a Cauchy convergence criterion for the drag coefficient. This criterion accepts a drag oscillation of less than 0.1 dcts. in 2000 iteration, which corresponds to approximately one-third of the total number of iterations. It should be noted that the following evaluation focuses on the impact of the OWN on the aerodynamic characteristics of the wing.

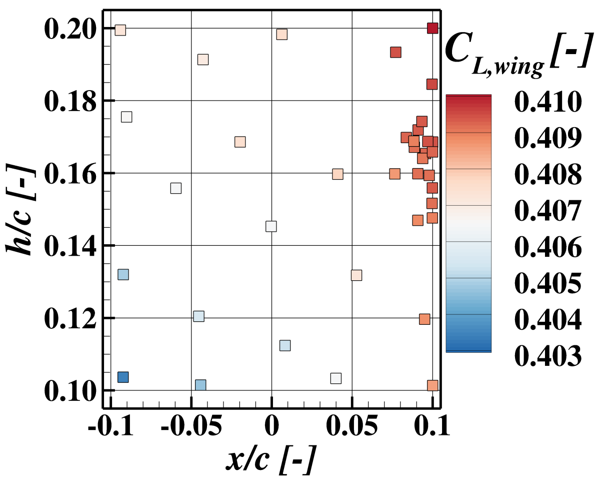

Fig. 5.20 *Componentwise lift coefficient $C_{L,wing}$ of FSW in the presence of the OWN*

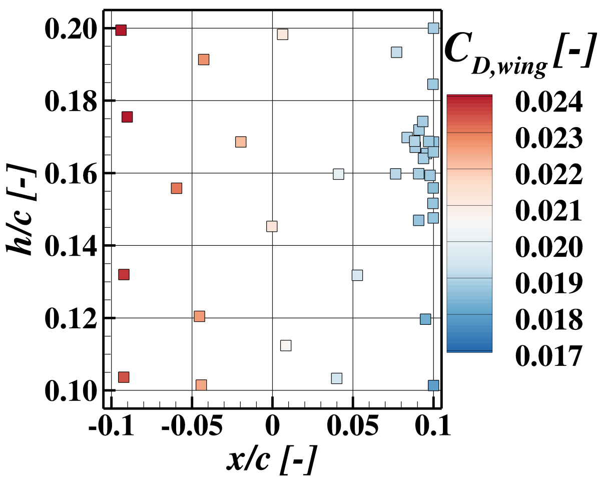

Fig. 5.21 *Componentwise drag coefficient $C_{D,wing}$ of FSW in the presence of the OWN*

A first overview of the collected data is plotted in Fig. 5.20 and Fig. 5.21. These figures illustrate the behavior of the wing's lift $C_{L,wing}$ and drag $C_{D,wing}$ coefficients within the investigated parameter space. The vertical distance h/c is plotted over the horizontal distance x/c. Negative values for x/c are indicating an overlap of nacelle highlight and wing trailing edge. Each colored square corresponds to an investigated sample point, while the coloring reflects the contour value. The componentwise lift coefficient $C_{L,wing}$ in Fig. 5.20 varies by 0.7 lcts. within the parameter space. The lowest lift coefficients can be found for the largest overlap and smallest vertical distance between nacelle and wing. The highest $C_{L,wing}$ is present for the most downstream position and largest vertical distance. Thus can be stated, that a close coupling of OWN and wing results in lift decrease on the wing component, which needs to be compensated by the remaining aircraft components to reach the same overall lift coefficient. The changes of $C_{L,wing}$ in between the maximum and minimum positions in horizontal and vertical direction are in the same order of magnitude, but the covered horizontal distance is twice as large as the vertical distance. Thus, the vertical distance is the dominant parameter with respect to the componentwise lift coefficient $C_{L,wing}$.

The variation of $C_{D,wing}$ in Fig. 5.21 unveils a decisive trend dependent on the engine position. The wing drag component is minimal for the most downstream engine position at x/c=0.1. There, most of the sample points ware placed by the optimizer. By shifting the engine upstream, $C_{D,wing}$ increases significantly. The difference between the two extreme points at $h/c \approx 0.2$ totals 55 dcts.. The variation of the vertical distances reveals a minor impact on $C_{D,wing}$.

Following, a detailed analysis of the driving mechanisms will be accomplished on the basis of three selected samples. First, the impact on the lift component will be evaluated on the diagonal from the strongest coupled configuration at $x/c \approx -0.09$ and $h/c \approx 0.1$ over the sample at $x/c \approx 0$ and $h/c \approx 0.145$ to the most far off located nacelle position at $x/c \approx 0.1$ and $h/c \approx 0.2$. As starting point, an impression of the pressure coefficient c_p over a volume slice in the engine's symmetry plane of each sample is provided in Fig. 5.22 to Fig. 5.24. For orientation, the slice is transparent and the critical pressure coefficient $c_{p,crit}$, representing $M = 1$, is marked by a black solid line to indicate the area of supersonic flow. The contour level ranges from -1 to $+1$, while blue indicates a c_p close to -1, and red colors represents pressure levels around $+1$. Fig. 5.22 to Fig. 5.24 display from left to right a simultaneous increase of vertical and horizontal distance.

Based on these illustrations, an interaction between engine position and area of supersonic flow on wing and nacelle can be noticed. By moving the engine towards the most far off position, the boundary for $M = 1$ extends for the wing. Concurrently, the area of supersonic flow at the upper nacelle leading edge decreases. The observed change on the engine correlates with the required angle of attach α to achieve target C_L. The incidence changes from 2.50° at x/c=-0.09 and h/c=0.10 to 2.07° at $x/c = 0.1$ and h/c=0.2.

For a direct comparison, the isolated iso-Mach lines are brought together in Fig. 5.25. The plot presents a superposition of the volume slices through the engine symmetry plane. As a consequence, the dark gray area represents a cross section through wing, engine and pylon. For traceability, the dashed line, highlighting the iso-Mach lines for $M = 1$, and the outer edges of the nacelle, showing the geometrical variation, are harmonized. Furthermore, the regions of supersonic flow are exemplary highlighted white for the configuration with $hx/c = 0.1$ and $h/c = 0.2$. The legend provides additionally the necessary angle of attack α to achieve target C_L.

Based on Fig. 5.25, an explicit correlation between engine position and area of supersonic flow can be observed. The shock position complies with the engine displacement. Attention should be paid to the fact, that the area of supersonic flow increases and the shock location moves downstream even though the angle of attach decreases. Nevertheless, the nacelle displacement is larger than the shock relocation. Despite a constant step interval between the three engine locations, the correlating distance in between the shock locations is decreasing for the most far off engine position. A potential explanation is the limitation by the underlying wing. To follow up this assumption, a comparison of the pressure distributions in this particular section is provided by Fig. 5.26.

This figure presents the pressure coefficient c_p plotted reverse along the y-axis over the normalized chord x/c. The line color scheme corresponds to Fig. 5.25. The surface pressure coefficients were extracted at $y/s = 0.314$. In addition, the wing shock position

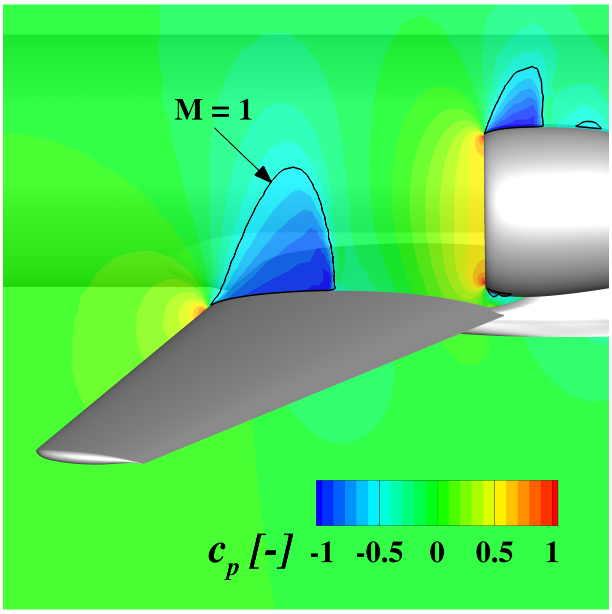

Fig. 5.22 *Volume slice showing the pressure coefficient at y/s=0.314 (engine position: x/c=-0.09; h/c=0.10) for the FSW*

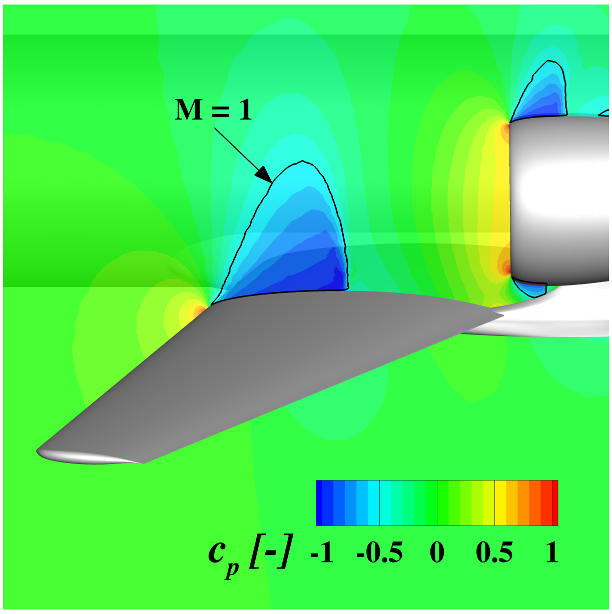

Fig. 5.23 *Volume slice showing the pressure coefficient at y/s=0.314 (engine position: x/c=0.00; h/c=0.145) for the FSW*

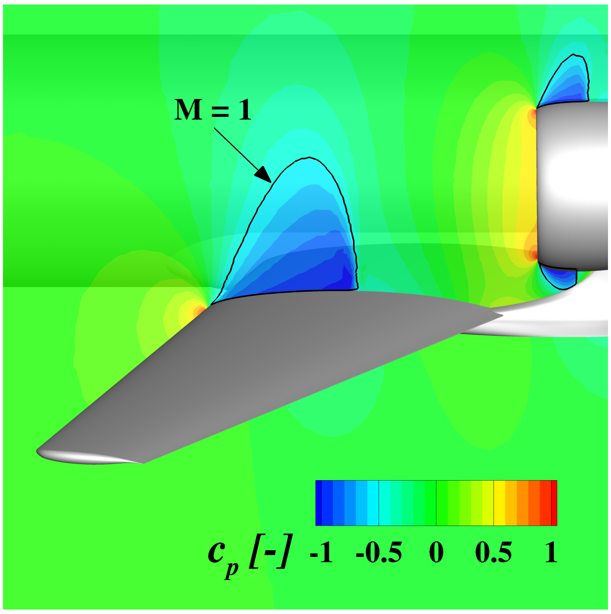

Fig. 5.24 *Volume slice showing the pressure coefficient at y/s=0.314 (engine position: x/c=0.10; h/c=0.20) for the FSW*

for the REF4-WB configuration is highlighted by a vertical dashed line, located at x/c=58%. The three pressure distributions differ most on the upper side from the shock down to the trailing edge. The progression of c_p on the lower wing up the pylon at $x/c \approx 0.65$ and along the front upper side is characterized my small deviations. The observations based on the region of supersonic flow are confirmed by the downward shift of the steep pressure gradient indicating the shock position. For the most aft engine

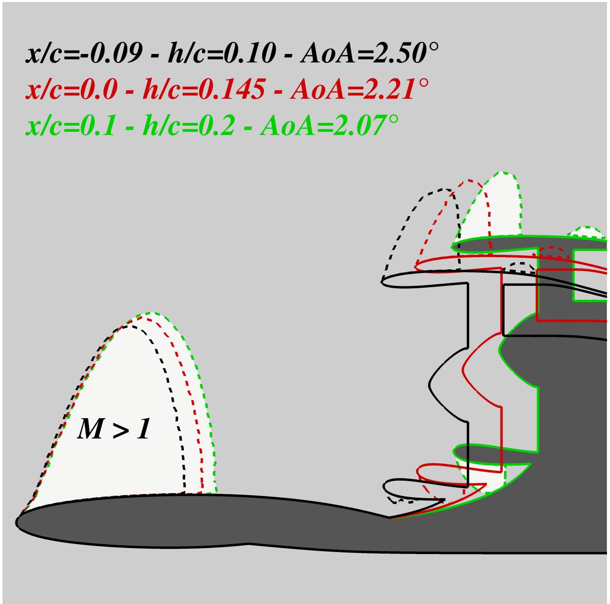

Fig. 5.25 *Comparison of the iso-Mach lines for varying engine positions on the FSW*

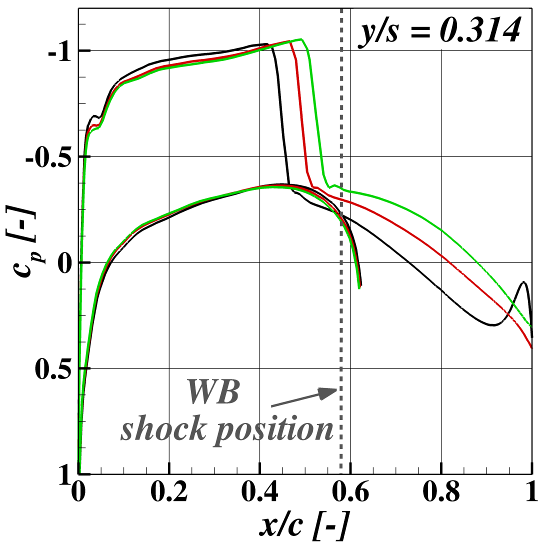

Fig. 5.26 *Comparison of the pressure distributions for x/c=-0.09 / h/c=0.1 (black), x/c=0.0 / h/c=0.145 (red) and x/c=0.1 / h/c=0.2 (green) on the FSW*

position (green) the shock is located at $x/c = 0.55$, close to the isolated wing shock location. This could explain the decreasing step size in downstream direction despite a larger engine displacement. Thus, the shock relocation is not only influenced by the engine induced reverse pressure gradient but is also limited by the airfoil.

Moreover, the increasing wing lift component $C_{L,wing}$ can be understood on the basis of the pressure distributions. On the one hand, the area of low pressure along the upper wing surface increases due to the shock displacement caused by the horizontal engine displacement. On the other hand, c_p decreases on the rear wing due a declining presence of the engine, which is further amplified by the engine's relocation in vertical direction. The wing lower surface is nearly unaffected by the engine position variation. Resulting, the lift contribution of the inner wing section increases, despite an decreasing angle of attack.

The following focuses on the behavior of the drag coefficient $C_{D,wing}$, observed in Fig. 5.21. The evaluation revealed a dominant impact of the horizontal engine position. Consequently, three samples close to $h/c = 0.2$ were selected for this evaluation. The extracted sample points are marked by solid circles in Fig. 5.27. Besides the samples for the drag evaluation, the data points for the previous $C_{L,wing}$ investigation are highlighted by dashed circles. The chosen horizontal positions x/c are almost identical for both investigations. However, the vertical position h/c are different for two of three points. Thus, a comparison between these five samples enables an additional separation of the impact caused by the vertical and horizontal distance of the OWN on the wing aerodynamic.

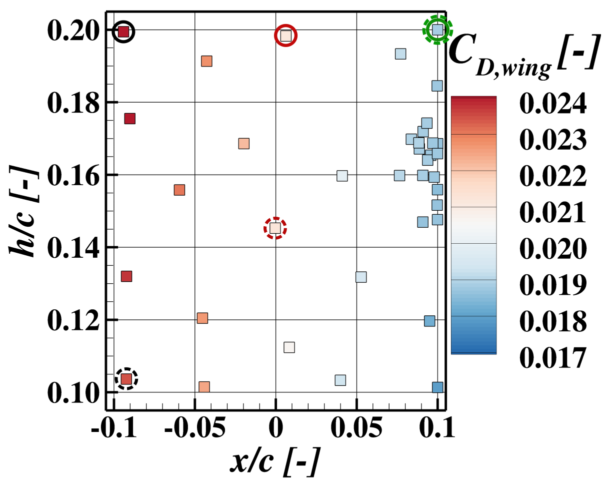

Fig. 5.27 *Componentwise drag coefficient $C_{D,wing}$ of FSW in the presence of the OWN including marked sample points*

Fig. 5.28 is an extension of Fig. 5.26, which compares the pressure distributions of all five samples. The dashed lines are representing the engine position at the same h/c-level. The solid pressure distributions display the sample points on varying vertical positions, which are already known from the $C_{L,wing}$ evaluation. Same colors imply similar horizontal engine positions. The plot reveals approximately identical shock locations on the wing for similar horizontal engine positions. The vertical distance has almost no impact on the supersonic low pressure region along the front airfoil. Based on this observation, it can be derived that the dominant impact on the shock location is the horizontal engine position. Nevertheless, a distinct change of c_p on the rear wing can be observed. The solid line of the C_L-variation correspond to smaller vertical distances between OWN and wing. As a consequence, the presence of the OWN is pronounced by higher c_p-values on the rear wing despite a similar horizontal distance. Concluding from this observation, it can be stated that the vertical engine position affects solely the subsonic region on the rear wing.

Since, the horizontal engine position was identified as main factor of influence regarding the wing shock location, the behavior of the chordwise shock location with respect to

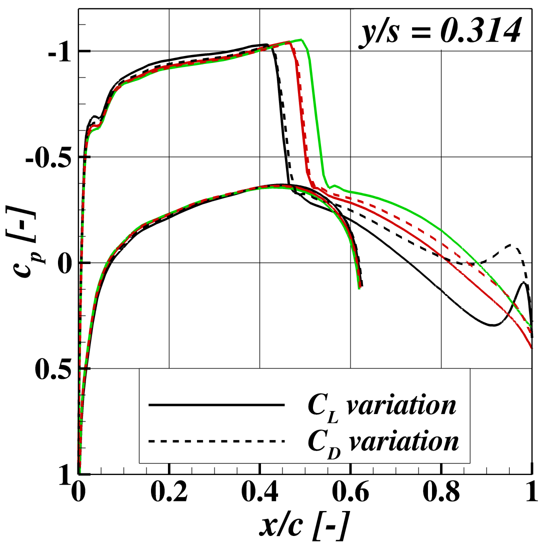

Fig. 5.28 *Comparison of the pressure distributions for x/c=-0.09 (black), x/c=0.0 (red) and x/c=0.1 (green) on the FSW*

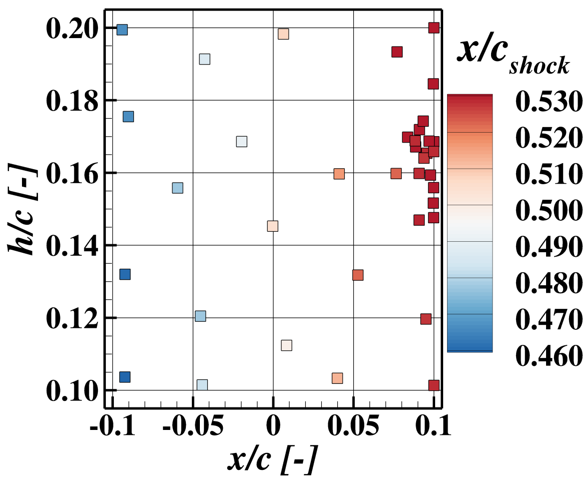

Fig. 5.29 *Chordwise shock location x/c_{shock} at engine symmetry plane on FSW*

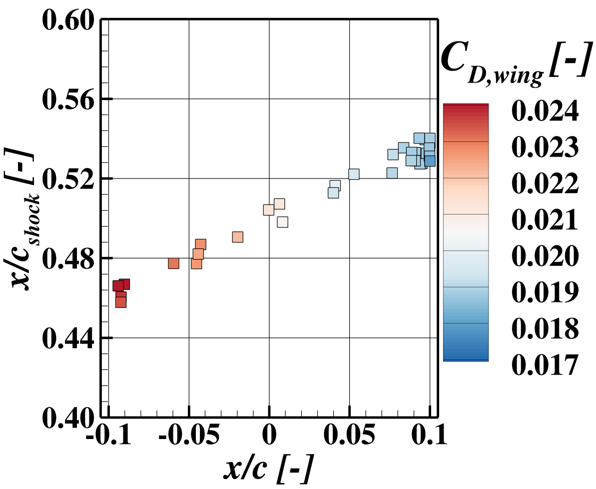

Fig. 5.30 *Chordwise shock location at engine symmetry plane on FSW dependent on x/c*

the whole investigated parameter space is plotted in Fig. 5.29. The vertical distance h/c is plotted on the y-axis over the horizontal distance x/c. The symbols coloring indicates the chordwise shock location between 46% and 54% chord. The overall trend within this plot confirms the horizontal distance as the dominant driver for the shock position. Thus, the chordwise shock location is plotted in dependence of the horizontal engine position in Fig. 5.30. Additionally, the symbols are colored with respect to the wing drag contribution. A linear correlation between horizontal engine position x/c and wing shock location x/c_{shock} in front of the engine is observable. An engine position variation

Tab. 5.1 *Physical drag breakdown of three different horizontal engine positions at $h/c \approx 0.2$ for the FSW*

		Horizontal position x/c		
		-0.095	*0.01*	*0.10*
Drag components	*friction drag*	120.8	122.5	122.6
	vis. pressure drag	120.5	72.5	64.2
	wave drag	40.1	35.8	27.1
	induced drag	114.0	112.5	107.7
	Total drag	395.4	343.3	321.6

of $\Delta x/c$=0.1 is accompanied by $\Delta x/c_{shock}$ of approximately 0.4. Furthermore, it should be noted that the necessary angle of attack α for target C_L decreases linear by about 0.27° in correlation with an engine displacement of 10% chord in downstream direction. Thus, an expected upstream shift of the shock location caused by the decreasing α narrows the shock relocation induced by the engine displacement. Furthermore, the presumed influence of the airfoil limitations on the shock relocation, can not be confirmed with certainty. A conclusive flattening of the linear gradient for the most aft engine position is not proven by the present data. Nevertheless, a clear correlation between the drag coefficient of the wing $C_{D,wing}$ and engine position or the according chordwise shock location is seen in Fig. 5.30. But no reason for the significant drag variation accompanied by the engine position was identified yet. Thus, an analysis of physical drag components was performed for the three sample points with similar vertical engine positions. The physical drag breakdown is listed in Tab. 5.1.

The most significant drag variation can be found for the viscous pressure component. By shifting the engine downstream, this drag component almost halves between $x/c \approx -0.095$ and 0.1. The engine position at $x/c \approx 0.01$ implies a viscous pressure drag reduction of 48 dcts. in comparison with the results for the overlapping engine position at $x/c \approx -0.1$. A further downstream placement results in an additional viscous pressure drag decrease of about 8 dcts.. Thus it can be assumed that the overlap of OWN and wing results in a distinct viscous pressure increase. An increasing drag component with increasing overlap can also be found for the wave drag. However, the variation in this drag component is characterized by a small step of about 4 dcts, between the most upstream and mid engine position, whereas a further downstream placement at $x/c \approx 0.1$ results in a decrease of about 9 dcts.. Thus, it can be assumed that a significant wave drag reduction can only be achieved by locating the engine highlight downstream of the trailing edge of the forward swept wing. The friction drag varies only slightly over the different engine positions. Finally, a decreasing drag component for the downstream shift of the engine can be observed for the induced drag component. The variation totals 6 dcts. whereas the largest gain can be found between $x/c \approx 0.01$ and 0.1. This can be explained by the declining impact of the OWN for the most aft position on the spanwise lift distribution of the wing. Concluding, by shifting the engine further downstream, all drag components are decreasing except for the friction drag, which increases slightly due to the increasing pylon geometry.

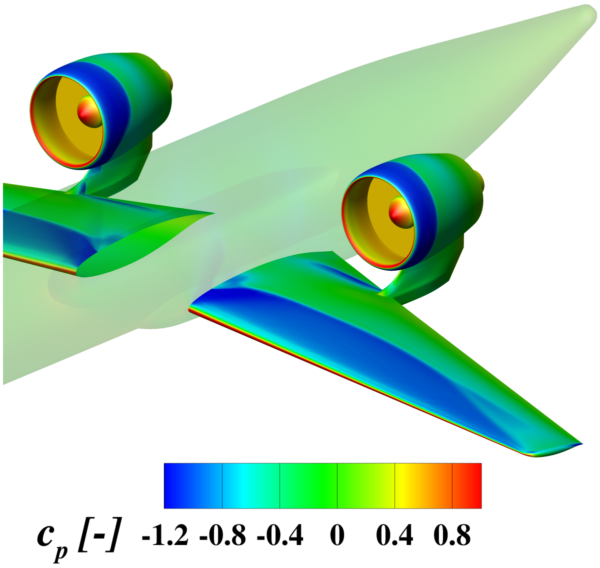

Fig. 5.31 *Visualization of c_p (x/c ≈-0.1) for the FSW*

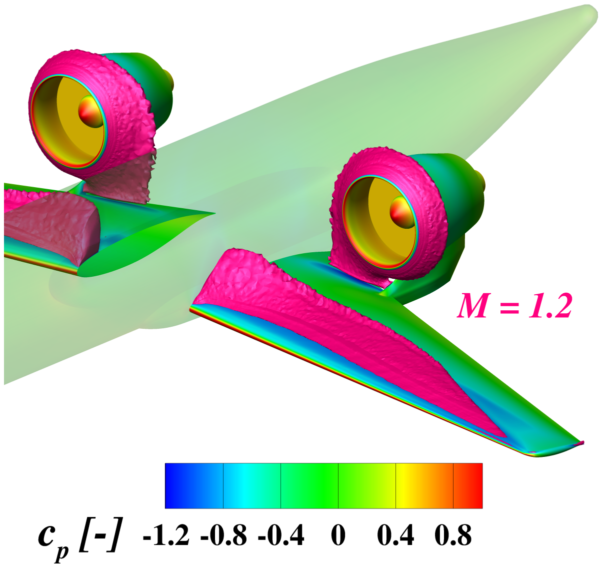

Fig. 5.32 *Visualization of iso-surfaces for M=1.2 (x/c ≈-0.1) for the FSW*

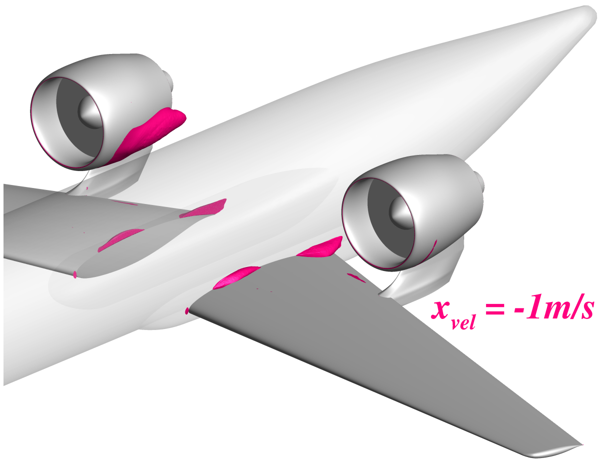

Fig. 5.33 *Visualization of iso-surfaces for x_{vel}=-1 m/s (x/c ≈-0.1) for the FSW*

Following, the aerodynamic features of all three configurations will be analyzed to identify the source of the most dominant drag variations. As starting point, the configuration with the largest overlap between nacelle and wing (x/c ≈-0.095) will be evaluated. Therefore, Fig. 5.31 to Fig. 5.33 visualizes different features from the same perspective. The figures present not only one half of the aircraft but the full aircraft by mirroring the flow solution. Thus, features outboard as well as inboard of the pylon could be detected through the transparent fuselage. The surface contour in Fig. 5.31 displays the pressure coefficient c_p. Based on the surface pressure distribution, the upstream shift of the iso-bar lines in the wing/fuselage junction is obvious. In addition blue areas, indicating low static pressure values, can be found on the outer nacelle front and in the channel between nacelle, fuselage and wing close to the trailing edge. This figure is enhanced by iso-Mach surface for $M = 1.2$ in Fig. 5.32. The iso-surfaces are colored magenta to stand out from the surface contour. Thus, a correlation between low pressure regions and iso-Mach surfaces are traceable. Because this configuration features the largest overlap of nacelle highlight and wing trailing edge, the resulting channel inboard of the engine is more distinct. Consequently, a large area of supersonic flow can be found with a peak Mach number of 1.6 in the narrow place between pylon, nacelle and wing, resulting in highest wave drag values within this comparison. The preceding analysis of the spanwise wave drag variation due to the OWN installation highlighted this flow channel as main source of wave drag. Thus, it can be stated that the wave drag correlates to the flow acceleration through the channel, which depends on the wing/nacelle overlap. However, the high Mach numbers are not only resulting in high wave drag values, but also imply high pressure gradients, which might cause shock induced flow separations. Since, the flow displacement by the geometry is almost identical, despite small variations of the pylon size, the cause for viscous pressure drag variations is probably the presence of flow separations. Therefore, areas of reversed flow ($x_{vel} = -1m/s$) are highlighted in Fig. 5.33. Three large areas of reversed flow can be identified. Two can be found at the wing/fuselage junction and another on the inboard facing nacelle. The first flow separation in the wing fuselage junction starts directly downstream of the shock position. This is a known weak spot of forward swept wings. The two remaining flow separations are correlating with the strong shock in the flow channel. Especially, the area of reversed flow on the nacelle expands significantly leading to a distinct flow displacement and pressure losses. Consequently, the sum of these three flow separation results in a significantly high viscous pressure drag.

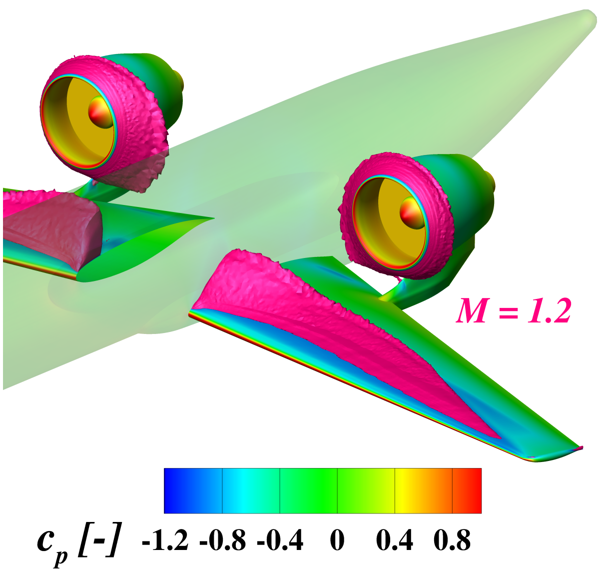

Fig. 5.34 *Visualization of iso-surfaces for M=1.2 (x/c ≈0.0) for the FSW*

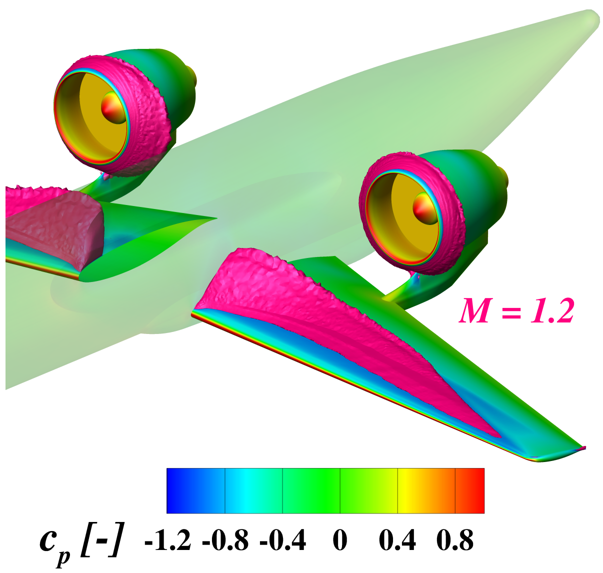

Fig. 5.35 *Visualization of iso-surfaces for M=1.2 (x/c ≈0.1) for the FSW*

Starting from the most upstream engine position, the impact of the horizontal engine position on the aerodynamic flow features is analyzed. For this purpose, the iso-Mach visualization, analogous to Fig. 5.32, for $x/c \approx 0$ and $x/c \approx 0.1$ is presented in Fig. 5.34 and

Fig. 5.35, respectively By comparison of all three configurations, a general contraction of the iso-surface for $M = 1.2$ around the nacelle is observable. The expansion of the iso-Mach surface in the channel between nacelle and fuselage is decreasing as well. For the mid engine position in Fig. 5.34, a small blue strip at the wing trailing edge is still present, indicating a c_p below -0.5 and thus still the presence of supersonic flow in this channel. The wave drag component totals still 35.8 dcts., which equals a decreases of about 10% in comparison with the most upstream engine position. However, the far-field drag evaluation revealed the largest wave drag decrease of 8.7 dcts. (25%) for the step between the mid and most downstream position. In case of the engine positioned at $x/c \approx 0.1$, the overlap between nacelle and forward swept trailing edge is minimal. Thus, the narrowing of the flow channel by the presence of the nacelle is formed behind the wing trailing edge. Consequently, the associated flow acceleration is reduced. As a result, the area of supersonic flow is not covering the entire channel between nacelle and fuselage. Instead, the flow exceeds $M = 1$ solely in a limited circle around the nacelle. This observation can be assumed as the main cause for the wave drag reduction in association with the horizontal engine position variation. Furthermore, it can be concluded that the horizontal distance between engine and wing has an impact on flow around the nacelle. By placing the engine above the wing, in the high velocity flow field, the engine experiences locally higher inflow velocities resulting in larger areas of supersonic flow. The downstream shift resulted in a shrinking of the iso-Mach surface. This interaction influences very likely the nacelle design and must be taken into account.

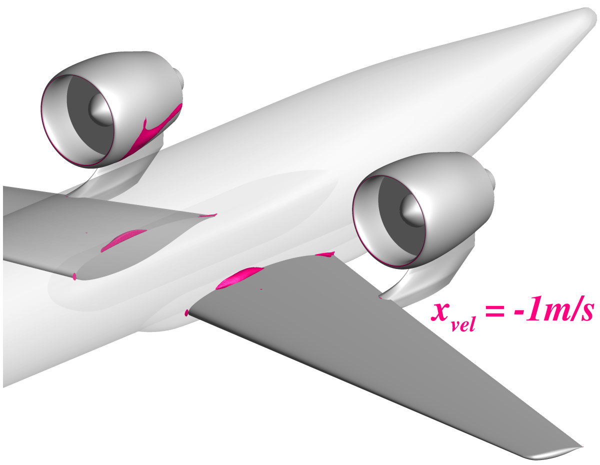

Fig. 5.36 *Visualization of iso-surfaces for M=1.2 (x/c ≈0.0) for the FSW*

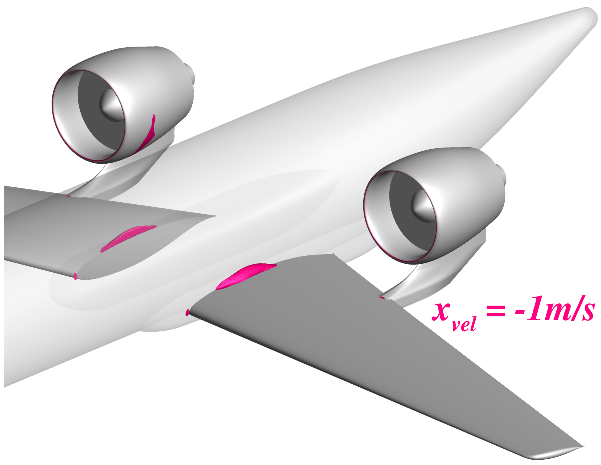

Fig. 5.37 *Visualization of iso-surfaces for M=1.2 (x/c ≈0.1) for the FSW*

Based on the declining flow accelerations and by implication declining shock strength, it can be assumed that the shock induced flow separations are affected as well. To confirm this assumption, the iso-surfaces for x_{vel}=-1 for the mid and most downstream engine position are shown in Fig. 5.36 and Fig. 5.37 analogous to Fig. 5.33. As mentioned, flow separations have a direct impact on the viscous pressure drag component. The far-field drag evaluation revealed a difference of 48 dcts. in viscous pressure drag between the most upstream and mid position. A comparison of the highlighted flow separations in Fig. 5.33 and Fig. 5.36 reveals flow separations at identical locations for both cases. Nevertheless, a significant contraction of the iso-surfaces for the engine at $x/c \approx 0.01$ can be recognized. Especially, the flow separation on the nacelle and at the wing trailing edge decreased significantly. This correlates with the decreasing shock strength in the flow channel between fuselage, wing and nacelle. In Fig. 5.37, representing the engine position at $x/c \approx 0.1$, the flow separation at the wing trailing edge is vanished and the area of reversed flow on the nacelle decreased to a minimum. Consequently, the further decrease in viscous pressure drag is reasonable. Nonetheless, a flow separation occurs at the wing/fuselage junction induced by the wing shock independent from the engine position.

Summarizing, the engine position has a significant impact on the overall drag coefficient. The total drag coefficient C_D varied by about 75 dcts. within the investigated parameter space. The evaluation revealed a dominant impact of the horizontal engine position. By analysis of three different engine positions, the formation of a flow channel between nacelle, wing and fuselage was identified as crucial. A large overlap of nacelle and wing results in a narrow channel leading to strong flow accelerations up to $M = 1.6$. These high pre-shock velocities are accompanied by strong pressure gradients. As a result, high wave drag components were identified on the one hand. On the other hand, shock induced flow separations occur on wing trailing edge and particular on the nacelle. These flow separations can be associated with viscous pressure drag, because of the resulting pressure losses and flow displacement. A downstream shift of the engine position enlarges the flow channel and by implication lowers the flow acceleration. Thus, the shock strength is reduced and by association the wave drag and flow separations. Finally, the biggest impact on the overall drag could be addressed to the flow separations which are directly linked to the viscous pressure drag component.

6 Conclusion

On the basis of two aircraft configurations, the impact of ultra-high bypass ratio (UHBR) over-wing-nacelle (OWN) installation on aerodynamic wing characteristics was investigated. The engine was placed above the wing trailing edge in cruise flight conditions. At a relevant Mach number of $M = 0.78$ different aspects were evaluated to build up a fundamental and generalized understanding of the associated installation effects.

The occurrence of aerodynamic features on the basis of a backward swept wing configuration and an arbitrary engine position was studied. A comparison between wing-body (WB) and wing-body-engine-pylon (WBEP) configuration at identical angle of attack revealed a crucial pressure increase on the inner upper wing segment accompanied by an upstream shift of the shock position. The outer wing experiences a reduction of the effective angle of attack as well as the formation of a double shock structure, caused by the overlap of nacelle and backward swept wing. These interferences result in a significant lift loss of about 40%. To reach the target lift of backward swept wing configuration, the incidence was increased by 1.42°. The aerodynamic installation effects on the outer wing were emphasized. As expected, the increasing incidence is associated with a decreasing local pressure coefficient c_p along the wing leading edge. The occurring flow phenomena are reflecting the observations by Hooker et al. [6] regarding the OWN TE 1 configuration at M=0.85.

Furthermore, the present work revealed, that the shock position on the inner wing segment remained almost unchanged as well as the surface pressure in the subsonic region of the wing for varying angle of attack. Thus, the rear wing pressure distribution is dominated by the presence of the OWN. This provides an explanation for the increasing drag divergence Mach number of the HondaJet due to the ONW installation [14], since the OWN engine has a dominant impact on the wing shock position. However, this observation raised the question, whether the pure presence of the OWN or the engine power setting affects the wing surface pressure. For this reason, the impact of flight idle power setting was examined. A comparison revealed a pressure increase due to the reduced engine mass-flow. The underlying effects due to the OWN installation in the wing pressure distributions are similar. An evaluation of the engine streamtubes yields to an additional observation. The variation of the engine inlet pressure is associated with the formation of a proboscis, creating a direct interaction between engine inlet and surface pressure distribution. By this, the sphere of influence by the OWN becomes apparent. However, this finding is based on a significant power setting variation between flight idle and cruise power. Consequently can be stated, that the presence of the OWN is the main cause for the installation effects and the power settings are of secondary importance.

The OWN installation on the forward swept wing configuration revealed similar interactions. The inner wing segment is characterized by a pressure increase on the upper surface and a crucial upstream shift of the shock position. In contrast, the outer wing pressure distribution is almost unaffected. This results from the nonexistent overlap between forward swept outer wing and nacelle. The flow channel between nacelle, wing and fuselage experiences a distinct flow acceleration including a pressure level comparable to the leading edge suction peak. A comparison of the forward swept wing configuration at target α_{WB} and target $C_{L,WB}$ verifies an area with unchanged pressure level in front of the nacelle, despite a different incidence angle, as found for the backward swept wing configuration.

The spatial expansion of this unaltered pressure region is comparable with the results observed for backward swept wing configuration. Furthermore can be stated on the basis of both OWN configurations, that an overlap of nacelle and swept wing trailing edge results in detrimental aerodynamic interference. The backward swept wing features a double shock structure along the outer wing, while the inner wing section of the forward swept configuration faces significant flow accelerations in the channel between fuselage, wing and nacelle.

Following, the impact of the OWN and accompanied installation effects on the aerodynamic performance was evaluated. Therefore, the physical drag breakdown into friction, wave, viscous pressure and lift-induced drag for WB and WBEP at identical C_L was considered. The friction drag rise corresponds to the increase in wetted area and thus meets the expectations. In addition, an increase of lift induced drag was expected due to the distinct disturbance of the spanwise lift distribution. However, a disproportional increase in wave drag was observed for both configurations. This drag rise could be ascribed partly to pronounced areas of supersonic flow on the nacelle, since the nacelle design is not suited for a mounting in the region of high flow velocities induced by the wing upper side. Thus, the pre-shock Mach number on the installed outer nacelle is increased in comparison with the isolated nacelle, followed by a distinct pressure gradient. The challenging flow along the nacelle can also be found in [6], where a high BPR engine with locally high Mach numbers along the outer nacelle in isolated flow conditions was not further investigated due to significant installation drag on both nacelle and wing. Instead, the slim Ultra Fan nacelle was chosen for most of the proceeding optimizations in the accelerated flow field above the wing trailing edge.

The increasing shock strength on wing and nacelle results partially in shock induced flow separations, leading to an increase of viscous pressure drag. In case of the backward swept wing configuration, these flow separations are minor, while large areas of reverse flow, originating from shock induced flow separations were observed for the forward swept wing configuration. Furthermore, the impact of the pylon fairing has to be addressed while comparing the viscous pressure drag of backward and forward swept wing configuration. The extended fairing of the backward swept wing configuration has a crucial impact on the viscous pressure drag, in the same order as the nacelle, while the pylon installation on the forward swept wing configuration causes a negligible drag rise for the overall configuration. Nevertheless, the most dominant drag rise due to the OWN installation on the forward swept wing configuration was observed in the flow channel between fuselage, wing and nacelle. There, a significant wave and viscous pressure drag rise is present, induced by two sequential low pressure regions associated by high pre-shock Mach numbers of about 1.4 and shock induced flow separations. This flow characteristic is aggravated by the forward swept trailing edge, resulting in an geometric overlap between nacelle and inboard wing. In contrast, the backward swept wing configuration features a geometric overlap between outer wing and nacelle, which causes a double shock structure accompanied by an increase in wave drag. In summary, both configurations experience a deteriorated aerodynamic performance due to a drag increase of more than 60 dcts. caused by the OWN installation.

Based on an arbitrary engine positions, a concluding assessment of the OWN installation would be incomplete. For that reason, an engine position variation was performed to evaluate its impact on the aerodynamic characteristic and performance of the wing. The vertical and horizontal engine position was varied with the aid of a surrogate-based optimization framework to gather areal information within the defined parameter space. To assess the impact by the OWN installation on the wing, the evaluation focused on the changes of aerodynamic coefficients C_l and C_d and characteristics related to the wing at constant overall lift coefficient C_L. The analysis revealed a correlation between vertical engine position and lift coefficient of the wing $C_{l,wing}$. With increasing distance, the pressure level along the upper rear wing decreases, while the lower wing is unaffected. Thus, more lift can be generated by the wing to achieve the overall target lift coefficient and concurrently, the aircraft is able to operate at a smaller angle of attack.

The area of supersonic flow on the wing is almost unaffected by the vertical engine position. This changes by an adaptation of the horizontal engine position. A detailed investigation of selected samples of the backward and forward swept wing configuration revealed a parallel shift between shock position and horizontal engine position. Furthermore, the necessary incidence for target C_L decreases while reducing the overlap between engine and wing trailing edge. This is caused by the accompanied increase of the area of supersonic flow respectively pressure decrease on the wing upper surface. At this point, the presence of the powered engine becomes again noticeable, because the shock position moves downstream despite a significant reduction of the aircraft incidence.

However, the most dominant effect of the horizontal engine position variation was observed with respect to the wing drag coefficient $C_{d,wing}$ for both backward and forward swept wing configuration. In case of backward swept wing configuration, a contrary behavior of viscous pressure and wave drag is present. On the one hand, a large overlap between engine and wing aggregates the detrimental supersonic characteristics on nacelle and wing. On the other hand, the junction between nacelle and inflexible pylon fairing results in large flow separations and consequently high viscous drag components with increasing downstream position. The dominant impact of the horizontal engine position meets the expectations by the wind tunnel experiments of Szodruch and Kotschote [18] and confirms the OWN position variation by Hooker et al. [6], where a distinct installation drag was found for overlapping engine positions.

The forward swept wing configuration enables a flexible pylon design. As a result, most physical drag components are decreasing with increasing distance between engine and wing. Solely, the friction drag increases slightly due to the expanding wetted area. The reason for a significant overall drag decrease is found in the flow channel between nacelle, wing and fuselage. The downstream movement of the engine widens this channel and prevents the formation of high supersonic flows and associated shock induced flow separations.

Concluding, the following statements can be formulated on the basis of the present study:

- Installation of an OWN-UHBR engine has a significant effect on the upper wing pressure distribution, while the lower wing is almost unaffected.
- The upper wing surface pressure is directly influenced and furthermore defined by the engine, whereby the sphere of influences in upstream and sideways direction is within the order of the engine diameter.
- This sphere of influence depends on the fan inlet pressure and thus on the engine power setting.
- Since the engine impact results in a local pressure increase, the wing shock position in front of the engine is shifted upstream.
- Originating from the OWN, flow disturbances are induced along the wing span, especially in the direction of the wing sweep. Consequently, the backward swept wing features a double shock structure on the outer wing, while the forward swept wing is characterized by an additional flow acceleration on the inner wing section amplified by the formed channel between nacelle and fuselage.
- The OWN installation leads to a reduction of the effective angle of attack along the entire wing span.
- Because the dominant disturbance propagation is following the wing sweep, only the inner 50% of the forward swept wing are affected by the OWN, while in contrast the aerodynamic characteristic of the entire backward swept wing changes.
- The vertical engine position affects mainly the subsonic rear wing pressure level and thus has solely an impact on the wing lift coefficient $C_{l,wing}$.
- A direct correlation between horizontal engine position and shock position was found, while despite a decreasing angle of attack a downstream shift of the shock location in relation to an aft moving engine position was observed, which underlines the dominating presence of the OWN.
- First, the flow on the upper wing side is decelerated in font of the engine inlet and then accelerated along the nacelle resulting in locally higher Mach numbers in comparison with the isolated engine
- The horizontal engine position was identified dominant with respect to the overall drag, because the geometric overlap between nacelle and wing results in additional flow accelerations and respectively higher pre-shock Mach numbers on both components. The increased pre-shock Mach numbers are partly accompanied by shock induced flow accelerations leading to additional wave and viscous pressure drag.

The present work describes the fundamental installation effects of OWN engines above the wing trailing edge of on transonic operating aircraft and provides a general insight regarding the origins and consequences of the aerodynamic phenomena. However, this thesis focuses on the aerodynamic characteristics and flow phenomena on the wing.

Further studies on the here investigated configurations have shown, that the wing shape can be adapted to take the impact of the OWN presence into account and achieve an reasonable aerodynamic performance [66]. However, the analysis of the wing engine interference revealed that a successful OWN installation also depends on the engine design. The engine position variation provides a first guidance for an appropriate engine placement. However, the impact of the nacelle shape in the challenging flow field above the wing trailing edge was neglected. But this is of great significance to enable an aerodynamic efficient OWN installation. Only by gaining further knowledge regarding the aerodynamic over wing nacelle design, a successful aircraft design is achievable and allows for the realization of an efficient and competitive transonic operating aircraft in combination with UHBR OWN engines.

A Appendix

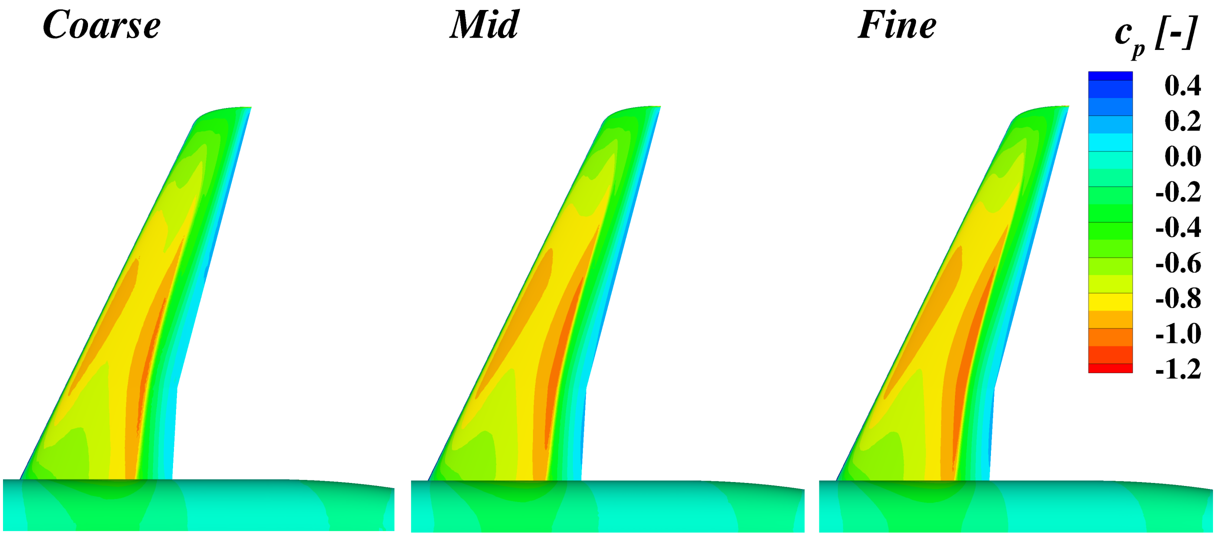

Fig. A.1 *Top view on pressure distribution of REF3-WB for coarse, mid and fine grid level with SA-neg turbulence model*

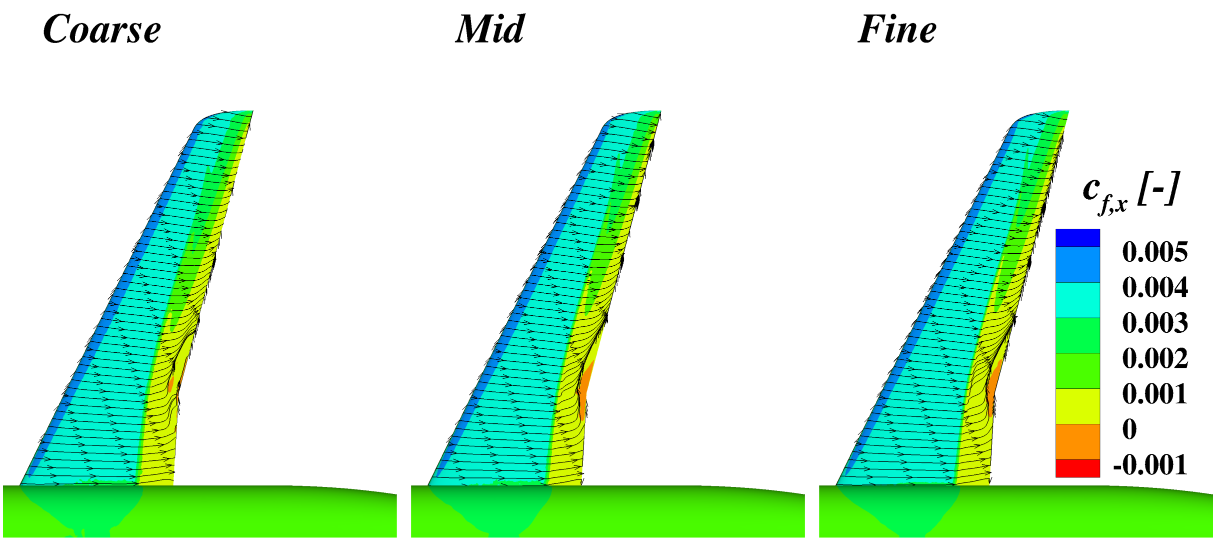

Fig. A.2 *Top view on skin friction of REF3-WB for coarse, mid and fine grid level with SA-neg turbulence model*

Bibliography

[1] DLR. ATTAS im Flug. URL https://www.dlr.de/content/de/bilder/luftfahrt/attas-im-flug.jpeg. CC-BY 3.0.

[2] W. Heinze. Main Data Sheet. A/C Type: REF3-2015 BASIS (with improvements in the second CRC 880 period 2015-2018). 2017.

[3] W. Heinze. Main Data Sheet. A/C Type: SFB880 Reference Aircraft REF4-2019 FSWref3-2015 basis. 2019.

[4] H. Kathen. *VFW 614, Quiet Short Haul Airliner*. 1974. doi: 10.2514/6.1974-937.

[5] M. Fujino. Design and Development of the HondaJet. *Journal of Aircraft*, 42(3): 755–764, 2005. doi: 10.2514/1.12268.

[6] J. R. Hooker, A. Wick, C. H. Zeune, and A. Agelastos. Over Wing Nacelle Installations for Improved Energy Efficiency. *31st AIAA Applied Aerodynamics Conference*, 2013. doi: 10.2514/6.2013-2920.

[7] J. R. Hooker, A. T. Wick, and C. J. Hardin. Commercial Cargo Derivative Study of the Advanced Hybrid Wing Body Configuration with Over-Wing Engine Nacelles. *NASA Report NASA/CR-2017-219653*, November 2017. NF1676L-26587.

[8] A. T. Wick, J. R. Hooker, J. Walker, D. T. Chan, R. Plumley, and C. Zeune. Hybrid Wing Body Performance Validation at the National Transonic Facility. *55th AIAA Aerospace Sciences Meeting*, 2017. doi: 10.2514/6.2017-0099.

[9] R. Rudnik, C.-C. Rossow, and H. Frhr. v. Geyr. Numerical simulation of engine/airframe integration for high-bypass engines. *Aerospace Science and Technology*, 6:31–42, 2002.

[10] LEAP-1A: chosen to power the Airbus A320neo. URL https://www.safran-aircraft-engines.com/commercial-engines/single-aisle-commercial-jets/leap/leap-1a. [Accessed: 13.11.2019].

[11] European Aviation Safety Agency. *TYPE-CERTIFICATE DATA SHEET No. E.110 for Engine LEAP-1A and LEAP-1C series engines*, 2017. URL https://www.easa.europa.eu/sites/default/files/dfu/TCDS%20E.003%20issue%2004_20170928.pdf. [Accessed: 13.11.2019].

[12] European Aviation Safety Agency. *TYPE-CERTIFICATE DATA SHEET No. E.003 for CFM56-5B and CFM56-5C series engines*, 2019. URL https://www.easa.europa.eu/sites/default/files/dfu/EASA%20E110%20TCDS%20Issue%208%20LEAP-1A-1C.pdf. [Accessed: 13.11.2019].

[13] W. J. G. Bräunling. *Flugzeugtriebwerke*. Springer, 4 edition, 2015. ISBN 978-3-642-34538-8.

[14] M. Fujino and Y. Kawamura. Wave-Drag Characteristics of an Over-the-Wing Nacelle Business-Jet Configuration. *Journal of Aircraft*, 40(6):1177–1184, 2003. doi: 10.2514/2.7207.

[15] J. Barche. Tragflügelentwurf am Beispiel des Verkehrsflugzeuges VFW 614. *Zeitschrift für Flugwissenschaften*, 22(4):101–115, 1974.

[16] G. Krenz and B. Ewald. Airframe - Engine interaction for engine configurations mounted above the wing; part i: Interference between wing and intake/jet; part ii: Engine jet simulation problems in wind tunnel tests. *AGARD Conference Proceedings*, (150), 1975. doi: 10.2514/6.1974-937. AIRFRAME/PROPULSION INTERFERENCE.

[17] D. E. Reubush. Effect of Over-the-Wing Nacelles on Wing-Body Aerodynamics. *Journal of Aircraft*, 16(6):359–365, 1979. doi: 10.2514/3.58532.

[18] J. Szodruch and J. Kotschote. Wind tunnel tests of over-the-wing nacelles. *Journal of Aircraft*, 20(7):606–611, 1983. doi: 10.2514/3.44918.

[19] M. Fujino. Aerodynamic and Aeroelastic Design of Experimental Aircraft MH02. *Proceedings of the 1994 AIAA/FAA Joint Symposium on General Aviation Systems*, pages 435–459, May 1994.

[20] D. Sasaki and K. Nakahashi. Aerodynamic Optimization of an Over-the-Wing-Nacelle-Mount Configuration. *Modelling and Simulation in Engineering*, 2011. doi: 10.1155/2011/293078.

[21] D. T. Chan, J. R. Hooker, A. T. Wick, R. W. Plumley, C. H. Zeune, M. V. Ol, and J. A. DeMoss. Transonic Semispan Aerodynmic Testing of the Hybrid Wing Body with Over Wing Nacelles in the National Transonic Facility. *55th AIAA Aerospace Sciences Meeting*, 2017. doi: 10.2514/6.2017-0098.

[22] W. Heinze. Ein Beitrag zur quantitativen Analyse der technischen und wirtschaftlichen Auslegungsgrenzen verschiedener Flugzeugkonzepte für den Transport grosser Nutzlasten. *ZLR-Forschungsbericht 94-01*, 1994.

[23] K. Horstmann, G. Redeker, A. Quast, U. Dreßler, and H. Bieler. Flight Tests with a Natural Laminar Flow Glove on a Transport Aircraft. *Flight Simulation Technologies Conference and Exhibit, Guidance, Navigation, and Control and Co-located Conferences*, pages 385–392, 1990. doi: 10.2514/6.1990-3044.

[24] M. Kruse, T. Wunderlich, and L. Heinrich. A Conceptual Study of a Transonic NLF Transport Aircraft with Forward Swept Wings. *30th AIAA Applied Aerodynamics Conference 2012*, 2012. doi: 10.2514/6.2012-3208.

[25] A. Seitz, M. Kruse, T. Wunderlich, J. Bold, and L. Heinrich. The DLR Project LamAiR: Design of a NLF Forward Swept Wing for Short and Medium Range Transport Application. *29th AIAA Applied Aerodynamics Conference 2011*, 2011. doi: 10.2514/6.2011-3526.

[26] T. McGeer. Wing Design for Minimum Drag with Practical Constraints. *Journal of Aircraft*, 21(11):879–886, 1984. doi: 10.2514/3.45058.

[27] T. Gerhold. Overview of the Hybrid RANS Code TAU. In N. Kroll and J. Fassbender, editors, *MEGAFLOW – Numerical Flow Simulation for Aircraft Design*, volume 89, pages 81–92. Springer, 2005. doi: 10.1007/978-3-030-52429-6_5.

[28] J. Wild. AeroForce - Thrust/Drag Bookkeeping and Aerodynamic Force Breakdown over Components update v 0.6.8, 2018. ISSN 1614-7790.

[29] D. Destarac and J. van der Vooren. Drag/thrust analysis of jet-propelled transonic transport aircraft; Definition of pyhsical drag components. *Aerospace Science and Technology*, 8:545–556, 2004.

[30] G. A. Wilke. Aerodynamic Optimization of Helicopter Rotor Blades using Variable Fidelity Methods, 2017.

[31] J. Blazek. *Computational Fluid Dynamics: Principles and Applications*. Elsevier, 2001. ISBN 0 08 043009 0.

[32] H. Schlichting and K. Gersten. *Grenzschicht-Theorie*. Springer, Berlin, Heidelberg, 1997. ISBN 978-3-662-07555-5. doi: 10.1007/978-3-662-07554-8_5.

[33] P.R. Spalart and S.R. Allmaras. A One-Equation Turbulence Model for Aerodynamic Flows. *AIAA paper*, (92-0439), 1992.

[34] S.R. Allmaras, F.T. Johnson, and P.R. Spalart. Modification and Clarification for the Implementation of the Spalart-Allmaras Turbulence Model. *7th International Conference on Computational Fluid Dynamics*, (ICCFD7-1902), 2012.

[35] P. R. Spalart. Strategies for turbulence modelling and simulations. *International Journal of Heat and Fluid Flow*, 21:252–263, 2000.

[36] Langley reseach center - turbulence modeling resource. URL `https://turbmodels.larc.nasa.gov/rsm-ssglrr.html`. [Accessed: 03.12.2021].

[37] Technical Documentation of the DLR TAU-Code Release 2019.1.0.

[38] R.C. Swanson, R. Radespiel, and E. Turkel. Comparison of several Dissipation Algorithms for Central Difference Schemes. *ICASE Report*, (97-40), 1997.

[39] A. Jameson, W. Schmidt, and E. Turkel. Numerical Solutions of the Euler Equations by Finite Volume Methods Using Runge-Kutta Time-Stepping Schemes. *AIAA paper*, (81-1259), 1981.

[40] R. Courant, K.O. Friedrichs, and H. Lewy. On the Partial Difference Equations of Mathematical Physics. *IBM Jounal*, (11):215–234, 1967.

[41] R. Dwight. Time-Accurate Navier-Stokes Calculations with Approximately Factored Implicit Schemes. *Computational Fluid Dynamics*, 2004.

[42] CentaurSoft: Centaur Hybrid Grid Generation System. URL `http://www.centaursoft.com`.

[43] D. Destarac. Three-Component Breakdown of Spurios Drag in Computational Fluid Dynamics. *Journal of Aircraft*, 52(4):1336–1344, 2015. doi: 10.2514/1.C032924.

[44] S. Crippa, S. Melber-Wilkending, and R. Rudnik. DLR Contribution to the First High Lift Prediction Workshop. *49th AIAA Aerospace Sciences Meeting including the New Horizons Forum and Aerospace Exposition*, 2011. doi: 10.2514/6.2011-938.

[45] L. F. Richardson. The Approximate Arithmetical Solution by Finite Differences of Physical Problems Involving Differential Equations, with an Application to the Stresses in a Masonry Dam. *Philosophical Transactions of the Royal Society of London. Series A, Containing Papers of a Mathematical or Physical Character*, 210:307–357, 1911. doi: 10.1098/rsta.1911.0009.

[46] P. J. Roache. Perspective: A Method for Uniform Reporting of Grid Refinement Studies. *Journal of Fluids Engineering*, 116(3):405–413, 09 1994. ISSN 0098-2202. doi: 10.1115/1.2910291. URL `https://doi.org/10.1115/1.2910291`.

[47] S. Keye, V. Togiti, B. Eisfeld, O. Brodersen, and M. B. Rivers. *Investigations of Fluid-Structure Coupling and Turbulence Model Effects on the DLR Results of the Fifth AIAA CFD Drag Prediction Workshop*. doi: 10.2514/6.2013-2509. URL `https://arc.aiaa.org/doi/abs/10.2514/6.2013-2509`.

[48] L. Ju, Q. Du, and M. D. Gunzburger. Probabilistic methods for centroidal Voronoi tessellations and their parallel implementations. *Parallel Computing*, 28:1477–1500, 2002.

[49] D. Krige. A statistical approach to some mine valuation and allied problems on the Witwatersrand, 1951.

[50] J. Blinstrub, L. Bertsch, and W. Heinze. CRC 880 Vehicle Concepts and Comparative Noise Assessment. In R. Radespiel and R. Semaan, editors, *Fundamentals of High Lift for Future Civil Aircraft*, volume 145, pages 405–426. Springer, 2020. ISBN 978-3-030-52428-9. doi: 10.1007/978-3-030-52429-6_25.

[51] C. Werner-Westphal, W. Heinze, and P. Horst. Multidisciplinary Integrated Preliminary Design Applied to Unconventional Aircraft Configurations. *Journal of Aircraft*, 45(2), 2008. doi: 10.2514/1.32138.

[52] L. Rossian, K. S. Rossignol, R. Ewert, M. Herr, and J. W. Delfs. Aeroacoustic Analysis of a Circulation Control Airfoil with Solid and Porous Trailing Edge. In R. Radespiel and R. Semaan, editors, *Fundamentals of High Lift for Future Civil Aircraft*, volume 145, pages 215–229. Springer, 2020. ISBN 978-3-030-52428-9. doi: 10.1007/978-3-030-52429-6_14.

[53] R. Semaan, Y. El Sayed, S. Loges, B. R. Noack, and R. Radespiel. Active Flow Control Experiments on a High-Lift Configuration. In R. Radespiel and R. Semaan, editors, *Fundamentals of High Lift for Future Civil Aircraft*, volume 145, pages 77–90. Springer, 2020. ISBN 978-3-030-52428-9. doi: 10.1007/978-3-030-52429-6_5.

[54] F. Runge, K. Sommerwerk, M. Rohdenburg, and M. C. Haupt. Design of Active High Lift Wing Configurations Via Fluid-Structure Interaction Simulation. In R. Radespiel and R. Semaan, editors, *Fundamentals of High Lift for Future Civil*

Aircraft, volume 145, pages 197–211. Springer, 2020. ISBN 978-3-030-52428-9. doi: 10.1007/978-3-030-52429-6_13.

[55] G. Dargel, H. Hansen, J. Wild, T. Streit, H. Rosemann, and K. Richter. Aerodynamische Fluegelauslegung mit Multifunktionalen Steuerflächen. *Deutsche Gesellschaft für Luft- und Raumfahrt - Lilienthal-Oberth e.V.*, art. DGLR-2012-096, 2002.

[56] R. Radespiel, M. Burnazzi, M. Casper, and P. Scholz. Active flow control for high lift with steady blowing. *Aeronautical Journal*, 120(1223):171–200, 2016. doi: 10.1017/aer.2015.7.

[57] J. Roskam. *Airplane Design*. Desing, Analysis and Research Corporation, 1985.

[58] C. D. Harris. NASA Supercritical Airfoils. *NASA Technical Paper*, (2969), 1990.

[59] J. Weber, G. G. Brebner, and D. Küchemann. Low-Speed Tests on 45 deg Swept back Wings. *Aeronautical Research Council Reports and Memoranda*, 2882, 1951.

[60] J. Wild. Mach and Reynolds Number Dependencies of the Stall Behavior of High-Lift Wing-Sections. *Journal of Aircraft*, 50(4):1202–1216, 2013. doi: 10.2514/1.C032138.

[61] M. Hepperle. MDO on Forward Swept Wings, 2009. URL `https://www.mh-aerotools.de/company/paper_12/KATnet%20-%20Forward%20Swept%20Wings%20-%20DLR-AS%20-%20Hepperle.pdf`. KATnet II Conference on Key Aerodynmic Technologies.

[62] GasTurb - Homepage. URL `https://www.gasturb.de/`. [Accessed: 2020-10-12].

[63] D. Giesecke, M. Lehmler, J. Friedrichs, J. Blinstrub, L. Bertsch, and W. Heinze. Evaluation of Ultra-High Bypass Ratio Engines for an Over-Wing Aircraft Configuration. 2:493–515, 2018. doi: 10.22261/JGPPS.8SHP7K.

[64] A. Renganathan, S. H. Berguin, M. Chen, J. Ahuja, J. C. Tai, D. N. Mavris, and D. Hills. Sensitivity Analysis of Aero-Propulsive Coupling for Over-Wing-Nacelle Concepts. *AIAA SciTech Forum*, 2018. doi: 10.2514/6.2018-1757. 2018 AIAA Aerospace Sciences Meeting.

[65] F. Lange and M. Kotzem. Aerodynamic Interference between Over-Wing-Nacelle and Wing. *Deutsche Gesellschaft für Luft- und Raumfahrt - Lilienthal-Oberth e.V.*, 2020. doi: 10.25967/530102.

[66] F. Lange and R. Rudnik. Aerodynamic Optimization of the OWN Configurations REF3 and REF4 in Cruise Flight. In R. Radespiel and R. Semaan, editors, *Fundamentals of High Lift for Future Civil Aircraft*, volume 145, pages 315–333. Springer, 2020. ISBN 978-3-030-52428-9. doi: 10.1007/978-3-030-52429-6_20.